PROCEEDINGS

MMM 2008

Fourth International Conference

MULTISCALE MATERIALS MODELING

OCTOBER 27-31, 2008 ▪ TALLAHASSEE, FLORIDA, USA

Tackling Materials Complexities via Computational Science

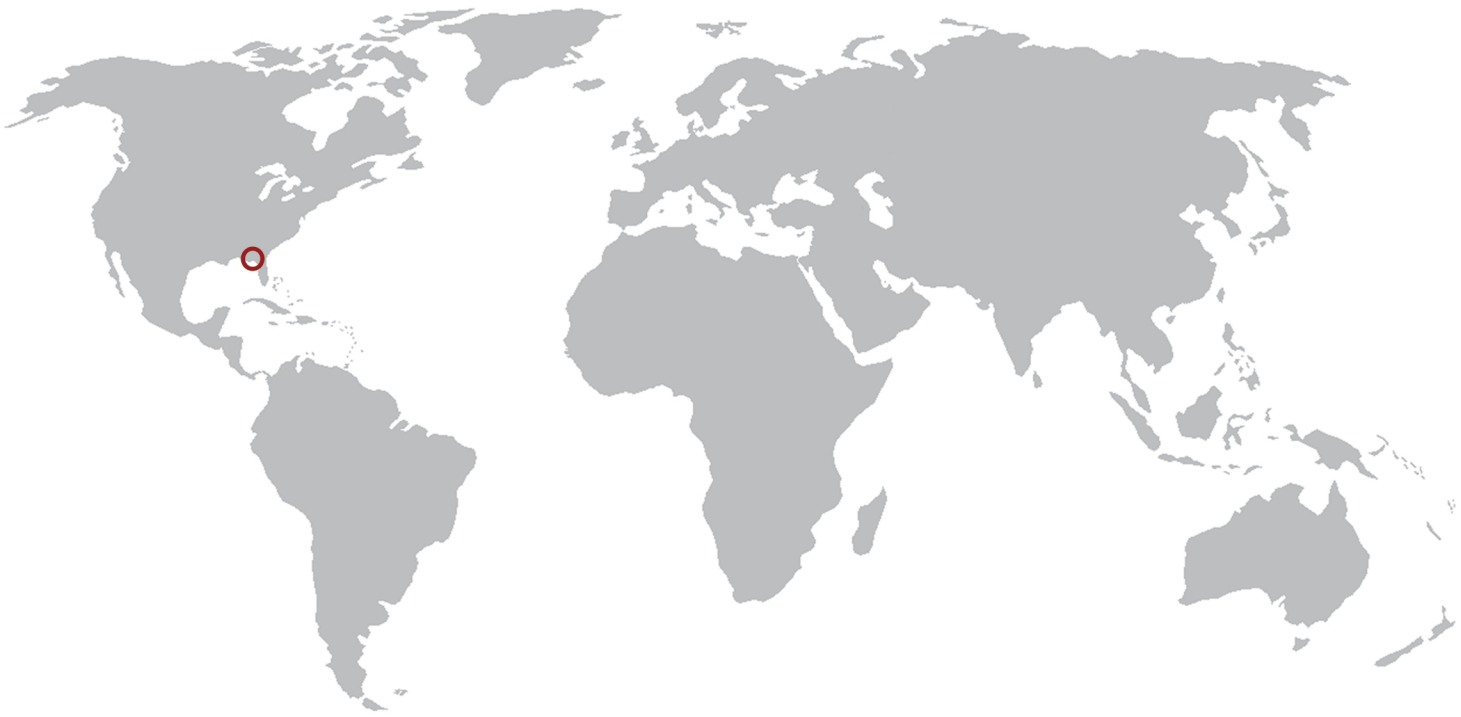

Hosted by the Department of Scientific Computing and Florida State University

DEPARTMENT OF Scientific COMPUTING

FLORIDA STATE UNIVERSITY 1851 VIRES ARTES MORES

Proceedings of

MMM 2008
Fourth International Conference
MULTISCALE MATERIALS MODELING
OCTOBER 27-31, 2008 ▪ TALLAHASSEE, FLORIDA, USA

Anter El-Azab
Editor

Organized and Hosted by
The Department of Scientific Computing and
Florida State University

DEPARTMENT OF Scientific COMPUTING

Papers published in this volume constitute the proceedings of the Fourth International Conference on Multiscale Materials Modeling (MMM-2008). Papers were selected by the program committee for oral or poster presentation. They are published as submitted, in the interest of timely dissemination.

ISBN 978-0-615-24781-6

Department of Scientific Computing
Florida State University
400 Dirac Science Library
P.O. Box 3064120
Tallahassee, FL 32306-4120

Printed in the United States of America

Forward

The field of multiscale modeling of materials promotes the development of predictive materials research tools that can be used to understand the structure and properties of materials at all scales and help us process materials with novel properties. By its very nature, this field transcends the boundaries between materials science, mechanics, and physics and chemistry of materials. The increasing interest in this field by mathematicians and computational scientists is creating opportunities for solving computational problems in the field with unprecedented levels of rigor and accuracy. Because it is a part of the wider field of materials science, multiscale materials research is intimately linked with experiments and, together, these methodologies serve the dual role of enhancing our fundamental understanding of materials and enabling materials design for improved performance.

The increasing role of multiscale modeling in materials research motivated the materials science community to start the Multiscale Materials Modeling (MMM) Conference series in 2002, with the goal of promoting new concepts in the field and fostering technical exchange within the community. Three successful conferences in this series have been already held:

- The First International Conference on Multiscale Materials Modeling (MMM-2002) at Queen Mary University of London, UK, June 17-20, 2002,
- Second International Conference on Multiscale Materials Modeling (MMM-2004) at the University of California in Los Angeles, USA, October 11-15, 2004, and
- Third International Conference on Multiscale Materials Modeling (MMM-2006) at the University of Freiburg, Germany, September 18-22, 2006.

The Fourth International Conference on Multiscale Materials Modeling (MMM-2008) held at Florida State University comes at a time when the wider computational science field is shaping up and the synergy between the materials modeling community and computational scientists and mathematicians is becoming significant. The overarching theme of the MMM-2008 conference is thus chosen to be "*Tackling Materials Complexities via Computational Science*," a theme that highlights the connection between multiscale materials modeling and the wider computational science field and also reflects the level of maturity that the field of multiscale materials research has come to. The conference covers topics ranging from basic multiscale modeling principles all the way to computational materials design. Nine symposia have been organized, which span the following topical areas:

- Mathematical basis for multiscale modeling of materials
- Statistical frameworks for multiscale materials modeling
- Mechanics of materials across time and length scales
- Multiscale modeling of microstructure evolution in materials
- Defects in materials
- Computational materials design based on multiscale and multi-level modeling principles

- Multiscale modeling of radiation effects in materials and materials response under extreme conditions
- Multiscale modeling of bio and soft matter systems

The first five topical areas are intended to cover the theoretical and computational basis for multiscale modeling of materials. The sixth topical area is intended to demonstrate the technological importance and industrial potential of multiscale materials modeling techniques, and to stimulate academia-laboratory-industrial interactions. The last two topical areas highly overlap with the earlier ones, yet they bring to the conference distinct materials phenomena and modeling problems and approaches with unique multiscale modeling aspects.

This conference would not have been possible without the help of many individuals both at Florida State University and around the world. Of those, I would like to thank the organizing team of MMM-2006, especially Professor Peter Gumbsch, for sharing their experience and much organizational material with us. I also thank all members of the International Advisory Board for their support and insight during the early organizational phase of the conference, and the members of the International Organizing Committee for the hard work in pulling the conference symposia together and for putting up with the many organization-related requests. Thanks are due to Professor Max Gunzburger, Chairman of the Department of Scientific Computing (formerly School of Computational Science) and to Florida State University for making available financial, logistical and administrative support without which the MMM-2008 would not have been possible. The following local organizing team members have devoted significant effort and time to MMM-2008 organization: Bill Burgess, Anne Johnson, Michele Locke, Jim Wilgenbusch, Christopher Cprek and Michael McDonald. Thanks are also due to my students Srujan Rokkam, Steve Henke, Jie Deng, Santosh Dubey, Mamdouh Mohamed and Jennifer Murray for helping with various organizational tasks. Special thanks are due to Bill Burgess and Srujan Rokkam for their hard work on the preparation of the proceedings volume and conference program.

I would like to thank the MMM-2008 sponsors: Lawrence Livermore National Laboratory (Dr. Tomas Diaz de la Rubia), Oak Ridge National Laboratory (Dr. Steve Zinkle) and Army Research Office (Drs. Bruce LaMattina and A.M. Rajendran) for the generous financial support, and thank TMS (Dr. Todd Osman) for the sponsorship of MMM-2008 and for advertising the conference through the TMS website and other TMS forums.

I would also like to thank all plenary speakers and panelists for accepting our invitation to give plenary lectures and/or serve on the conference panels. Lastly, I would like to thank the session chairs for managing the conference sessions.

Anter El-Azab
Conference Chair

International Advisory Board

Dr. Tomas Diaz de la Rubia	LLNL, USA
Prof. Peter Gumbsch	Fraunhofer Institute IWM, Freiburg, Germany
Dr. A.M. Rajendran	ARO, USA
Dr. Steve Zinkle	ORNL, USA
Prof. Anter El-Azab	FSU, USA
Prof. Michael Zaiser	Edinburgh, UK
Prof. Xiao Guo	Queens, London, UK
Prof. Shuichi Iwata	University of Tokyo, Japan
Prof. Jan Kratochvil	CTU, Prague, Czech Republic
Prof. Nasr Ghoniem (Chair)	UCLA, USA
Dr. Ladislas Kubin	ONERA-LEM, France
Prof. Shaker Meguid	Toronto, Canada
Prof. Alan Needleman	Brown, USA
Prof. Michael Ortiz	Caltech, USA
Prof. David Pettifor	Oxford, UK
Prof. Robert Phillips	Caltech, USA
Prof. Dierk Raabe	Max Planck Institute, Duesseldorf, Germany
Prof. Yoji Shibutani	Osaka University, Japan
Prof. Subra Suresh	MIT, Massachusetts USA
Prof. Yoshihiro Tomita	Kobe University, Japan
Prof. Erik Van der Giessen	University of Groningen, The Netherlands
Dr. Dieter Wolf	INL, USA
Prof. Sidney Yip	MIT, USA
Prof. David Bacon	Liverpool, UK
Dr. Michael Baskes	LANL, USA
Prof. Esteban Busso	Ecole des Mines, France
Prof. Timothy Cale	RPI, New York, USA
Dr. Moe Khaleel	PNNL, USA
Prof. David Srolovitz	Yeshiva, USA
Prof. Emily Carter	Priceton University, USA
Dr. Dennis Dimiduk	AFRL, USA
Prof. Rich Le Sar	Iowa State University, USA

International Organizing Committee

Weinan E	Princeton University, USA
Max Gunzburger	Florida State University, USA
Mitchell Luskin	University of Minnesota, USA
Rich Lehoucq	Sandia National Laboratories, USA
A.M. Rajendran	U.S. Army Research Office, USA
Stefano Zapperi	University of Rome, Italy
M.-Carmen Miguel	University of Barcelona, Spain
Mikko Alava	Helsinki University of Technology, Finland
Istevan Groma	Eötvös University, Hungary
Tom Arsenlis	Lawrence Livermore National Laboratory, USA
Peter Chung	Army Research Laboratory, USA

Marc Geers	Eindhoven University of Technology, The Netherlands
Yoji Shibutani	Osaka University, Japan
Dieter Wolf	Idaho National Laboratory, USA
Jeff Simmons	Air Force Research Laboratory, USA
Simon Phillpot	University of Florida, USA
Anter El-Azab (Chair)	Florida State University, USA
Daniel Weygand	University of Karlsruhe (TH), Germany
Zi-Kui Liu	Pennsylvania State University, USA
Hamid Garmestani	Georgia Institute of Technology, USA
Moe Khaleel	Pcific Northwest National Laboratory, USA
Mei Li	Ford Motor Company, USA
Fie Gao	Pacific Northwest National Laboratory, USA
Roger Stoller	Oak Ridge National Laboratory, USA
Pascal Bellon	University of Illinois, Urbana-Champaign, USA
Syo Matsumura	Kyushu University, Japan
Jeffery G. Saven	University of Pennsylvania, USA
Wei Yang	Florida State University, USA
T.P. Straatsma	Pacific Northwest National Laboratory, USA
L.P. Kubin	CNRS-ONERA, France
S.J. Zinkle	Oak Ridge National Laboratory, USA
Jaafar El-Awady	University of California, Los Angeles, USA
Shahram Sharafat	University of California, Los Angeles, USA
Hanchen Huang	Rensselaer Polytechnic Institute, USA
Yury N. Osetskiy	Oak Ridge National Laboratory, USA
Ron O. Scattergood	North Carolina State University, USA
Anna M. Serra	Universitat Politecnica de Catalunya, Spain

Local Organizing Committee (Florida State University, USA)

Prof. Anter El-Azab (Chair)
Prof. Max Gunzburger (Co-Chair)
Anne Johnson (Public relations and marketing)
Bill Burgers (Graphics and publications)
Srujan Rokkam (Proceedings and printing)
Michael McDonald (Webmaster)
Michele Locke (Finances)

Sponsors

Special thanks to the following sponsors:

- The Army Research Office
- Lawrence Livermore National Laboratory
- Oak Ridge National Laboratory

for their generous financial support, and to

- The Minerals, Metals & Materials Society (TMS)

for the sponsoring and advertising the conference through the TMS website.

Contents

Symposium 4

Symposium 4

Multiscale modeling of microstructure evolution in materials

Dislocation Mean Free Paths and Storage During Plastic Flow: A Study by Dislocation Dynamics Simulations

Benoit Devincre[1], Ladislas P. Kubin[1], Thierry Hoc[2],

[1]LEM, CNRS-ONERA, 29 Av. de la Division Leclerc, BP 72, 92322 Châtillon Cedex, France (E-mail: devincre@onera.fr)
[2]Laboratoire MSSMat., Ecole Centrale Paris, Grande Voie des Vignes, 92295 Châtenay-Malabry Cedex, France.

ABSTRACT

To predict in physical terms the strain hardening properties of crystals, one has to explicit two sets of master equations. The first one is the generalized Taylor relation determining the critical stress for activation of a slip system as a function of the microstructure [1]. The second one accounts for the evolution with strain of the dislocation density in the slip systems. Following the seminal work of Kocks, most existing models are describing this last evolution in terms of a dislocation mean free path (L), which is the statistic distance traveled by a dislocation segment of unit length before it is stored by its interactions with the microstructure. Dislocation dynamics (DD) simulations were performed in a representative volume element, using periodic boundary conditions, in order to identify the properties of dislocation mean free paths [2]. Copper was taken as model material. It will be shown that given the stress, L depends on the loading axis and is, in addition, a function of three simple material constants. These constants were measured by DD simulations with a good accuracy, thus allowing to predict rather precisely the values of L. Finally, evidence is made that this continuous mean free path can be statistically related to the discrete nature of plastic flow via the determination of the average amplitude of plastic strain bursts occurring in the simulated stress-strain curves.

[1] B. Devincre, L. Kubin, and T. Hoc. "Physical Analyses of Crystal Plasticity by DD Simulations". Scripta mater., **54**, 741 (2006).
[2] B. Devincre, T. Hoc, and L. Kubin. "Dislocation mean free paths and strain hardening of crystals". Science, **320**, 1745 (2008).

Stochastic Flow and Size Effects in Microcrystal Plasticity

Dennis M. Dimiduk[1], Chris Woodward[1], Satish I. Rao[2], Michael D. Uchic[1], Triplicane A. Parthasarathy[2], Richard LeSar[3] and Ed. Nadgorny[4]

[1]Air Force research Laboratory, Materials and Manufacturing Directorate, AFRL/RXLM, Bldg. 655, 2230 10th Street, Wright-Patterson AFB, OH 45433-7817 (E-mail: dennis.dimiduk@wpafb.af.mil)
[2]UES, Inc., 4401 Dayton-Xenia Road, Dayton, OH 45432-1894, (E-mail: satish.rao@wpafb.af.mil)
[3]Iowa State University, Department of Materials Science and Engineering, 2220 Hoover Hall, Ames, IA 50011-2300 (E-mail: lesar@iastate.edu)
[4]Michigan Technological University, Department of Physics, Houghton, MI 49931 (E-mail: nadgorny@mtu.edu)

ABSTRACT

A frontier topic in computational materials science and mechanics is the development of a plasticity-modeling framework that naturally and accurately represents evolving length-scale effects and the consequences of the dislocation structure. Current studies show that important intrinsic "size effects" exist separately from an evolving excess dislocation density at mesoscopic scales. Understanding those effects forms an essential foundation for representing microstructural effects within predictive computational frameworks. Our studies focused on simulation, analysis and measurements of the plastic phenomena occurring in microcrystals having dimensions at the lower end of the mesoscopic domain, wherein the discrete and stochastic nature of the dislocation ensemble is visible. In prior work, we reported on selected experimental results for Ni crystals. The present studies examined the athermal flow response of micron-scale single crystals using large-scale discrete dislocation simulations (DDS) in 3d, under conditions closely related to our experimental methods. Uniaxial compression tests were simulated for cells ranging from 0.5-20 micrometers in edge length. Simulations were carried out for a range of initial dislocation densities, close to experimentally observed values. While the simulations revealed a clear cell-size dependence of the flow response, they also showed intermittency in the flow response over a finite range of strain and a stochastic nature to the observed flow stress. Similar results are known from experiments and were recently described within other reports of simulation studies. This presentation provides further descriptions and analysis of the intermittency and stochastic variation of flow response for micron-scale crystals, from both simulation and experiment, within the context of the arguments suggested in previous work.

Introducing Dislocation Climb by Bulk Diffusion in Discrete Dislocation Dynamics Simulations

Dan Mordehai[1,2], Emmanuel Clouet[1,3], Marc Fivel[4] and Marc Verdier[4]

[1]SRMP, CEA-Saclay, 91191 Gif-sur-Yvette Cedex, France
(E-mail:danmord@tx.technion.ac.il)
[2]Department of Materials Engineering, Technion-Israel Institute of Technology, 32000 Haifa, Israel
[3]LMPGM, Universite Lille, 59655 Villeneuve d'Ascq Cedex, France
[4]SIMaP, Grenoble INP, CNRS/UJF, BP 75, 38402 St. Martin d'Heres, France

ABSTRACT

One of the powerful computational tools to study dislocation microstructure and plasticity at the mesoscopic scale is Dislocation Dynamics simulations, in which dislocations are treated as elastic entities. In this talk, we present a method to incorporate dislocation climb by bulk diffusion in Dislocation Dynamics simulations, by coupling this simulation technique with the diffusion theory of vacancies. We adapt the method to a 3-dimensional Discrete Dislocation Dynamics (DDD) simulation, in which each dislocation is represented by pure edge and screw dislocation segments. We firstly discuss the case in which the interaction between the flux fields of climbing segments is omitted. The calculation is demonstrated by simulating the activation of a Bardeen-Herring climb source upon the application of an external stress or under vacancy supersaturation, as well as isolated dislocation prismatic loops shrinkage and expansion. The model is then extended to allow climb in bulk materials, where dislocations are sources of vacancies, by considering simple interaction between the segments' flux fields. Subsequently, the model is shown to reproduce the coarsening of dislocation loops in annealed bulk. We observe in our simulations that large dislocation loops expand on the expense of smaller ones. Medium size loops are found to translate from expansion to shrinkage, as the vacancy supersaturation is relieved along the calculation. The processes observed in our simulations agree with experimental observations in fcc metals [1].

[1] D. Mordehai, E. Clouet, M. Fivel and M. Verdier, "Introducing Dislocation Climb by Bulk Diffusion in Discrete Dislocation Dynamics Simulations", Philosophical Magazine, **88**, 899 (2008).

Dislocations evolution in hetero-epitaxial multilayers

Siu Sin Quek[1], Yong-Wei Zhang[1,2], Yang Xiang[3] and David J. Srolovitz[4]

[1]Materials Theory and Simulation Laboratory, Institute of High Performance Computing, 1 Fusionopolis Way, #16-16, Connexis, Singapore 138632, Singapore (E-mail: quekss@ihpc.a-star.edu.sg)
[2] Department of Materials Science and Engineering, National University of Singapore, 10 Kent Ridge Crescent, Singapore 119260, Singapore (E-mail: msezyw@nus.edu.sg)
[3] Department of Mathematics, Hong Kong University of Science and Technology, Clear Water Bay, Kowloon, Hong Kong (E-mail: maxiang@ust.hk)
[4] Department of Physics, Yeshiva University, New York, NY 10033, USA (E-mail: srol@yu.edu)

ABSTRACT

We simulated dislocation dynamics during the growth of multilayer heteroepitaxial thin film like in the case of multilayer nanocomposites. We considered the case when threading dislocations emerging from the substrate replicate themselves into the thin film during the film growth process. In the regime where the thin film layer thickness is of tens of nanometers, the strain hardening mechanism is by the glide of single dislocation segments in the thin film instead of by dislocation pileups. We study the dislocations evolution behavior and their interactions since these now become significant to the strain hardening of the multilayer structure. We found that cross-slip of threading dislocation segments in multilayer structure is more prevalent compared to a single-layered thin film. This can result in a more complex array of interfacial dislocations and may have a siginificant contribution to the interactions between threading and interfacial dislocations. The simulation is carried out using the level set method incorporating thin film growth.

Plasticity Of Micro-samples: Discrete Dislocation Dynamics Study On The Size Effect Under Uniaxial Loading Conditions

Daniel Weygand[1], Jochen Senger[1], Peter Gumbsch[2], Oliver Kraft[3]

[1]University of Karlsruhe, izbs, Kaiserstr. 12, 76131 Karlsruhe, Germany,
(E-mail: Daniel.Weygand@izbs.uni-karlsruhe.de);
[2]Fraunhofer Institut für Werkstoffmechanik IWM, Wöhlerstr. 9-11,
79108 Freiburg, Germany
[3] Institut für Materialforschung IMF II, Forschungzentrum Karlsruhe, Germany.

ABSTRACT

The use of micromechanical devices in critical application such as sensors requires a characterization of the mechanical properties of metallic materials at the micro-meter scale. At this scale, the flow stress of single crystals is known to show a pronounced size effect even under nominally uniaxial loading, such as compression or tension. Before these findings, the size effect has mostly been related to the presence of strain gradients or interface constraints, leading to the classical Hall Petch scaling for the flow stress. At the micro-meter scale, the plasticity is no longer well described by a field theory, as the local variation of dislocation microstructure is essential for the understanding of the phenomenon at the origin of the size effect. Therefore a discrete dislocation dynamics tool is used to model the plastic flow of micro-specimens. Recent tensile experiment on wires under single slip orientation has shown that the aspect ratio is of importance for the size effect. In this presentation the results for single and multi-slip loading of wires with of different aspect ratios and diameters will be presented. The results suggest that the boundary constraints of wires with a low aspect ratio is more important for single slip than multislip, where dislocation-dislocation interaction are dominant. Furthermore, results on the bi-crystalline pillars will be presented in comparison to experiments and the role of grain boundaries as possible obstacle or source of dislocations will be discussed.

Financial support of the EC for the project NANOMESO (project no 16710) is gratefully acknowledged.

Modeling the Evolution of Intragrain Lattice Orientation Gradients and Yield Asymmetries in Polycrystalline Solids

Paul Dawson

196 Rhodes Hall, Sibley School of Mechanical and Aerospace Engineering
Cornell University, Ithaca, New York, 14853
(E-mail: prd5@cornell.edu)

ABSTRACT

Polycrystalline solids exhibit microstructural features at several length scales that are important to their macroscopic mechanical behavior. These range from packing arrangements and faults at atomistic scales to the contiguity of polycrystalline phases. The inhomogeneous material structure leads to heterogeneous deformations at virtually all of the scales even under nominally uniform loading conditions at the macroscopic scale. In this presentation we examine the coupling of effects from two scales: intragranular and intergranular. For polycrystals, the partitioning of deformation and the sharing of load among grains depends on the crystal anisotropy inherited from its lattice structure and orientation. The deformation within grains is heterogeneous owing to the varying constraints imposed by neighboring grains. The consequence is that plastic straining is not at all uniform over individual grains, which manifests itself as gradients in slip. In this presentation we will discuss two aspects of slip gradients in crystals within a polycrystalline body. The first is the development of gradients of the lattice orientation, which can display features such as cell-like spatial arrangement and twist-like correlations between misorientations and position. The second is the development of yield stress asymmetry, arising from the development of internal elastic strain distribution. This strain can bias the applied stress and cause a decrease in the apparent yield stress upon load reversal. Examples of each effect will be given for materials with cubic crystal structures.

Crystal Plasticity Models with Multi-Time Scaling for Cyclic Deformation of Polycrystalline Metals

Somnath Ghosh, Deepu S. Joseph, Pritam Chakraborty

Department of Mechanical Engineering, Ohio State University, 201 W. 19. Ave. Columbus, OH 43210 (E-mail: ghosh.5@osu.edu)

ABSTRACT

A dual time scale finite element model is developed in this paper for simulating the cyclic deformation of polycrystalline alloys characterized by crystal plasticity constitutive relationships. A wavelet-based scheme is used to decouple the governing equations into two time scales. Each time dependent variable is decomposed into its wavelet components. The wavelet coefficients exhibit long time scale (coarse) behavior and the wavelet basis captures the fine time scale behavior of the variable. A finite element framework and an equivalent coarse time scale evolution equation at the constitutive level is developed using this decomposition and is used to study the cyclic deformation of polycrystalline materials. The newly developed model enables time stepping over a large number of cycles resulting in greatly reduced computational time and therefore facilitates the study of the fatigue response of the material by simulating a large number of cycles to crack initiation.

1. Introduction

Advanced polycrystalline alloys with improved properties and reliability find widespread use in aerospace and automotive industries. These components are exposed to cyclic loading conditions during operation which results in fatigue or time delayed fracture [1]. Fatigue failure in the microstructure evolves in three stages. First there is crack nucleation due to inhomogeneous plastic flow or grain boundary failure followed by crack growth due to cyclic stresses and finally coalescence of cracks to cause fast crack propagation.

Crystal Plasticity based models are well suited to simulate the behavior of polycrystalline materials and study their cyclic behavior. Unlike other approaches such as Stress Life (S-N curve) or strain life (Coffin-Mason Rule), which are empirical or statistical in nature, crystal plasticity based models include the morphological and crystallographic features of the material in the constitutive response. The details of the crystal plasticity model are given in Section 2.Crystal Plasticity Models, though accurate becomes computationally expensive when used to study the fatigue response of real microstructures. Hence a faster methodology is required to solve the crystal plasticity model.

The typical response of a material point undergoing cyclic deformation based on crystal plasticity is shown in Fig. 1. As it can be seen from this figure, there exist two time scales in the material response: A fast varying fine time scale (τ) and a slow varying coarse time response (t) which varies very slowly within a cycle and therefore can be identified with a given cycle number. The net response is the fine time scale variation modulated by the coarse time behavior.

Since the coarse time scale variation is much smoother than the fine scale response, it can be solved using much larger time steps, if it can be decoupled from the fine scale response. Therefore a procedure to decouple the different scales with the ability to zoom in and obtain the fine scale response when required need to be developed in order to make the crystal plasticity models for fatigue behavior feasible.

Asymptotic based methods have been used [1, 2] to decouple the various scales while studying multiscale problems. However when applied to fatigue response, the asymptotic assumption is violated as the stress ratio approaches -1 (R->-1). A wavelet-based algorithm is therefore developed for the separation of scales, which works for all stress ratios. Each time dependent variable (displacement, plastic strain, stress etc) is decomposed into its wavelet components. The wavelet basis is assumed to be a function of fast (fine) time scale only, while the wavelet coefficients vary much slower when compared to the fine scale i.e. is a function of the coarse time scale. As a result much larger time steps could be used for tracking the evolution of these coefficients. A methodology based on this is presented in Section 3 and few results that show significant time advantage based on this framework is presented in Section 4.

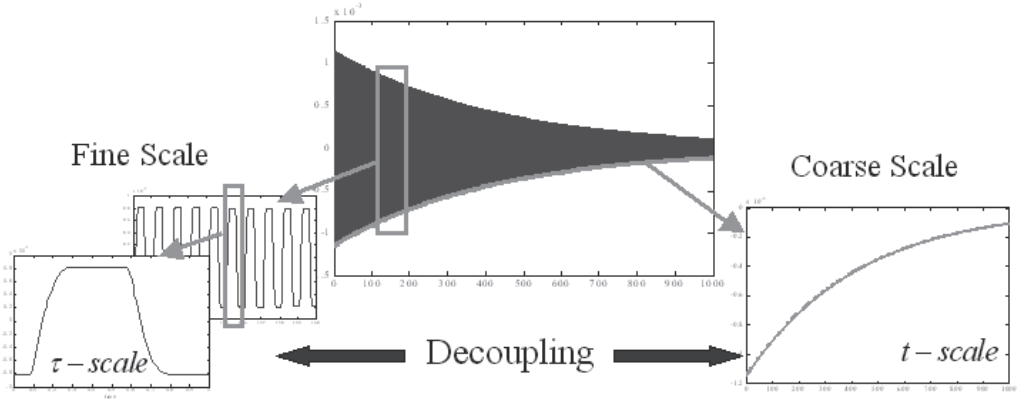

Figure 1. Evolution of plastic strain at a material point under cyclic loading

2. Crystal Plasticity Based Constitutive Model

In crystal plasticity, slip happening on different slip systems is the governing mechanism for the plastic behavior of a material [3]. A multiplicative decomposition of deformation gradient into an elastic and plastic deformation gradient (Eqn (1)) is performed. The evolution of plastic deformation gradient is related to the slip rate $\dot{\gamma}^{\alpha}$ on different slip systems as shown in Eqn (2).

$$F_{ij} = F^{e}_{ik} F^{p}_{kj} \tag{1}$$

$$\dot{F}^{p}_{ij} = \sum_{\alpha} \dot{\gamma}^{\alpha} S^{\alpha}_{o,ik} F^{p}_{kj} \tag{2}$$

The slip rate on each slip system is related to the resolved shear stress (τ^{α}) and slip system resistance (g^{α}) by a power law (Eqn (3)). The evolution of slip system resistance is related to the slip rate as shown in Eqn (4).

$$\dot{\gamma}^{\alpha} = \dot{\gamma}_0 \left(\frac{\tau^{\alpha}}{g^{\alpha}} \right)^{\frac{1}{m}} \operatorname{sgn}(\tau^{\alpha}) \tag{3}$$

$$\dot{g}^{\alpha} = \sum q^{\alpha\beta} h^{\beta} \mid \dot{\gamma}^{\beta} \mid \tag{4}$$

Finally the stress is related to the elastic part of deformation gradient as shown in Eqn (5).

$$\sigma_{ij} = \frac{1}{J} F^{e}_{ki} S_{kl} F^{e}_{lj} \quad \text{where} \quad S_{ij} = C_{ijkl} E_{kl} \quad \text{and} \quad E_{ij} = \frac{1}{2} (F^{e}{}_{ki} F^{e}{}_{kj} - \delta_{ij}) \tag{5}$$

3. Wavelet Based Multitime scale method

3.1 Wavelets

A wavelet basis spans the space of square integrable function through translation and dilation Eqn. (6). The wavelet transform of a given function splits the function into components of different resolutions [4].

$$f(\tau) = \sum_{m} \sum_{n} C^{m,n} \psi_{m,n}(\tau) \qquad and \qquad \psi_{m,n} = 2^{\frac{m}{2}} \psi(2^{m} \tau - n) \tag{6}$$

Wavelets form a good basis for representing the fine scale behavior because of the following properties:

(a) Orthogonal Support-Easy to evaluate the wavelet coefficients
(b) Compact Support-No Gibbs Phenomena unlike other bases (Fourier Series)
(c) For a given resolution of the fine scale behavior, the space of basis functions is finite.

In addition, as compared to asymptotic methods, the wavelet decomposition does not make assumptions on the order of contribution from different scales and therefore does not fail for cases where R->-1.

3.2 Coarse Scale Constitutive Equations

In this section, the coarse scale evolution equations corresponding to Eqn (2) and Eqn (4) are developed. Both these equations can be represented in the form:

$$\dot{y} = f(y, F_{ij}) = f(y_k, F^{k}_{ij}, \tau) \tag{7}$$

where $y(t,\tau)$ is the material response and F^{k}_{ij} are the known wavelet coefficients of deformation gradient for the cycle corresponding to coarse time t at a given gauss point . This can be decoupled into coarse and fine scale using the wavelet decomposition:

$$y(t, \tau) = \sum_{k} y^{k}(t) \psi_{k}(\tau) \tag{8}$$

Over a given cycle corresponding to coarse time t_{n+1}:

$$y(t_{n+1},\tau) = y(t_{n+1},0) + \int_0^\tau f(y^k, F_{ij}^k, \tau')d\tau' = y_0(t_{n+1}) + \int_0^\tau f(y^k, F_{ij}^k, \tau')d\tau' \tag{9}$$

Therefore given the initial value y_o of the variable for the cycle (Fig. 2), the wavelet coefficients of y corresponding to the cycle can be obtained as:

$$y^k(t_{n+1}) = y_0\delta_{0k} + \int_0^T y(t_{n+1},\tau)\psi_k(\tau)d\tau = y_0\delta_{0k} + \int_0^T \psi_k(\tau)\int_0^\tau f(y^k, F_{ij}^k, \tau')d\tau' d\tau \tag{10}$$

Therefore the coarse time evolution equation for y_0 can be shown to be:

$$\frac{dy_0}{dt} = Y_0(y_0, F_{ij}^k) = \frac{\sum_k y^k(y_0^{n+1}, F_{ij}^k)\psi_k(T) - y_0^{n+1}}{T} \tag{11}$$

Applying the above methodology, the coarse time equations for Eqn (2) and Eqn (4) are:

$$\frac{dF_{ij,0}^p}{dt} = Y_{ij}^p(F_{ij,0}^p, F_{ij}^k, g_0^\alpha) \qquad \text{and} \qquad \frac{dg_0^\alpha}{dt} = G^\alpha(F_{ij,0}^p, F_{ij}^k, g_0^\beta) \tag{12}$$

where $F_{ij,0}^p$ and g_0^α are the initial values of the plastic deformation gradient and slip system hardness for the cycle and are coarse time variables. Y_{ij}^p and G^α are evaluated based on Eqn (11).

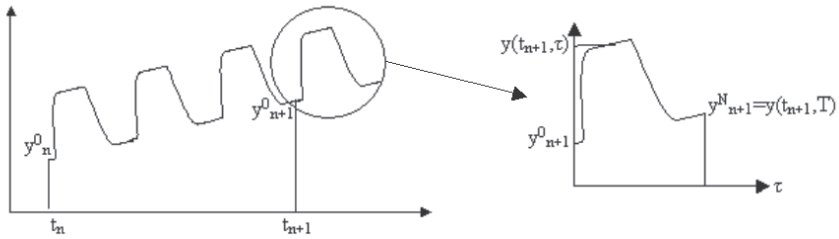

Figure 2: Evolution of state variable y at a material point

3.3 FEM framework

The nodal displacements are decomposed in terms of wavelet basis functions:

$$q_{i,\alpha}(t,\tau) = \sum_k q_{i,\alpha}^k(t)\psi_k(\tau) \tag{13}$$

The components of the deformation gradient at every gauss point can be obtained as:

$$F_{ij}^{k}(X,t) = \delta_{ij}\delta_{0k} + \sum_{\alpha} \frac{\partial N_{\alpha}}{\partial X_{j}} q_{i,\alpha}^{k} \tag{14}$$

Eqn. (14) is an input to the evolution equations in (12) and along with Eqns. (10) and (5) can be used to obtain the wavelet components of the stress corresponding to the coarse time (cycle) t_{n+1}. The residual corresponding to the weak form of the equilibrium equation is represented as:

$$\{R(t,\tau)\} = \int_{\Omega} [B]^{T} \{\sigma(t,\tau)\} d\Omega - \int_{\Gamma} [N]^{T} p(t,\tau) d\Gamma = 0 \tag{15}$$

Similar to other variables the residual can also be decomposed in terms of the wavelet basis function as follows.

$$\{R_{k}(t)\} = \frac{1}{T} \int_{0}^{T} \left(\int_{\Omega} [B]^{T} \{\sigma(t,\tau)\} d\Omega - \int_{\Gamma} [N]^{T} p(t,\tau) d\Gamma \right) \psi_{k}(\tau) d\tau = 0 \tag{16}$$

Eqn (16) is solved for the unknown wavelet coefficients of the displacement $q_{i,\alpha}^{k}(t)$.

4. Results and Discussion

The methodology is verified using 2 problems. One with $R = -1$ loading for an 8 element polycrystalline case and the other with $R \neq -1$ loading for a 343 element polycrystalline case with no latent hardening and fcc slip systems. In both the simulations Haar wavelet was used, along with second order backward difference scheme to integrate the coarse scale constitutive equations Eqn (12). Only the displacement coefficients which evolve during the coarse of the problem is considered for solution.

4.1 Loading $R \neq -1$

A triangular pressure load of average 500 MPa and amplitude of 125 MPa is applied. The comparison of displacement for a node and the slip system hardness evolution for a gauss point is shown in Fig. 3.

As can be observed from Fig. 3., the methodology gives good match with fine scale. Time advantage of 15 times is obtained.

4.2 Loading $R = -1$

A triangular load with maximum pressure of 700 MPa is applied. The comparison of displacement for a node and slip system hardness evolution for a gauss point is shown in Fig. 4.

As can be observed from Fig. 4, the methodology gives good match with fine scale. However significant time advantage was not obtained in this case due to the large number of coefficients, which evolve (hence larger number of degrees of freedom). Work is in progress to optimize this particular aspect of the model.

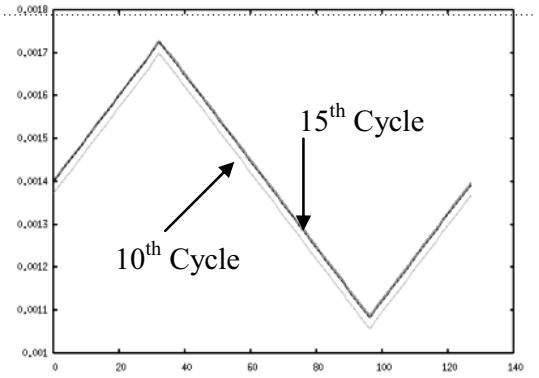

(a) Displacement for 15th cycle

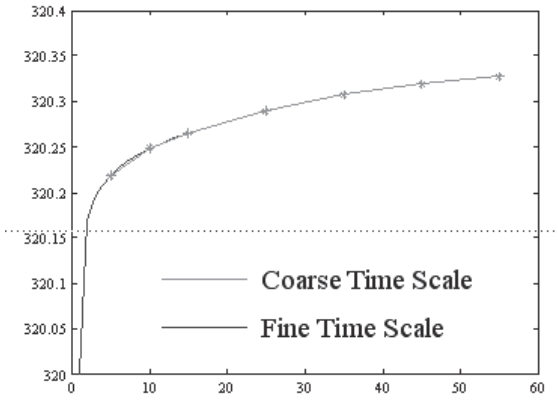

(b) Slip system resistance evolution

Figure 3: Comparison of displacements for a cycle and coarse time scale hardness evolution

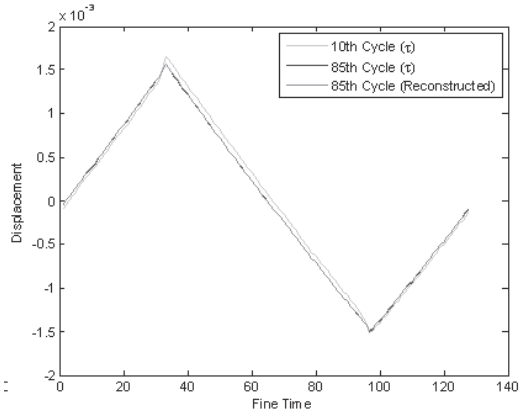

(a) Displacement for 100th cycle

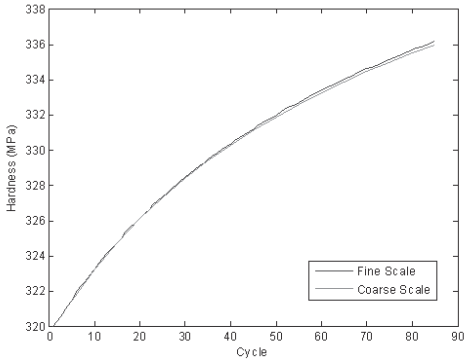

(b) Slip system resistance evoltuion

Figure 4: Comparison of displacements for a cycle and coarse time scale hardness evolution

References

[1] S. Manchiraju, M. Asai and S.Ghosh, "A dual-time-scale finite element model for simulating cyclic deformation of polycrystalline alloys," J. Strain Anal. Eng. Des. **42**, 183-200 (2007).
[2] Q.Yu and J.Fish," Temporal homogenization of viscoelastic and viscoplastic solids subjected to locally periodic loading", Computational Mechanics **29**, 199-211 (2002).
[3] C.A. Bronkhorst , S.R. Kalidindi and L. Anand, "Polycrystalline plasticity and the evolution of crystallographic texture in FCC metals", Philosophical transactions of the Royal Society of London A, **341**, 443-447 (1992).
[4] E. Hernandez, G. Weiss, "A First Course on Wavelets", CRC Press (1996).

Through-Process Texture and Microstructure Modeling of AA3103 from Hot Rolling to Final Annealing

C. Schäfer, V. Mohles, G. Gottstein

Institute of Physical Metallurgy and Metal Physics, Kopernikusstr.14, 52074 RWTH Aachen (E-mail: cschaefer@imm.rwth-aachen.de)

ABSTRACT

In the present work a through-process modeling scheme has been proposed for the prediction of recrystallization textures and microstructures starting from hot-rolling over cold rolling to final annealing. The deformation behavior is hereby modeled by means of the advanced deformation texture model GIA-3IVM+, which is based on a multi-grain approach and incorporates the work hardening behavior in terms of the evolution of dislocation densities. The recrystallization model is a spatially resolved model based on the cellular automaton method. This model allows the orientation dependent consideration of recovery on grain level. Hereby, the consideration of recovery is consistent with the formulation in GIA-3VM+. This allows the consequent tracking of changes in dislocation densities throughout the whole process. Since the used recrystallization model is a pure growth model, the nucleation is described by separate nucleation models to account for different nucleation mechanisms. The importance of those models becomes evident when considering the final microstructure after recrystallization, which is strongly dependent on the nucleus frequencies and on the amount of recovery before the initiation of nucleation. The presented modeling setup allows the prediction of final recrystallization textures with good agreement to experimental texture and reasonable predictions of grain sizes.

1. Introduction

For optimizing materials properties and processing the aluminum industry is interested in through-process modeling, e.g. during sheet metal fabrication. The key for reliable predictions in this case is the precise control of microstructure and texture. The main issue in this context is the modeling of recrystallization, which can strongly influence the material properties by severe changes in texture and microstructure. The evolution of recrystallization is strongly influenced by the prior deformation, especially by the deformation inhomogeneities, and by the precipitation state in case of particle-containing alloys. Against this background only a spatially resolved recrystallization model is capable of describing interaction of the involved processes. Softening processes, such as recrystallization occur during interpass time if hot-rolling is considered or during heat treatment after cold rolling. The scope of the present work was to model the texture and microstructure evolution during sheet metal fabrication of AA3103 subsequent to break down rolling.

2. Models

The modeling of hot-rolling and subsequent cold rolling with a final annealing treatment requires various submodels. The strain path information is obtained from FEM simulations.

For deformation texture prediction the advanced GIA model was used. It is based on a multi-grain approach, which considers the deformation of an eight-grain aggregate embedded in a homogeneous surrounding [1]. The deformation of the grains is described in terms of plastic deformation according to Taylor theory and by the introduction of geometrically necessary dislocations owing to grain interactions. The work-hardening behaviour required as input for GIA is calculated based on the dislocation density evolution by the model 3IVM+ [2]. Both models are incrementally coupled on grain scale, which makes GIA-3IVM+ a material-dependent model.

The modeling of recrystallization was accomplished with the CORe model, an adaptive cellular automaton, discrete in space and time [3, 4]. It allows the consideration of spatially resolved data, such as grain orientations, stored dislocation densities, inhomogeneities and second-phase particles. However, CORe is a pure growth model, which describes grain boundary motion by $v = m^* p$, whereas m is the boundary mobility, v the velocity and p the local driving force. Since the driving force for primary static recrystallization in aluminum alloys is the stored dislocation energy which is reduced by recovery, such effects were taken into account as well. The consistency with GIA-3IVM+ was ascertained by using the same model for recovery in CORe. Due to the spatial resolution in CORe, orientation-dependent recovery can be incorporated. The nucleation of recrystallization, however, needs to be described by separate nucleation models [5, 6].

Effects such as Zener drag and solute drag, which influence boundary mobility and local driving force of recrystallization, were accounted for by calculations with the precipitation model ClaNG, which is based on classical nucleation and growth theory of precipitation [7]. This allows tracking of potential changes in the precipitation behavior for the designed processing route prior to the actual texture simulation and delivers the required precipitation state at request.

3. Results

3.1 Hot Rolling of AA3103

Hot rolling was carried out in three passes from a slab thickness of 28mm to 4.2mm with a reduction of 50% in each pass. The initial material prior to hot rolling was fully recrystallized with a grain size of 50µm. The main texture component was the Cube orientation.

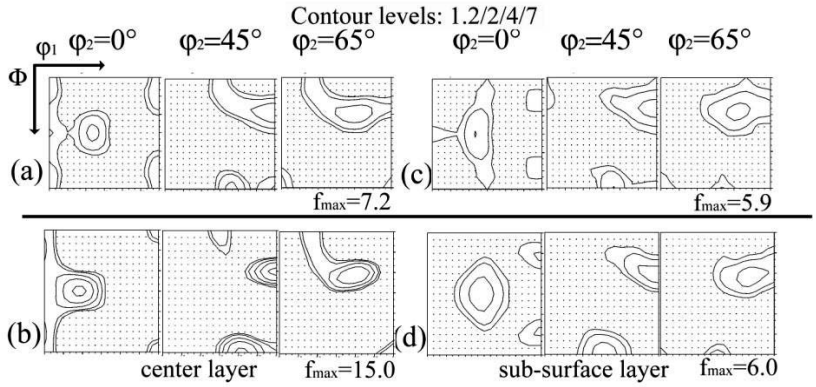

Fig.1 Macrotexture of hot rolled slab (a,b) experimental, (c,d) simulated.

During interpass time a recrystallized volume fraction of maximum 20% was assumed for the center-layer, respectively 100% recrystallized volume fraction for the sub-surface. Furthermore, recovery and drag effects by particles and solute atoms were considered. For the latter, the solid-solution content of manganese was calculated by a prior ClaNG simulation to be $c_{ss,Mn}$=0.6at%, the dispersoid particle radius r_P= 23.1nm, and the corresponding volume fraction f_P= 0.24Vol%. The temperature during hot rolling was T=330°C. For modeling the work hardening behavior, flow curves were fitted in the range T=250°-400°C and for strain rates ranging from 1 s^{-1} to 100 s^{-1}, were fitted. The textures after hot rolling are shown in Fig.1. The quality of texture prediction is quite good for center layer and sub-surface layer besides small deviations in the prediction of the rotated Cube orientations. The predicted grain size in the center layer after hot rolling was 258µm in RD, 50µm in TD and 9µm in ND direction compared to experiment with a grain size of 200µm in RD, 40µm in TD and 10µm in ND.

3.2 Cold Rolling

The simulated macrotexture obtained after hot rolling (Fig.1b) was used as input for a cold rolling simulation with the GIA-3IVM+ model for cold rolling reductions of 50% and 70%, respectively. The work hardening behavior was fitted with the improved 3IVM+ for experimental flow curves in the range of 25°-100°C and strain rates 0.1 s^{-1}, 0.01 s^{-1}, and 0.001 s^{-1}. Fig.2 displays the macrotextures obtained after 50% cold rolling reduction. The skeleton plots in Fig.2c include also the results after 70% cold rolling reduction. In order to account for the texture randomization effect by second-phase particles, a volume fraction of 20% random orientations was added to the final cold rolling textures.

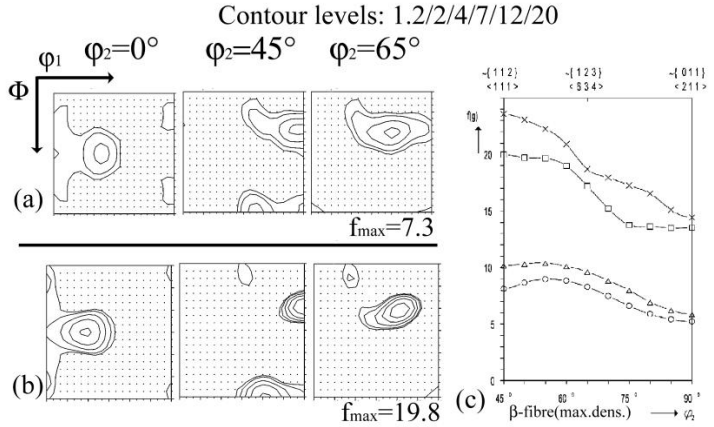

Fig.2 Macrotexture of 50% cold rolled sheet (a) experimental, (b) simulated, (c) Skeleton plot

3.3 Final Annealing

Starting from the simulated cold rolling textures predicted by GIA-3IVM+, a recrystallization simulation with CORe was carried out. With the ClaNG model a dispersoid radius of r_P= 11nm and a volume fraction f_P= 1.06Vol% was calculated, leaving a solute content of $c_{ss,Mn}$=0.43at%. Besides microchemistry also recovery was considered. The results of the recrystallization texture simulations are compared in Fig. 3 in case of the initially 50% cold rolled material with experimental macrotextures obtained after salt bath annealing for 15

minutes at T=350°C for 15 minutes. The experimentally observed grain size was 6µm for the 50% cold rolled material and 8µm for the 70% cold rolled material, which compares to the predictions 17.21µm in case of the 50% cold rolled material and 55µm for the prior 70% cold rolled material.

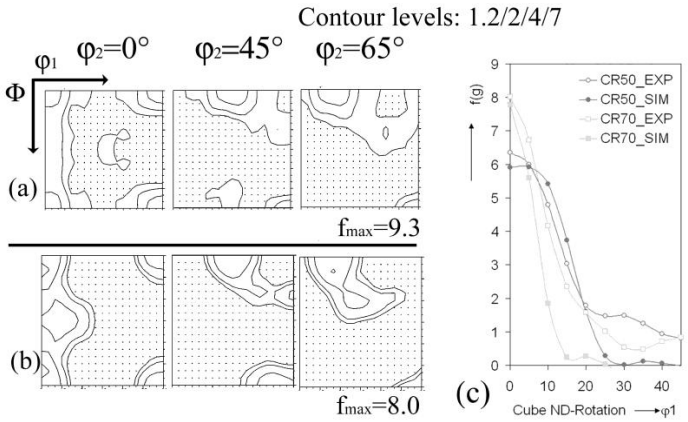

Fig.3 Macrotexture of 50% cold rolled and annealed sheet (a) experimental, (b) simulated, (c) Skeleton plot

Apparently the modeled recrystallization textures show good agreement with the experimental textures. For the 70% cold rolled and annealed material, however, the occurrence of a strong Goss orientation was predicted, which could not be found in the experimental recrystallization texture.

4. Discussion

The predictions of hot-rolling textures obtained from the chosen modeling setup yielded reasonable results. All components present in the experimental texture were also obtained in the simulation, even if the prediction for the centre layer showed slightly higher texture intensities. This results from the too fast texture evolution during deformation as typical for Taylor type texture models. Some deviations were observed for the prediction of the TD rotated Cube component. The rotations found in the experimental texture, could not be traced in the modeled texture. This originates from the GIA model which does not properly predict TD-rotations.

The textures predicted from GIA-3IVM+ show too strong texture intensities, which originate from the homogeneous nature of the model as it allows no consideration of deformation heterogeneities such as in the deformation zone of particles.
Nevertheless, the quality of the predictions is sufficient for a good prediction of recrystallization textures. The simulated final grain size is throughout the whole process in the same order of magnitude as measured by experiment.

5. Conclusions

For a commercial AA3103 alloy a simulation of hot-rolling with subsequent cold rolling and annealing was carried out. Various models were used, to account for the different physical mechanisms occurring throughout the chosen virtual processing chain. It was found that the

incorporation of a discrete recrystallization model gives good texture and microstructure predictions.

Acknowledgement

The authors gratefully acknowledge the assistance of Dr. Cheng Liu (CORUS) with providing material and data. This research was carried out under project number MC4.03176 in the framework of the Strategic Research programme of the Netherlands Institute for Metals Research in the Netherlands (www.nimr.nl).

References

[1] M. Crumbach, G. Pomana, P. Wagner, G. Gottstein," ", in Proc. 1st joint int. conf. on recrystallization and grain growth, edited by G. Gottstein, D.A. Molodov (Springer, Berlin, 2001), 1053.
[2] F. Roters, D. Raabe, G. Gottstein,"Workhardening in heterogeneous alloys – a microstructural approach based on three internal state variables", Acta Mater., **48**, 4181 (2000).
[3] H.W. Hesselbarth, I.R. Göbel, "Simulation of recrystallization by cellular automata", Acta Metall. et Mater., **39**, 2135 (1991).
[4] P. Mukhopadhay, M. Loeck, G. Gottstein, " A cellular operator model for the simulation of static recrystallization ", Acta Mater., **55**, 551 (2007).
[5] M. Crumbach, G. Gottstein, " Modeling of recrystallization textures: I. Model set-up and integration", Acta Mater., **54**, 3275 (2006).
[6] C. Schäfer, G. Gottstein, "Modeling Recrystallization of Al Alloys: A Refined Approach To Particle Stimulated Nucleation ", Mat. Sci. Forum, **558-559**, 1169 (2007).
[7] M. Schneider, "Modellierung und Validierung zeitabhängiger mikrochemischer Prozesse in Al-Legierungen", Ph.D. thesis, RWTH Aachen (2006).

Comparison of two full field approaches for modeling of microstructure evolution of polycrystals

Aruna Prakash[1], Ricardo Lebensohn[2]

[1]Fraunhofer Institute for Mechanics of Materials, Woehlerstrasse 11, 79108 Freiburg, Germany (E-mail: prakash@iwm.fraunhofer.de)
[2]Los Alamos National Laboratory, Los Alamos, NM 87545, USA (E-mail: lebenso@lanl.gov)

ABSTRACT

In this contribution we compare finite element (FE) and fast Fourier transform (FFT) approaches for the prediction of microstructure evolution in viscoplastic polycrystals. Both approaches are 'full-field' approaches and can be used to investigate the heterogeneity of the inter- and intragranular stress and strain fields in a polycrystalline material. The FE approach belongs to the class of crystal plasticity finite element models (CPFEM). It uses the single crystal plasticity constitutive model proposed by Asaro [1]. The model has been successfully used to predict the deformation behavior of a wide range of materials (e.g. [2, 3]). The FFT approach is a relatively new method and was proposed by Lebensohn [4] for polycrystalline viscoplastic materials.

We compare both approaches, not only in terms of their predictive capability, but also in terms of their performance. The models are evaluated for fcc, bcc and hcp materials. The polycrystal is modeled as a 3-D unit cell with periodic boundary conditions. Grains in the unit cell are discretized with sufficient number of elements (FE) or voxels (FFT) in order to capture the deformation inhomogeneities. Preliminary results from simulations of fcc polycrystals have been encouraging. The deformation characteristics along with stresses and evolving texture predicted by both models are almost identical.

[1] R.J. Asaro, "Crystal plasticity", *Journal of Applied Mechanics*, **50**, 921 (1983)

[2] A. Prakash, S.M. Weygand, H. Riedel," Modeling the evolution of texture and grain shape in Mg alloy AZ31 using the crystal plasticity finite element method", *Computational Materials Science,* doi:10.1016/j.commatsci.2008.06.015 (2008)

[3] J. Očenášek, M.R. Ripoll, S.M. Weygand, H. Riedel, "Multi-grain finite element model for studying the wire drawing process", *Computational Materials Science*, **39**, 23–28 (2007)

[3] R.A. Lebensohn, "N-site modeling of a 3D viscoplastic polycrystal using fast fourier transform", *Acta Materialia*, **49**, 2723 (2001)

This work is partially supported by the German research foundation through the grant RI 329 under the framework of the priority program SP1168.

Morphological models of evolving microstructures

Dominique Jeulin

MINES ParisTech, CMM- Centre de Morphologie Mathématique, Mathématiques et Systèmes, 35 rue Saint Honoré, 77305 Fontainebleau Cedex, France
(E-mail: Dominique.jeulin@ensmp.fr)

ABSTRACT

Complex muti-componenent textures in materials can be modeled and simulated by models of random sets [3]. In this presentation, we address the case of evolving microstructures by means of space and time random models, and we illustrate our purpose by three different situations:

· Sequential models, like the color dead leaves model [1], are well suited to reproduce the evolution of interlocked random microstructures, with crystals of various minerals growing from a melt. We will remind some probabilistic properties of this kind of models, making it possible to propose a model identification from micrographs.

· Reaction-Diffusion models [2] mimick the evolution of microstructures under a combination of transport by diffusion and reaction between species. Such models provide very realistic morphologies to generate simulations of porous media like foams, bones, or sintered materials.

· Microstructures under a stress field can progressively damage. Starting from a distribution of random defects, which can be activated under increasing loads, we propose models of evolving random damaged microstructures, which enable us to predict macroscopic stress-strain curves of quasi-brittle random media [4].

[1] D. Jeulin "Dead Leaves Models: from space tesselation to random functions", in Proc. of the Symposium on the Advances in the Theory and Applications of Random Sets (Fontainebleau, 9-11 October 1996), D. Jeulin (ed), World Scientific Publishing Company, pp. 137-156 (1997).

[2] L. Decker, D. Jeulin "3D Spatial time structure simulations by reaction-diffusion models", Acta Stereologica, **18**, n° 2, 247 (1999).

[3] D. Jeulin "Random texture models for materials structures", Statistics and Computing, **10**, 121 (2000).

[4] D. Jeulin "Models of random damage", in Proc.Euromat 2000 Conference, Tours, France, D. Miannay, P. Costa, D. François, A. Pineau (eds), 771-776 (2000).

Multiscale Modeling of Fracture in Aluminum: Constitutive Relation for Interface Debonding from Atomistic Simulations

Vesselin I. Yamakov[1], Erik Saether[2], Edward H. Glaessgen[2]

[1]National Institute of Aerospace, 100 Exploration Way, Hampton, VA 23666
(E-mail: yamakov@nianet.org)
[2]NASA Langley Research Center, Hampton, VA 23681
(E-mail: Edward.H.Glaessgen@nasa.gov)

ABSTRACT

A multiscale modeling strategy using a constitutive-relation based scaling methodology for simulating damage processes related to intergranular fracture in aluminum is discussed. In this strategy, the information from the atomistic level is transferred to the continuum level through constitutive relations governing different damage models. An essential part of the strategy is a methodology for atomistic derivation of a cohesive-zone law and its implementation in cohesive-zone finite-element models for simulating fracture in aluminum. The cohesive-zone law is derived as a statistical mechanics representation of crack propagation through defining a statistical ensemble of atomistic cohesive-zone-model-elements (CZVEs). The constitutive equation of interface debonding is formulated as a statistical average of the traction-displacement states of the CZVE ensemble under the conditions of a steady-state crack propagation. The cohesive-zone law derived by this technique is free of finite size effects and is statistically representative for describing the interfacial debonding of an idealized interface examined at atomic length scales. The sensitivity of the extracted cohesive zone model on the conditions of the simulation, system size and temperature, is discussed for the example of a high-angle $\Sigma 99$ symmetric tilt grain boundary in aluminum. The study is a step towards relating atomistically derived decohesion laws to macroscopic predictions of fracture.

Dislocation depinning transition in a dispersion strengthened steel

B. Bakó,[1,*] D. Weygand,[2] M. Samaras,[1] W. Hoffelner,[1] and M. Zaiser[3]

[1]*Paul Scherrer Institute, 5232 Villigen PSI, Switzerland*
[2]*IZBS University of Karlsruhe, Kaiserstrasse 12, 76131 Karlsruhe, Germany*
[3]*Centre for Materials Science and Engineering, The University of Edinburgh, Edinburgh EH9 3JL, United Kingdom*

Investigation at high temperatures of the dynamic behavior of dislocations, the carriers of plastic deformation attracts growing interest because of its importance for understanding many properties of plastically deformed crystalline materials, closely related to the dislocation patterning and dynamic properties of dislocation motion. Dispersoid strengthening is particularly important for ferritic based structural components used in nuclear applications due to their superior radiation resistance and creep strength at high temperatures. In oxide dispersion strengthened steels the interactions between dispersoids and dislocations determine the material's plasticity.

Discrete dislocation dynamics simulations are used to investigate the dynamics of a driven dislocation line interacting with randomly distributed, incoherent oxide dispersoids that act as pinning centers in a BCC ferritic alloy. The dislocation line undergoes a depinning transition where the order parameter is the mean dislocation line velocity v, which increases in the depinning region from zero as $v \sim (\tau - \tau_c)^{\beta}$ for external resolved shear stresses beyond a threshold value τ_c. The critical stress and critical exponents characterizing the depinning transition are determined numerically, and the observed dynamical behavior is compared with that of a depinning elastic string.

*Electronic address: botond.bako@psi.ch

Using Atomistic Simulations To Inform Mesoscale Simulations Of Microstructural Evolution

Stephen M. Foiles, David L. Olmsted, Elizabeth A. Holm

Computational Materials Science and Engineering Department, Sandia National Laboratories, Albuquerque, NM 87185-1411, USA (E-mail: foiles@sandia.gov)

ABSTRACT

Predicting and controlling the evolution of materials microstructure is one of the central challenges of materials science. The simulation of microstructural evolution requires a detailed knowledge of the properties, including energies and mobilities, of interfaces in the material. We present the results of molecular dynamics simulations of these interfacial properties for a large set of boundaries.

1. Introduction

The grain-level microstructure of a material strongly impacts a wide array of materials properties such as strength, toughness and corrosion resistance to name a few. Therefore, understanding and controlling microstructural evolution is one of the central topics of materials science. The modeling of the evolution of the grain structure is typically performed at the mesoscale where the simulations track the motion of grain boundaries in response to the driving forces acting on the boundaries. At this level, the properties of the boundary that are considered include the boundary energy, the interfacial stiffness and the boundary mobility. Up to about a decade ago, the mesoscale simulations of grain growth made the simplifying assumption that boundary properties were isotropic, in other words all boundaries have the same properties. More recently, there has been substantial effort to include the variation of boundary properties with the crystallography of the boundary[1]. The challenge is that even for planar boundaries there are five macroscopic degrees of freedom that describe the boundary and variation of boundary properties within this space is not well known. In the current work, we use atomic-scale simulation methods to examine the grain boundary energy and mobility throughout this five-dimensional space.

There have been several previous studies of the variation of grain boundary energy with the boundary crystallography[2]. However, these studies only considered boundaries in certain types such as, for example, tilt boundaries about a given axis. In the current work, as discussed below, we consider a more extensive set of boundary geometries that includes both high-symmetry boundaries as well as low-symmetry, essentially general, boundaries. The boundary mobility has been much less studied in the past. There have been a small number of simulations of the mobility for specific boundaries[3]. This reflects the computational effort required to perform mobility simulations. Here we use a recently develop synthetic driving force method [4]

to compute the mobility which has the advantage of being more readily applied to the broad range of boundaries. Thus this work represents the first simulation study of the mobility of a extensive set of grain boundaries.

2. Methods

In order to study grain boundary properties throughout the five dimensional space of the macroscopic grain boundary parameters without arbitrarily considering preselected types of boundaries, we considered all grain boundaries that can be constructed within a specified maximum cell size. We employ periodic boundary conditions within the grain boundary plane. In the direction normal to the boundary, the cell is terminated by free surfaces for the mobility calculations and by free surfaces with the near surface atoms constrained to move as a block for energy minimizations. This setup limits us to studying boundaries with coincident site lattice (CSL) misorientations [5], and rational boundary plane normals. Our approach to choosing a group of reasonably small boundaries, but without imposing other conditions, is to look at all boundaries that can be built in such a simulation cell where the periodic length of each grain along the principal axes of the simulation cell is no more than a maximum length, $L_{\max}$. Taking $L_{\max} = 15a_0/2$, where a_0 is the lattice spacing, gives 388 distinct fcc boundaries, and these are the boundaries considered here. All boundaries with CSL misorientation and rational boundary plane normals can be built in this configuration for large enough $L_{\max}$. While not all boundaries are precisely CSL boundaries, any non-CSL boundary can be approximated arbitrarily well by a CSL boundary. CSL boundaries are often characterized by their Σ value which is the inverse density of coincident sites for that misorientation. The largest Σ in this set of boundaries is 385; the smallest Σ *not* contained in this set of boundaries is 23. There are 72 distinct misorientations represented in the 388 boundaries.

The energy minimization and molecular dynamics simulations were performed using embedded atom method (EAM) interatomic potentials that were developed for Ni by Foiles and Hoyt [6] and for Al that were developed by Ercolesi and Adams[7]. Substantial effort was taken to find a good estimate of the minimum energy of each boundary via an extensive sampling of initial boundary structures that were then optimized using a conjugate gradient algorithm. The initial configurations for each boundary were based on three types of variations: the choice of offset vector between the two crystals (relative displacement of the lattice origins of the two crystals), the placement of the boundary in the direction normal to the two crystals, and which atoms were discarded because they were close to atoms in the other crystal. For each macroscopic geometry, the number of initial structures considered ranged from thousands to tens of thousands. Fig. 1 presents two examples of the results of such an energy search. The energy after the conjugate gradient minimization is plotted for each of the starting configurations used, sorted by increasing energy. Panel (a) shows the results for a Σ111 boundary. About half of the configurations minimize to essentially the same energy, consistent with the possibility that this is the global minimum, at least for the cell size used. Some of the starting configurations minimized to significantly higher energies, demonstrating the need for the search. In particular note that for this case, if a single configuration was considered there is about a 50% chance that one would obtain an incorrect high energy and that the error in the energy could be over a factor of two. Panel (b) shows the results for an asymmetric Σ5 boundary with normals of <100><430>. In this

case more than half of the configurations give essentially the same energy. However, a few configurations give slightly lower energies. This case suggests that even with the extensive sampling performed here, some boundary energies reported in this study may not be global minima. Fortunately, the behavior shown suggests that the errors in those cases are small.

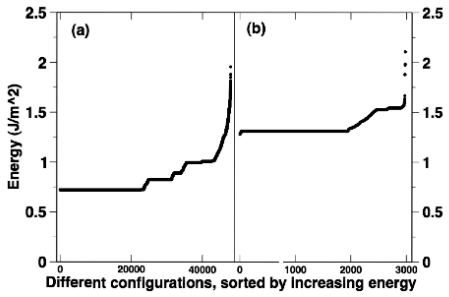

Figure 1. The minimized energy of the set of initial structures discussed in the text for (a) a Σ111 grain boundary and (b) a asymmetric Σ5 (100)/(430) grain boundary. The energies are sorted by increasing energy in the plot.

The mobility of the boundaries was computed using a method proposed by Janssens, et al. [4] that will just be summarized here. In this approach, an artificial potential is added to each atom that depends on how closely the positions of its neighboring atoms match those expected for an ideal fcc lattice with the crystal orientation of one of the grains. Standard molecular dynamics are then used to move the atoms where the forces are determined from the EAM potential and the gradient of this artificial potential. In this way, one of the grains can be made to be energetically favored relative to the other thus providing a driving force for boundary motion. The position of the boundary as a function of time is then monitored to obtain the boundary velocity and the mobility is computed from the ratio of the boundary velocity to the applied driving force. The advantage of this approach is that one can induce boundary motion for arbitrary boundaries and that it can be applied in an automated way to a large number of boundaries. We have compared the mobility computed in this manner with that obtained by Zhang, et al. [8] using an elastic stress driving force and found that the two approaches agree for small driving forces.

3. Results

The computed grain boundary energies for Ni are plotted in Fig. 2 as a function of both the disorientation angle between the grains and the net expansion of the boundary. The corresponding plots for Al are qualitatively similar except for the energy scale. The disorientation angle is the minimum misorientation angle between the grains. The net expansion is the excess volume associated with the boundary per unit boundary area. There are several conclusions that can be drawn from the results. First, disorientation angle by itself is insufficient to determine the boundary energy though the boundary energy does tend to zero for small disorientations as expected. Second, boundaries with the same disorientation but different boundary planes, as typified by the Σ3 boundaries, may have substantially different energies which emphasizes the important role of the boundary plane. Third, he <111> and <100> twist boundaries are systematically low energy. Finally, there is a rough correlation between the grain

boundary energy and the net expansion; boundaries with smaller net expansions tend to have lower energies. However this correlation is not strong enough to be quantitatively useful.

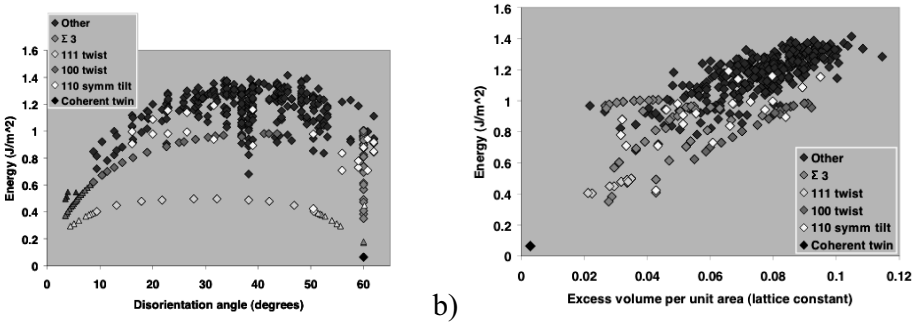

Figure 2. The computed grain boundary energies for Ni plotted against a) the disorientation angle between the two grains and b) the net boundary expansion. Triangles indicate data for boundaries outside the group of 388.

It is typically assumed that the variation of grain boundary energy with the macroscopic degrees of freedom will be similar for various fcc metals. In order to test this concept, Fig. 3 shows a scatter plot of the computed grain boundary energy for Ni and Al. Each point corresponds to the same values of the macroscopic degrees of freedom for each material but the detailed minimum energy atomic structure may be different for the two elements. There is a clear correlation between the energies in the two materials indicating that the variation of the energy with the macroscopic degrees of freedom is similar in Ni and Al apart from an overall scaling factor of about 2.6. There are deviations from this for the <111> twist boundaries including the coherent twin boundary.

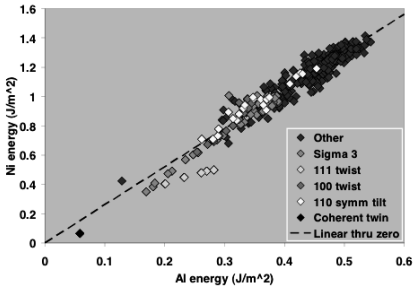

Figure 3. Scatter plot of the computed grain boundary energies for Ni and Al. Each point represents the same macroscopic degree of freedom though the microscopic structures may differ in some cases. The line indicates a linear fit to the data constrained to pass through the origin.

It is interesting to explore how the ratio of the grain boundary energies observed for Ni and Al relate to the ratios of simple materials properties of these metals. We have examined the ratios of a variety of properties including the melting temperature, sublimation energy, vacancy formation energy, stacking fault energy, low index surface energies, and elastic moduli. In all cases the values are multiplied by the required power of the lattice constant to obtain quantities with the same dimensions as grain boundary energy. It has been suggested that boundary energies and surface energies are related. The low-index surface energies are in a ratio of 2.2-

2.3, which is reasonably close to the observed ration of 2.6. The best comparison is with the Voigt average shear modulus, 2.4 or C_{44}, 2.8. (Note that C_{44} is also a shear modulus.) The correlation with shear moduli is physically plausible since grain boundaries can be viewed as dislocation arrays and the elastic strain energy of a dislocation scales with the shear modulus. The correlation of grain boundary energy with C_{44} has been proposed previously by Udler and Seidman[9].

The grain boundary mobility for Ni computed for this set of boundaries at the temperature of 1400 K are presented in Figure 4 as a function of the disorientation angle. Note that due to numerical limitations, we are not able to quantify the mobility below a certain threshold and in these plots all such boundaries are given a value of zero. The first observation is the large variation of the computed mobility; the vertical scale is a log-scale. Recently, there has been discussion of the coupling of shear motion with normal motion of the boundary in the case of planar boundaries [10]. The relative shear motion, the distance of shear in the plane of the boundary divided by the distance moved normal to the boundary, has been computed for each case with significant motion. The rough level of the shear motion is indicated by the symbol on the plot in panel a. Note that the majority of the boundaries with especially large mobilities have large relative shear. The coupling of normal motion with shear is not inhibited for the periodic bi-crystal, planar boundary geometries used in these calculations. However, in a polycrystalline microstructure, such coupled motion would be inhibited and so may not occur in polycrystalline grain growth.

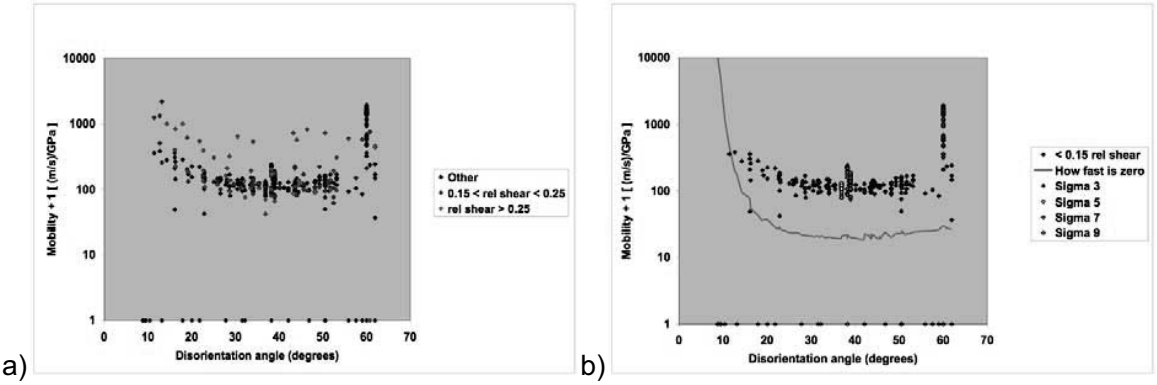

Figure 4. The computed grain boundary mobility for Ni at 1400K plotted as a function of the disorientation angle. In a) the shading reflects the degree to which normal motion and shear are coupled and in b) only the low shear boundaries are included and the shading indicates certain sigma values.The curve indicates the smallest value for which mobility can be reliably computed.

The grain boundary mobilities for the those boundaries which do not have significant shear motion, relative shear of < 0.15, are plotted in panel b. The variation of the mobilities is still large but reduced by the elimination of shearing boundaries. An interesting observation is that the Σ3 boundaries have large mobilities except for the coherent twin, which has extremely low mobility as expected. The behavior of low Σ boundaries is of interest to the field of grain boundary engineered materials. The Σ5 boundary mobilities are very much in line with the overall trend while some of the Σ7 and Σ9 boundaries are somewhat more mobile than other boundaries with similar disorientations. Another unexpected result is that the mobility appears to

increase for moderately small disorientation angles. This is in conflict with the experimental observation that low angle boundaries have low mobility. This observation is still under analysis, but it may be related to the inevitable presence of impurities in the experimental samples.

4. Summary

The grain boundary energy and mobility of 388 distinct grain boundaries have been computed based on EAM potentials for Ni and Al. The results presented here and to be elaborated elsewhere[11, 12] provide insight into the variation of these properties across the five-dimensional space of planar grain boundaries. Current mesoscale models of grain growth will benefit from these calculations either through the development of compact representations of the properties as a function of the boundary crystallography or via interpolative treatments of data such as this.

Acknowledgements

Sandia is a multi-program laboratory operated by Sandia Corporation, a Lockheed Martin Company, for the United States Department of Energy's National Nuclear Security Administration under contract DE-AC0494AL85000.

References

[1] G.S. Rohrer, "Influence of Interface Anisotropy on Grain Growth and Coarsening", Annual Reviews of Materials Research, **35**, 99-126 (2005)

[2] D. Wolf and K.L. Merkle, "Correlation between the structure and energy of grain boundaries in metals", in *Materials Interfaces: Atomic-level structure and properties*, edited by D. Wolf and S. Yip (Chapman-Hall, London, 1992) 87-150.

[3] Z.T. Trautt, M. Upmanyu, and A. Karma, "Interface Mobility from Interface Random Walk", Science, **314**, 632-635 (2006)

[4] K.G.F. Janssens, D. Olmsted, E.A. Holm, S.M. Foiles, S.J. Plimpton, and P.M. Derlet, "Computing the Mobility of Grain Boundaries", Nature Materials, **5**, 124-127 (2006)

[5] A.P. Sutton and R.W. Balluffi, *Interfaces in Crystalline Materials*. 1995, Oxford: Clarendon Press.

[6] S.M. Foiles and J.J. Hoyt, "Computation of Grain Boundary Stiffness and Mobility from Boundary Fluctuations", Acta Materialia, **54**, 3351-3357 (2006)

[7] F. Ercolessi and J.B. Adams, "Interatomic Potentials from First-Principles Calculations: the Force-Matching Method", Europhysics Letters, **26**, 583 (1994)

[8] H. Zhang, M.I. Mendelev, and D.J. Srolovitz, "Computer simulation of the elastically driven migration of a flat grain boundary", Acta Materialia, **52**, 2569-2576 (2004)

[9] D. Udler and D.N. Seidman, "Grain Boundary and Surface Energies of FCC Metals", Physical Review B, **54**, R11133-R11136 (1996)

[10] J.W. Cahn, Y. Mishin, and A. Suzuki, "Coupling Grain Boundary Motion to Shear Deformation", Acta Materialia, **54**, 4953-4975 (2006)

[11] D. Olmsted, S.M. Foiles, and E.A. Holm, "Survey of Grain Boundary Properties in FCC Metals: Grain Boundary Energy", Acta Materialia, submitted.

[12] D. Olmsted, E.A. Holm, and S.M. Foiles, "Survey of Grain Boundary Properties in FCC Metals: Grain Boundary Mobility", in preparation.

Synchronous Parallel Kinetic Monte Carlo

Enrique Martinez

Lawrence Livermore National Lab, Livermore, CA, 94559, USA
(E-mail: enriquemasa@yahoo.es)

ABSTRACT

A novel parallel kinetic Monte Carlo (kMC) algorithm formulated on the basis of perfect time synchronicity is presented. The algorithm is intended as a generalization of the standard n -fold kMC method, and is trivially implemented in parallel architectures. In its present form, the algorithm is not rigorous in the sense that boundary conflicts are ignored. We demonstrate, however, that, in their absence, or if they were correctly accounted for, our algorithm solves the same master equation as the serial method. We test the validity and parallel performance of the method by solving several pure diffusion problems (*i.e.* with no particle interactions) with known analytical solution. We also study diffusion-reaction systems with known asymptotic behavior and find that, for large systems with interaction radii smaller than the typical diffusion length, boundary conflicts are negligible and do not affect the global kinetic evolution, which is seen to agree with the expected analytical behavior. We have studied as well discrete systems via Ising model reaching to the same conclusion. In the latter, boundary conflicts are suppressed using a sublattice algorithm. Both methods, with and without sublattice have been compared. Our method is a controlled approximation in the sense that the error incurred by ignoring boundary conflicts can be quantified intrinsically, during the course of a simulation, and decreased arbitrarily (controlled) by modifying a few problem-dependent simulation parameters.

Kinetic Consequences of Point Defect Energetics and Deformation Mechanisms in Metastable Alloys

Mukul Kabir[1], Timothy T. Lau[2], Sidney Yip[1,2], Krystyn J. Van Vliet[1]

[1]Department of Materials Science and Engineering, Massachusetts Institute of Technology, Cambridge, Massachusetts 02139, USA
[2]Department of Nuclear Science and Engineering, Massachusetts Institute of Technology, Cambridge, Massachusetts 02139, USA
(E-mail: mukulkab@MIT.EDU)

ABSTRACT

Many technologically important metallic alloys are intentionally processed as metastable microstructures comprising a supersaturation of crystal defects. Although the interaction among these multidimensional defects is known to control mechanical properties and deformation mechanisms, the local distribution and kinetics of defects in such complex materials are challenging to resolve experimentally. Hardened steels, body-centered cubic iron supersaturated in both carbon (1 wt %) and vacancies, are an important example of alloys in which deformation behavior is intrinsically coupled to the lattice defects. Here, we determine the energetic properties of point defect microstructures and their concentrations in metastable Fe-C alloys via density functional theory. From these energetics and our predicted defect phase diagrams, we develop a new many-body classical potential, which correctly reproduces the physical properties of such point defects/defect clusters. From this potential, we rapidly survey key defect interactions and apply the nudged elastic band method to calculate migration barriers of statistically abundant defect complexes, as well as the effective self-diffusivity of iron as a function of local chemical composition and mechanical stress. Further, we employ kinetic Monte Carlo to study the dislocation climb rate as a function of defect concentration. For this metastable alloy, we show that self diffusivity and associated deformation rates are controlled by the concentration of carbon-free vacancy clusters.

Stress-induced Phase Transformation in Nanocrystalline UO_2

Tapan G. Desai[1], Blas Uberuaga[2], Paul C. Millett[1], Dieter Wolf[1]

[1] Materials Properties and Performance, Idaho National Laboratory, Idaho Falls, ID 83415
[2] Materials Science and Technology Division, Los Alamos National Laboratory, Los Alamos, NM 87545
(E-mail: tapan.desai@inl.gov)

ABSTRACT

We have performed Molecular Dynamics (MD) simulations using an empirical potential to study stress-induced phase transformation in nanocrystalline UO_2 at T = 1000K. The columnar UO_2 microstructure consists of 6 grains of identical hexagonal shape and diameter (d = 20 nm) in a three-dimensional periodic simulation cell. Under constant-stress tensile loading conditions, we found a phase transformation from the fluorite to α-PbO_2 structure. The heterogeneous nucleation process of this new phase (α-PbO_2) occurs at the grain boundaries and the new phase then grows toward the interior of the grain. To verify that this phase transformation seen in MD simulations is physically reasonable, density functional theory (DFT) calculations were performed. The DFT calculations agree that the α-PbO_2 structure is energetically favored over the fluorite structure under certain tensile conditions. According to our knowledge, experimental validation of this phase transformation is not yet available.

Thermal and Elastic Properties of Fe Nanowires

Herbert M. Urbassek and Luis A. Sandoval

Fachbereich Physik, Technische Universität Kaiserslautern
Erwin-Schrödinger-Straße, Gebäude 46, D-67663, Kaiserslautern, Germany
(E-mail: urbassek@rhrk.uni-kl.de)

ABSTRACT

By means of molecular dynamics simulations we study various finite-size effects on Fe nanowires. In particular, we are interested in the role of shape, size and crystal orientation on the temperature-induced transition from alpha-Fe to gamma-Fe. We study two phonon modes which may be interpreted as dynamical precursors of the martensitic transformations, the longitudinal 2/3(1,1,1) and the transverse T_1 1/2(1,1,0) mode with [1 -1 0] polarization. We use two different kinds of potentials: embedding-atom method potential (Meyer-Entel) [1] and the bond-order potential (Müller et al.) [2], which can describe phase transitions in iron. We explore the feasibility to make multi-scale modeling of the nanowire thermal conductivity.

[1] R. Meyer and P. Entel, "Martensite-Austenite Transition and Phonon Dispersion Curves of $Fe_{1-x}Ni_x$ Studied by Molecular-Dynamics Simulations", Physical Review B, **57,** 5140 (1998).
[2] M. Müller, P. Erhart and K. Albe, "Analytic Bond-Order Potential for BCC and FCC Iron - Comparison with Established Embedded-Atom Method Potentials", Journal of Physics: Condensed Matter, **19,** 326220 (2007).

Atomic Bonding and Properties of Metastable Phase in Al-Cu Alloy

Gao Yingjun, Huang Chuanggao, Zhang Hailin, Wen chunli, Jin Xing

School of Physics Science and Engineering, Guangxi University, Nanning 530004, China
(E-mail: gaoyj@gxu.edu.cn)

ABSTRACT

According to "Empirical Electron Theory of solid"(EET), atomic bonding of metastable precipitations of Al-Cu alloy are calculated. The states of atoms and atomic bonding of metastable precipitations are discussed. These can be used to explain the mechanical properties and thermal stability of metastable precipitations on atomic bonding levels.

1. Introduction

It is well know that Al-Cu alloy is one of the most important precipitation-hardening Al-based alloys. The supersaturated solid solution (SSSS) of Al-Cu alloy as-quenched will increase its strength by ageing. Under the low temperature of artificial ageing for Al-Cu alloy, the precipitation is in the following sequence[1]: SSSS→GPZ→θ''→θ'→stable θ(Al_2Cu). There are different thermal stability of these precipitation GPZs, θ'', θ' and θ, therefore the contribution of each precipitation to strength of alloy is different. Some make alloy strengthening, some make the alloy weakening. The thermal stability of precipitation and its contribution to strength of alloy, are closely concerned in atomic states of precipitation, particularly, are concerned in local atomic bonding of precipitation. The empirical electron theory (EET) [2] of solid, which is established on the basis of Pauling's valence bond theory[3] and the energy band theory, offers a simple and practical empirical method-bond length difference (BLD) method to deal with valence electron structures of complicated system, and has been applied to many fields[4-7]. In this paper the atomic bonding of metastable precipitation in Al-Cu alloy are calculated by using the EET, then its influences on the properties of alloy are discussed.

2. Crystal structure

2.1 FCC cell of Al and Cu

Crystal structures for pure Al and Cu metal are the FCC structure in Fig. 1, lattice constant are a_{Al}=0.40496nm and a_{Cu}=0.36147nm, respectively. Although Cu atoms distribute randomly in matrix at the as-quenched state of the alloy to form the metastable disordered solid solution α(Al)phase, the crystal structure of the solid solution phase is still the FCC. Its crystal structure is the same as the structure of pure Al and Cu metal. To deal with this disorder system of alloy mixed

by Al and Cu atoms, the system can be described by using "Average Atom Model[6]". The cell structure of GPZ is shown in Fig. 2. The lattice constants are a=0.404nm and c=0.380nm.

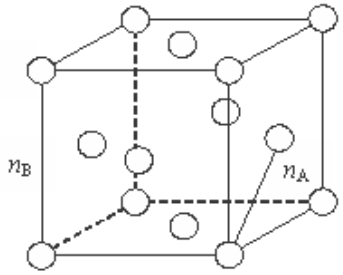

Fig1. Crystal cell structure of Al or Cu

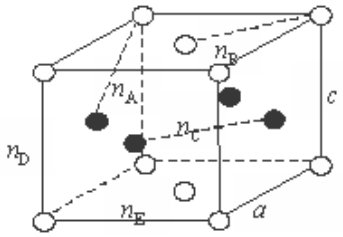

Fig.2 Unit cell of G.P Zone

2.2 Cell structure of θ'' and θ' phase

In ageing of SSSS of Al-Cu alloy, metastable θ'' can not only nucleus in SSSS of matrix, but also directly evolve from GPZ of Al-Cu alloy. The crystal cell θ'' is shown in Fig. 3, with tetragonal structure [6], and its lattice constant are a=0.4040nm and c=0.7680nm. Considering the differentiation of Al atoms surrounding in the side and in the edge of θ'' cell, here Al^1 and Al^2 are used to denote the differentiation of two sorts of Al atoms. With the ageing time lasting, the metastable θ'' can be dissolved and gradually precipitate a new metastable θ' in matrix and with a tetragonal structure. The crystal structure of θ' is shown in Fig.4, its lattice constant are a=0.4040nm and c=0.5800nm.

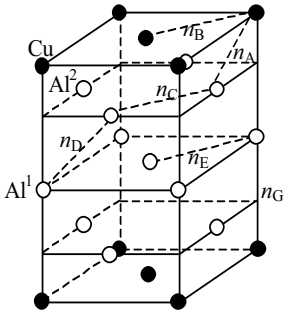

Fig 3 Unit cell of θ'' phase

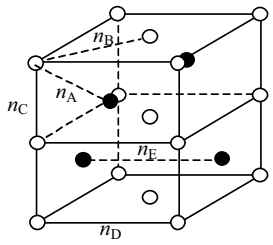

Fig 4 Unit cell of θ' phase

3. Calculation Method

The empirical electron theory (EET) [2] of solids can offer a simple and practical empirical method-bond length difference (BLD) method to deal with valence electron structures of complicated systems. Here main procedure of calculation is given, and the more details are in the Ref.[4-7].

3.1 State of Al atom

According to fundamental hypothesis [2] of EET, the electron configuration relating to ground state of element Al is $3s^2 3p^1$, which is a one-covalence state. Because of the metallic properties of the elements under some conditions, the ***s*** electron is considered to be the lattice electron to form the *h* state from the ground state, while the ***p*** electron is considered to be the electron to form covalence bond in order to ensure the one-covalence state. Let one lattice electron be denoted by Φ, the covalent electron by •, and the empty orbit by ○, then, the *h* state can be represented as follows:

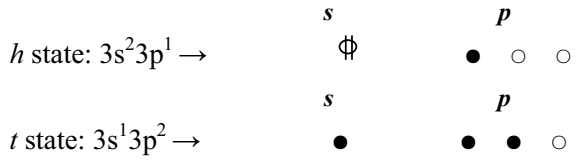

where ⌱ represents two lattice electrons. The *t* state is selected considering the three-covalence state, which often appears in solids and molecules, so the related electron configuration is $3s^1 3p^2$. To ensure the three-covalence state, all of them should be covalent electrons. So the *t* state can be represented as above.

3.2 State of Cu atom

According to the fundamental hypothesis of EET, the *h* state and *t* state of Cu atom in solid are as below [6],

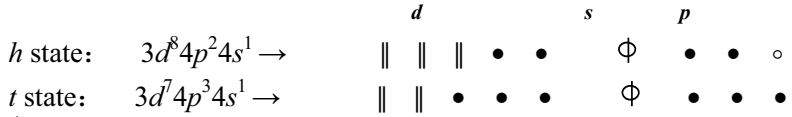

where Φ represents one lattice electron. The covalent electron is represented by •, and the empty orbit by ○, and the nobond electron is represented by ‖. Following the two-hybrid-state of the Al and Cu atoms, the detail hybrid-states of the two atoms are calculated and the detail hybrid-state Tables are listed in Ref. [6].

3.3 Calculation Method

According to EET, the valence electron structure of the metal determines the states of the atoms that form the alloy and the electron distribution of the covalent bonds formed by these atoms. Covalent electrons are distributed in the bonds of the nearest neighbor, the second nearest neighbor and *s*th nearest neighbor. The amount of covalence electrons of each bond (namely bond order n_s) can be represented by the following bond length formula established by Pauling [3],

$$D(n_s) = R^u + R^v - \beta \lg n_s \tag{1}$$

Where $D(n_s)$ is the bond length, R^u and R^v are the single bond radii of u and v atoms, β is constant. The amount of covalence electron in a cell can be represented by the following equation:

$$K_1 n_c^u + K_2 n_c^v = \sum_s I_s n_s \tag{2}$$

Where the numbers of u and v atoms in the cell are represented by K_1, K_2 respectively. n_c^u and n_c^v are the amount of covalent electrons of u and v atoms respectively. I_s is the

equivalence-bond number of n_s. The equivalence-bond number can be calculated according to Ref. [4-5]. For a given structure, if the calculated atom states of the consisting atoms are correct, the theoretical bond lengths $\overline{D}_{n\alpha}$, which are determined by atom state parameters n_c and $R(1)$, should all accord with the experimental bond lengths $D_{n\alpha}$. Therefore, by comparing the theoretical values $\overline{D}_{n\alpha}$, which are calculated from certain atom state, with the experimental one of all covalent bonds in a structure unit, we can determine if the given atom state accords with the actual state. To determine if the theoretical bond lengths $\overline{D}_{n\alpha}$ accord with the experimental one $D_{n\alpha}$, quantitatively, Yu[2] suggested that the absolute value of their different should be less than 0.005 nm under first-order approximation

$$\Delta D_{n\alpha} = \left|\overline{D}_{n\alpha} - D_{n\alpha}\right| < 0.005\text{nm} \tag{3}$$

The formula (3) is the bond length difference (BLD) criterion. According to Ref. [2], the atomic bonding in a cells can be calculated one by one with BLD-criterion, and the detail procedure has been shown in the Ref.[4-5]. The results of the atomic bonding are shown from Tab. 1 to Tab. 3.

4. Discussion

The calculation results are shown from Tab. 1 to Tab. 3. The Al atom and Cu atom in pure Al and Cu metals are in fourth hybrid-state and ninth hybrid-state in Tab.1, respectively. The single-bond-radii of Al atom is $\boldsymbol{R}(1)$ =0.1190nm, and $\boldsymbol{R}(1)$ of Cu atom is 0.11481nm. The covalence electron numbers of Al atom are n_c =2.5296, and that of Cu atom is n_c = 4.5504. The results in Tab. 2 show that when the disorder-solid solution of α-Al phase is formed, the hybrid-state of Al and Cu atoms in alloy do not change, and is the same as the state in pure Al and Cu metal, so the valence electron states of Al and Cu atoms in α (Al) phase can be written as

$$\textbf{Al: [Ne]}(3\boldsymbol{S_f})^{0.4704}(3\boldsymbol{S_c})^{0.7648}(3\boldsymbol{P_c})^{1.7648};\quad \textbf{Cu: [Ar]}(4\boldsymbol{S_f})^{1.0}(4\boldsymbol{S_c})^{0.0}(4\boldsymbol{P_c})^{2.2752}(3\boldsymbol{d_c})^{2.2752}(3\boldsymbol{d_n})^{5.4496}$$

Where $3S_f$ is the free electron of 3*S* orbits, usually as conducting electron; $3S_c$ is the covalence electron in 3*S* orbits, and $3d_c$ is the covalence electron in 3*d* orbits, while the $3d_n$ is the nobond electron in 3*d* orbits. The result in Tab. 2 shows that the hybrid-states of Al atom and Cu atoms have changed in GPZ, falling down to next lower hybrid lever state. The single-bond-radii of Cu atom changes from 0.11481 nm up to 0.11492 nm, and the number of covalence electron change from n_c = 4.5504 down to 4.4006. The electron states of Al and Cu atoms in GPZ are written as

$$\textbf{Al: [Ne]}(3\boldsymbol{S_f})^{1.8266}(3\boldsymbol{S_c})^{0.0867}(3\boldsymbol{P_c})^{1.0867};\quad \textbf{Cu: [Ar]}(4\boldsymbol{S_f})^{1.0}(4\boldsymbol{S_c})^{0.0}(4\boldsymbol{P_c})^{2.2003}(3\boldsymbol{d_c})^{2.2003}(3\boldsymbol{d_n})^{5.5994}$$

Not only the hybrid lever states of Al and Cu atoms in GPZ fall down to the lower lever states comparing with that of matrix of alloy, but also the numbers of covalence electrons in Al and Cu atoms in a cell decrease comparing with that in pure Al and Cu metals, while the strongest Al-Cu covalence bond in GPZ is much bigger than that in matrix. The main reason is that Cu content in matrix of Al-Cu alloy is much low, therefore the number of the covalence electron contributed by Cu atom in matrix is very fewer. Because Cu content in GPZ reaches 50% in GPZ cell, the covalence electron number contributed by Cu atoms in the cell is much greater comparing that in matrix, and so the Al-Cu covalence bond is much stronger. It is the strongest Al-Cu covalence bond when GPZ precipitates in the matrix that makes the bond network in matrix enhance and strengthen alloy.

Table 1 Atomic bondings of Pure Al and Cu metals

Al Cell						**Cu** Cell					
Bond	I_α	$D_{n\alpha}/nm$	$\overline{D}_{n\alpha}/nm$	n_α	$\Delta D/nm$	**Bond**	I_α	$D_{n\alpha}/nm$	$\overline{D}_{n\alpha}/nm$	n_α	$\Delta D/nm$
$D_{nA}^{\text{Al-Al}}$	12	0.28635	0.28633	0.2086	0.00002	$D_{nA}^{\text{Cu-Cu}}$	12	0.2556	0.2551	0.3760	0.0005
$D_{nB}^{\text{Al-Al}}$	6	0.40496	0.40494	0.0045	0.00002	$D_{nB}^{\text{Cu-Cu}}$	6	0.3615	0.3610	0.0065	0.0005
Al: a_0(nm)= 0.40496; σ=4; n_c=2.5296; R(1)(nm)= 0.119						Cu: a_0(nm)= 0.36147; σ=9; n_c=4.5504; R(1)(nm)= 0.11481					

Table 2 Atomic bondings of α-Al and GPZ

α-**Al Cell**						**GPZ** Cell					
Bond	I_α	$D_{n\alpha}/nm$	$\overline{D}_{n\alpha}/nm$	n_α	$\Delta D/nm$	**Bond**	I_α	$D_{n\alpha}/nm$	$\overline{D}_{n\alpha}/nm$	n_α	$\Delta D/nm$
D_{nA}^{S}	12	0.28577	0.28576	0.2116	0.00001	$\boldsymbol{D_{nA}^{\text{Al-Cu}}}$	32	0.27732	0.27676	0.2492	0.00056
D_{nB}^{S}	6	0.40416	0.40414	0.0046	0.00001	$\boldsymbol{D_{nB}^{\text{Al-Al}}}$	8	0.28567	0.28512	0.2170	0.00056
a_0(nm)= 0.40416; Al: σ=4; n_c=2.5296; R(1)(nm)= 0.119						$D_{nC}^{\text{Cu-Cu}}$	8	0.28567	0.28512	0.1665	0.00056
Cu: σ=9; n_c=4.5504; R(1)(nm)= 0.11481						$D_{nD}^{\text{Al-Al}}$	2	0.38000	0.37944	0.0102	0.00056

GPZ: a_0(nm)= 0.40496, c(nm)= 0.380; Al: σ=3; n_c=1.1734; $R(1)$(nm)= 0.119; Cu: σ=8; n_c=4.4006; R(1)(nm)= 0.11492

Table 3 Atomic bondings of θ'' and θ' phase

θ'' Cell						θ' Cell					
Bond	I_α	$D_{n\alpha}/nm$	$\overline{D}_{n\alpha}/nm$	n_α	$\Delta D/nm$	**Bond**	I_α	$D_{n\alpha}/nm$	$\overline{D}_{n\alpha}/nm$	n_α	$\Delta D/nm$
$D_{nA}^{\text{Al2-Cu}}$	32	0.27190	0.27135	0.2702	0.00055	$D_{nA}^{\text{Al-Cu}}$	16	0.24865	0.24870	0.5496	0.00004
$D_{nB}^{\text{Cu-Cu}}$	8	0.28567	0.28512	0.1453	0.00055	$D_{nB}^{\text{Al-Al}}$	8	0.28567	0.28571	0.1602	0.00004
$D_{nC}^{\text{Al2-Al2}}$	8	0.28567	0.28512	0.1908	0.00055	$D_{nC}^{\text{Al-Al}}$	4	0.29000	0.29004	0.1357	0.00004
$D_{nD}^{\text{Al1-Al2}}$	32	0.28567	0.28512	0.1908	0.00055	$D_{nD}^{\text{Al-Al}}$	8	0.40400	0.40404	0.0017	0.00004
$D_{nE}^{\text{Al1-Al1}}$	8	0.28567	0.28512	0.1908	0.00055	$D_{nE}^{\text{Cu-Cu}}$	4	0.40400	0.40404	0.0012	0.00004

θ'': a=0.404nm, c=0.768nm; Al^1: σ_{Al}^1= 4 n_c= 2.5296 R(1)= 0.119nm
Al^2: σ_{Al}^2 =5, n_c=2.897, R(1)=0.119 nm
Cu: σ_{Cu}=7, n_c=4.1170, R(1)=0.11512 nm

θ': a=0.404nm, c=0.580 nm;
Al: σ_{Al}=4, n_c=2.5296, $R(1)$=0.119nm
Cu: σ_{Cu}=13, n_c=4.6208, $R(1)$=0.11477 nm

The results in Tab. 5 show that the state of Cu atoms is in seventh hybrid-order state in θ'' phase, which is lower than the ninth hybrid-state of Cu atoms in pure Cu metal, while the state of the Al atoms nearest neighbor to Cu atom is up to fifth hybrid state, and the state of Al atom second nearest neighbor to Cu atom is still in fourth state. This indicates that when θ'' phase is formed, there are lattice deformations near the region of Cu atom. Because there are strong interaction between the Cu and Al, the hybrid state of Al atom which is the nearest neighbor to Cu atom changes obviously, from fourth state up to fifth state, the covalence electron in Al atom are from 2.5296 up to 2.8974, and form the strong Al-Cu covalence bond. Tab. 3 also shows that the strongest covalence bond is the Al-Cu bond and it reaches na=0.2702, much greater than that in matrix of Al-Cu alloy. When θ'' phase gradually and uniformly precipitate in matrix of Al-Cu alloy, and is coherence with matrix, the whole covalence bond networks in alloy are enhanced, and so the alloy hardening. The atomic states of Al and Cu atoms in θ'' phase can be written as:

$$\mathbf{Al^1: [Ne](3S_f)^{0.4704}(3S_c)^{0.7648}(3P_c)^{1.7648};\quad Cu: [Ar](4S_f)^{1.0}(4S_c)^{0.0}(4P_c)^{2.0585}(3d_c)^{2.0585}(3d_n)^{5.8880}}$$
$$\mathbf{Al^2: [Ne](3S_f)^{01030}(3S_c)^{0.9485}(3P_c)^{1.9485};}$$

After a long ageing time, θ'' become dissolved, then the more stable phase θ' gradually precipitates in matrix of Al-Cu alloy. The calculation results in Tab. 3 show that hybrid state of Al atom in θ' plane does not change, and is the same as Al atom in matrix in fourth hybrid-lever state, while the state of Cu atoms in θ' phase change obviously. Not only Cu atom state in θ' phase changes from the ninth state in pure Cu metal up to thirteen hybrid state in θ', but also its

covalence electron number increase from 4.5504 up to 5.774. The atomic states of Al and Cu atoms in θ' phase can be written as:

$$\textbf{Al: [Ne]}(3S_f)^{0.4704}(3S_c)^{0.7648}(3P_c)^{1.7648};\quad \textbf{Cu: [Ar]}(4S_f)^{1.0}(4S_c)^{0.0}(4P_c)^{2.7887}(3d_c)^{2.7887}(3d_n)^{4.4226}$$

The results in Tab. 3 show that the strongest covalence bond is the Al-Cu bond with n_A = 0.4596 electronic numbers, very much stronger than the strongest Al-Cu covalence bond with n_A=0.2702 in θ'' phase. It is the strongest Al-Cu covalence bond network in θ' phase that θ' phase is of higher thermal stability than the θ'' phase, therefore the θ'' phase is easier to dissolve than θ' phase in higher temperature.

4. Conclusion

In early ageing stage, the state of Cu atoms in θ'' phase is in seventh hybrid-lever state, which is lower than the ninth hybrid-state of Cu atoms in pure Cu metal, while the state of the Al atoms nearest neighbor to Cu atom is in fifth hybrid-state, and the state of Al atom second nearest neighbor is still in fourth state. It is this reason that the whole bond network is enhanced in alloy, then the strength of alloy will increase. After a long ageing time, the Al atom state in θ' plane does not change, and is the same as Al atom in matrix in fourth hybrid state, while the state of Cu atoms in θ' phase change to up state, and cause to the strongest Al-Cu covalence bond. It is the strongest covalence bond network in the θ' phase that the θ' phase is of higher thermal stability than the θ'' phase is, therefore the θ'' phase is easy to dissolve than θ' phase is in higher temperature.

Acknowledgments

This work was financially supported by the Natural Science Foundation of China under Project number 50061001and 50661001; supported by the Science Foundation of Guangxi Province under Project number 0832029 and 0639004.

References

[1] S-K. Sou, M. Takeda, “Thermal stability of phase in Al-Cu alloy”, Mater. Sci. Forum, 475-479, 353(2005).
[2] Yu Ruihuang, The Empirical Electron Theory of Solids. *Chinese Science Bulletin.* 23, 217 (1978).
[3] L. Pauling, The Nature of The Chemical Bond. San Simeon: Cornell University Press. (1960).
[4] Guo Yongquan , “Magnetic Properties and Electronic Structures of $LaT_{3-x}Al_x$(T=Fe,Co)”, *J. Phys. Chem.* B, 102, 9(1998).
[5] Liu Zhilin, “Catalysis mechanism and catalyst design of diamond”. *Metall. Mater.Trans.* A. 30, 2757 (1999).
[6] Gao Yingjun. “Atomic bonding and properties of precipitates in Al-Cu alloy”, *J. Electronic Materials*, 35, 1801(2006).
[7] Gao Yingjun, “Atomic Bonding and Phase transformation of Al-Cu-Mg Alloy” *J Alloy & Compound,* 441, 241(2007).
[8] L. F. Mondolfo. Structure and Property of Aluminum Alloys. London: Butterworths Press (1976)

The impact of short range order on Fe-Cr thermodynamics

Giovanni Bonny[1], Paul Erhart[2], Alfredo Caro[2], Roberto C. Pasianot[3,4], Lorenzo Malerba[1], Magdalena Serrano de Caro[2]

[1]SCK-CEN, Nuclear Materials Science Institute, Boeretang 200, B-2400 Mol, Belgium, (E-mail: Gbonny@sckcen.be, Lmalerba@sckcen.be)
[2]LLNL, Chemistry, Materials and Life Sciences Directorate, L-367, Livermore, CA 94550, USA, (E-mails: Erhart1@llnl.gov, Caro2@llnl.gov, Serranodecaro2@llnl.gov)
[3]CAC-CNEA, Departamento de Materiales, Avda. Gral. Paz 1499, 1650 San Martín, Pcia. Buenos Aires, Argentina
[4]CONICET, Avda. Rivadavia 1917, 1033 Buenos Aires, Argentina
(E-mail: Pasianot@cnea.gov.ar)

ABSTRACT

Using atomistic simulations of Fe-Cr alloys and computational thermodynamics techniques, we study the influence of short range order, SRO, on the location of the α-α' miscibility gap. By comparing the random alloy to the short range ordered alloy, we extract the contributions of SRO to the free energy coming from the enthalpy of mixing, and from the vibrational and configurational entropies. The obtained phase diagram is compared to the standard Fe-Cr phase diagram and additional experimental data. We conclude that the effects of SRO are significant, doubling the solubility limit of Cr at low temperatures (≈ 300 K), and that this effect is mainly due to the contribution of SRO to the enthalpy.

1. Introduction

The Fe-Cr binary is a model alloy for ferritic/martensitic steels, whose use as structural materials is envisaged in all future nuclear systems, from GenIV to fusion. Both experiments [1] and *ab initio* results [2] suggest a negative heat of mixing and short range ordering (SRO) in the Fe-rich region. Starting from about 8-10 at.% Cr, the heat of mixing changes sign and α-α' phase separation occurs. In a recent atomistic study [3], these phenomena were explained quantitatively in terms of ordering and precipitation. Using computational thermodynamics and the latter study as a starting point, the effects of SRO on the thermodynamics of this alloy, in particular the equilibrium phase diagram is analysed and a critical comparison with the standard phase diagram [4] is made.

2. Methodology

In this work the free energy per particle at a given temperature for a given configuration is obtained through a thermodynamic integration between the state of interest and a reference state

(here the Einstein crystal). Full details regarding this methodology are given in [5]. To describe the atomic interactions an interatomic potential developed by Caro et al. [6] was used, which is the same as in the recent study regarding SRO [3] and describes the Fe-Cr alloy reasonably well.

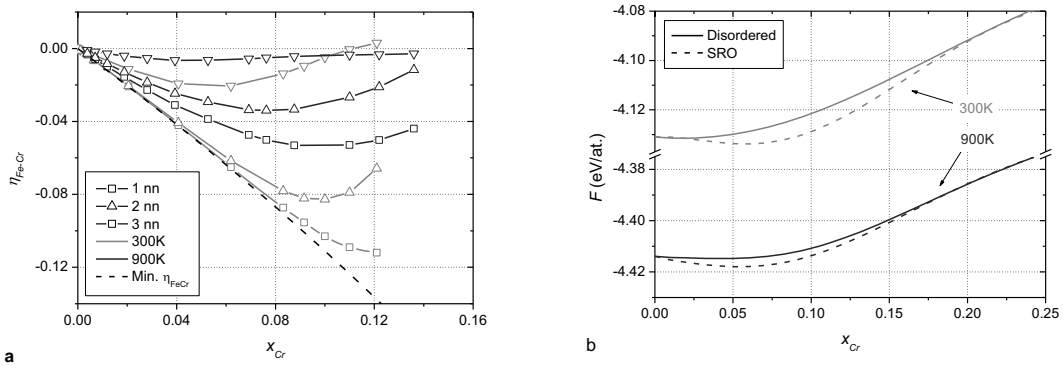

Figure 1. (a) The SRO parameter for the first three neighbour shells at 300 and 900 K. (b) Isotherms of the free energy surface for the short range ordered and random alloy.

The free energy was calculated for both random and short range ordered configurations. The short range ordered configurations were obtained from [3], where they were quantified by the Warren-Cowley parameter, η^{ν}, as a function of Cr content x and temperature T, as shown in Fig. 1a. The thermodynamic integration provides an exact value (i.e. without approximation) for the enthalpy and the vibrational entropy of a given configuration. The configurational entropy of mixing for a given state, however, can not be obtained without further approximation. For the binary perfectly random alloy, the configrational entropy can be approximated by the regular solution expression for the configurational entropy,

$$S_{Rand} = -k_B\left[x\ln(x) + (1-x)\ln(1-x)\right], \tag{1}$$

where k_B denotes the Boltzmann constant. In the case of SRO, the cluster variation method entropy in pair approximation is used to express the configurational entropy. Within this approximation the configurational entropy including pairs up to n-th nearest neighbour distance in a bcc lattice becomes [5],

$$S_{CVM}^{(n)} = S_{Rand} + k_B \sum_{n=1}^{n} \left\{ Z^n \left[x\ln(x) + (1-x)\ln(1-x)\right] - \frac{Z^n}{2}\left[p_{AA}^n \ln(p_{AA}^n) + 2p_{AB}^n \ln(p_{AB}^n) + p_{BB}^n \ln(p_{BB}^n)\right] \right\}. \tag{2}$$

Here $\{p_{AA}, p_{AB}, p_{BB}\}$ denote pair-probabilities which are uniquely defined as a function of η and x [5]. It is clear that for uncorrelated pairs Eqn (2) reduces to Eqn (1). As shown in Fig. 1a, the correlation between pairs decreases fast with increasing distance (i.e. η converges to zero with increasing distance).

3. Results and discussion

Two isotherms at 300 and 900 K are shown in Fig. 1b. In this plot the free energy from the random and short range ordered alloys is compared. It is clear that the isotherms for the short range ordered alloy are significantly lower (i.e. the difference is larger than the numerical error) than the isotherms of the random alloy. Further investigation [5] has attributed this difference mainly to the enthalpy, rather than the configurational and vibrational entropy.

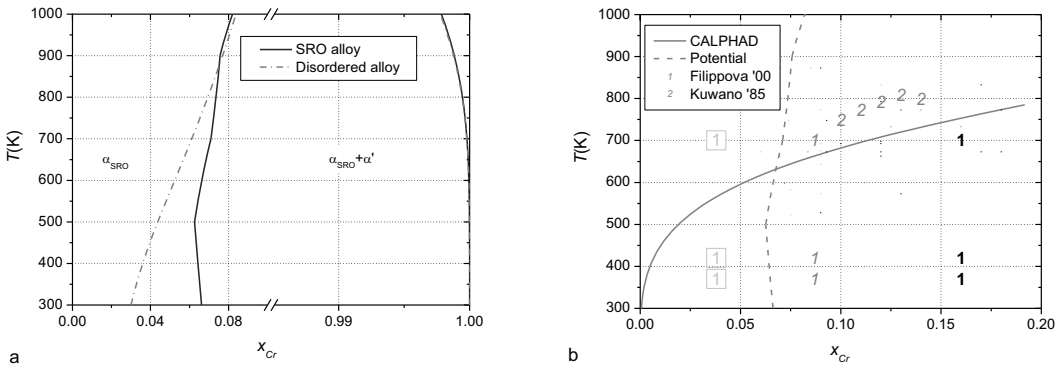

Figure 2. (a) The phase boundaries for the short range ordered and random alloy. (b) The phase diagram obtained from our simulations compared with experimental data.

The shift in free energy introduced by SRO is translated into a shift and steepening of the Fe-rich phase boundary presented in Fig. 2a. The phase boundary is shifted towards the Cr-rich side by approximately 4 at.% Cr at low temperature, an amount that implies doubling the solubility limit of Cr in the α phase. This shift, however, decreases fast with increasing temperature and disappears at about 900K, even though SRO is still present as shown in Fig. 1a. This observation suggests that the sudden disappearance of SRO due to the magnetic transition from ferro to para-magnetism (at Curie temperature, $T_{Curie} \approx 1050$ K) will not have a drastic impact on the phase diagram. Therefore the phase boundary is expected to show a smooth transition at the Curie temperature. At the Cr-rich side the phase boundary remains unchanged, as expected, since the Cr-rich alloy does not exhibit SRO.

In Fig. 2b our prediction for the Fe-rich phase boundary is compared with the standard CALPHAD phase diagram (in the range of the ferro-magnetic phase outside the range of formation of the σ-phase) [4] and with some experimental low temperature data points from the works of Filippova et al. [7] and Kuwano [8], which include data from both irradiation and thermal ageing experiments, respectively. In the plot, the square (green) points denote observed SRO, the bold (black) points denote precipitates observed, and the italic (red) points denote estimated phase boundary points by the respective authors. The low temperature data comes from irradiated samples. It is the belief of the authors that the irradiation conditions merely accelerated the precipitation process, as no precipitates were induced, while SRO was detected. Taking this into account, the experimental data points are used to describe the low temperature phase diagram, other than CALPHAD, which does not take low temperature data into account.

Fig. 2b shows that the phase boundary obtained from our simulations matches the experimental data quite closely at temperatures below 700 K, with the salient feature that the phase boundary is very steep, and the Cr solubility at low *T* very large, in contrast to the commonly accepted Fe-Cr phase diagram [4]. At higher *T*'s the discrepancy is significant as the miscibility gap does not close under melting temperature ≈ 2000 K, whereas the ferromagnetic metastable (neglecting the slow σ phase formation) miscibility gap closes around 900 K [4]. In spite of the outlined limitations, we still believe that the potential gives an adequate description of the Fe-Cr alloy in the low temperature region (<700 K).

4. Conclusions

In this paper the effect of short range order on the thermodynamic properties of Fe-Cr alloys has been investigated by means of atomistic simulations. The free energy of the short range ordered alloy is significantly lower than the random alloy at low temperature, and still noticeably lower at high temperature: the decrease of free energy due to short range order is mainly attributed to the decrease in enthalpy. The difference on the configurational and vibrational entropy between the short range ordered and random alloy is of minor importance.

The effect of short range order on the Fe-rich phase boundary is significant at low temperature, where the boundary is shifted towards the Cr-rich region almost doubling the solubility limit compared to the phase boundary for the random alloy. At about 900K the phase boundaries obtained from the short range ordered alloy and the random alloy coincide, while short range order is still observed. The Fe-rich phase boundary seems to match well the experimental phase diagram below 700 K but is in striking contrast above.

5. Acknowledgments

This work was performed under the auspices of the U.S. Department of Energy by LLNL under Contract DE-AC52-07NA27344 with support from the LDRDP and FMP. The work is also partially funded by FP7/2007-2011 under grant agreement number 212175 (GetMat project). RCP acknowledges partial support from CONICET-PIP 5063 and UNSAM c032.

6. References

[1] I. Mirebeau, M. Hennion, and G. Parette, Physical Review Letters, **53**, 687 (1984).
[2] P. Olsson, I.A. Abrikosov, and J. Wallenius, Journal of Nuclear Materials, **321**, 84 (2003).
[3] P. Erhart, A. Caro, M. Serrano de Caro, and B. Sadigh, Physical Review B, **77**, 134206 (2008).
[4] J-O. Andersson and B. Sundman, Calphad, **11**, 83 (1987).
[5] G. Bonny, P. Erhart, A. Caro, R.C. Pasianot, L. Malerba, and M. Caro, "The influence of short range order on the thermodynamics of Fe-Cr alloys", submitted to Physical Review B (2008).
[6] A. Caro, D.A. Crowson, and M. Caro, Physical Review Letters, **95**, 075702 (2005).
[7] N.P. Filippova, V.A. Shabashov, and A.L. Nikolaev, The Physics of Metals and Metallography, **90**, 145 (2000).
[8] H. Kuwano, Transactions of the Japan Institute of Metals, **26**, 473 (1985).

The Microstructure Evolution of Oxide Particles in a Dispersion strengthened steel

Takashi Segi, Masayuki Inaba, Takashi Yamasaki, Takashi Watanabe and Takanari Okuda

Kobelco Research Institute, Inc., Nishi-ku, , Kobe, Hyogo 615-2271, Japan
(E-mails: segi.takashi@kki.kobelco.com, inaba.masayuki@kki.kobelco.com, inaba.masayuki@kki.kobelco.com, yamasaki.takashi@kki.kobelco.com, watanabe.takashi@kki.kobelco.com, okuda.takanari@kki.kobelco.com)

ABSTRACT

The oxide dispersion strengthened (ODS) ferritic steel is the first candidate cladding tube material of the fast breeder reactor for the excellent irradiation resistivity and creep strength at elevated temperature due to the fine distribution of nano size particles. The mechanisms of the ultra fine oxide particles distribution in the Fe-Cr matrix is not known yet. It is confirmed that the sample steel prepared by the mechanical alloying method contains the yttrium oxide cluster by using a synchrotron radiation X-ray fine structure measurements. However it was too difficult to make clear the more detail structure experimentally. Thus the first principle cluster method and molecular dynamics calculation were applied to simulate the evolution process of fine oxide particles. The electronic structure calculation predicts that the interstitial sites of oxygen atom in Fe-Cr bcc structure matrix. The effect of additional elements such as Al and Ti on the nano-particle growth is discussed by the molecular dynamic calculation.

Ab initio study of solutes and defects in FeCr

Pär Olsson, Christophe Domain

EDF R&D, Département Matériaux et Mécanique des Composants, Les Renardières, F-77250 Moret-sur-Loing, France (E-mail: par.olsson@edf.fr)

ABSTRACT

Reduced activation ferritic/martensitic steels are candidate structural materials for Gen IV fission reactors as well as for future fusion reactors. It is imperative for the modeling of these steels to understand the behavior of binary FeCr alloys and the role of the minor solute elements. Electronic structure calculations in the framework of density functional theory have been used in order to study the thermodynamic effects of the minor solutes and their interactions with interstitial and vacancy type defects in both Fe and FeCr matrixes. The stability of interstitial clusters has been investigated and found to be significantly less stable in Cr rich precipitates than in an FeCr matrix. The *ab initio* predictions have been used as input parameters for atomistic kinetic Monte-Carlo studies of the microstructural evolution.

This work has been partially supported by the European Commission within the project GETMAT (FP7-212175). A large part of the calculations were performed on the supercomputers at Centre de Calcul Recherche et Technologie (CCRT) in the framework of an EDF-CEA contract.

Structural Reordering at Wafer Bonded Interfaces and Quantum Dots using Molecular Dynamics Relaxation with Analytic Bond Order Potentials

Kurt Scheerschmidt

Max Planck Institute of Microstructure Physics, Halle, Saxony-Anhalt, Germany
(E-mail: schee@mpi-halle.de)

ABSTRACT

Structural Reordering at Wafer Bonded Interfaces and Quantum Dots using Molecular Dynamics Relaxation with Analytic Bond Order Potentials Kurt Scheerschmidt and Volker Kuhlmann Max Planck Institute of Microstructure Physics, Weinberg 2, D-06120 Halle, Germany Molecular dynamics (MD) simulations have been performed to study atomic processes related to the reordering at interfaces and relaxation of nanostructures [1,2]. To enhance MD, we use the bond order potential (BOP) based on the tight binding (TB) model [3], as it preserves the essential quantum mechanical nature of atomic bonding, yet abandons the electronic degree of freedom. In addition, BOP achieves O(N) scaling - beyond ab initio methods - by diagonalising the orthogonal TB-Hamiltonian recursively and is recognized as a fast and accurate model for atomic interaction. It allows to explore the dynamics of systems on macroscopic time and length scales on the atomic level that are beyond the realm of ab initio calculations on present computers. The resulting semi-empirical many body potential is transferable to describe phases and configurations not in the parameter fit - a feature not found in other empirical potentials. Moreover, transferability extends to different kinds of materials, where only the parameters need to be refitted. In our implementation of BOP4 we have retained a number of angular terms related to certain bonds between neighbouring atoms and contribute up to 40%, but were ignored previously.. Fig. 1 shows resulting minimum structures at wafer bonded interfaces comparing Tersoff and BOP4+ potentials, and Fig. 2 the pair, bond angle-, and torsion angle distribution for the interface of Fig. 1 indicating a higher potential stiffness of BOP. The recalculated structures are used to explain electron microscope contrasts and electronic interface properties.

[1] K. Scheerschmidt, in: Theory of Defects in Semiconductors, D.A. Drabold, S. Estreicher (Eds.), Topics in Applied Physics, Springer Verlag 2006, Chapter 9, pp. 213-244.
[2] K. Scheerschmidt and V. Kuhlmann, Int. J. Mat. Res. 98 (2007) 11. [3] V. Kuhlmann and K. Scheerschmidt, Phys. Rev. B 75 (2007) 014306.

Computational Modeling of Interactions between Slip-systems and Grain Boundaries that lead to Fracture Initiation

Thomas Bieler[1], Martin Crimp[1], Carl Boehlert[1], Leyun Wang[1], Yiyi Yiyi[1], Philip Eisenlohr[2], Franz Roters[2], Dierk Raabe[2], Wenjun Liu[3], Gene Ice[4], Darren Mason[5]

[1]Michigan State University, Michigan, USA
[2]Max-Planck-Institut für Eisneforschung, 40237 Düsseldorf, Germany
[3]Argonne National Laboratory, Argonne, Illinois, USA
[4]Oak Ridge National Laboratory, Oak Ridge, Tennessee, USA
[5]Albion College, Albion, Michigan, USA
(E-mail: bieler@egr.msu.edu)

ABSTRACT

Most modeling approaches developed so far assume pre-existing flaws or cracks in order to predict the growth of damage. To identify fundamental rules for identifying strong and weak grain or phase boundaries in the context of a deformation path, quantitative measurements of (i) the orientations of crystals on either side of interfaces, (ii) the boundary orientation, (iii) the activated deformation systems on either side of the boundary, and (iv) the local strain history within the grains on either side of an interface are necessary. Recent characterization of localized deformation processes that lead to microcracking at grain boundaries has led to identification of fracture initiation parameters that can that predict relatively weak vs. strong boundaries for a given deformation state. This concept has been shown to be effective in ambient temperature deformation of a duplex TiAl alloy and in creep of a cobalt based fcc superalloy. Further investigations will be presented to identify whether the same paradigm is effective in commercial purity titanium. Combined use of digital image correlation to measure local strains, orientation imaging microscopy to track grain orientations, electron channeling contrast imaging to detect dislocation activity, and 3-D x-ray identification of local orientations and orientation gradients, are used to identify local deformation phenomena in the vicinity of grain boundaries. Computational modeling of highly characterized microstructural regions is used in comparison with experiments to evaluate the accuracy of crystal plasticity finite element models (CP-FEM) that provide slip based information that can be difficult to obtain experimentally. Progress towards implementing fracture initiation parameters into the CP-FEM microstructural modeling context will be presented.

Experimental Observations of Evolving Microstructures

[1]Erik M. Lauridsen, [2]Wolfgang Ludwig, [3]Richard W. Fonda, [4]Peter W. Voorhees

[1]Materials Research Department, Risø-DTU, Frederiksborgvej 399, 4000 Roskilde, Denmark (E-mail: erik.mejdal@risoe.dk)
[2]European Synchrotron Research Facility, BP 220, 38043 Grenoble cedex, France (E-mail: ludwig@esrf.fr)
[3]Naval Research Laboratory, Washington, DC 20375, USA (E-mail: Richard.fonda@nrl.navy.mil)
[4]Northwestern Univ, Dept Mat Sci & Engn, 2220 Campus Dr, Evanston, IL 60208 USA (E-mail: p-voorhees@northwestern.edu)

ABSTRACT

In recent year's development in scientific computing capabilities have allowed for significant increase in complexity and size of microstructure simulations. Hence, it is now feasible to model the evolution of real 3D microstructures – and of statistical significant sizes. To complement these new simulation capabilities a parallel effort focussing on obtaining 3D experimental microstructures has been carried out within the past 5-10 years throughout the materials science community. In this presentation recent progress in non-destructive 3D characterization of evolving microstructures will be demonstrated. Common for the techniques presented is that they are based on intense synchrotron radiation and that they provide detailed 3D images of the evolving microstructures which are directly compatible with simulation tools like e.g. Monte Carlo, Phase field or Finite elements. The details and limitations of the applied experimental techniques will be discussed and examples of coupling between experimental data and simulations will be given.

Morphology and Growth Modes of Metal-Oxides Deposited on $SrTiO_3$

J. Wohlwend, C. Boswell, R. Behera, S.R. Phillpot, S.B. Sinnott

Department of Materials Science and Engineering, University of Florida, Gainesville, FL, 32611-6400
(E-mail: ssinn2003@yahoo.com)

ABSTRACT

Classical molecular dynamics simulations are used to examine the growth of SrO, TiO_2, and $SrTiO_3$ (STO) thin films on STO surfaces. In particular, the simulations consider the deposition of molecular beams of varying compositions of SrO and TiO_2 and the deposition of stoichiometric STO clusters at incident energies ranging from 0.1 to 10.0 eV/atom onto the (001) surface of STO. The simulations thus allow us to determine the influences of particle size, composition, and incident energy on the resulting thin film. Additionally, the influence of STO surface termination layer (SrO vs. TiO_2) on thin film growth is considered. In the case of SrO thin film deposition, smooth, ordered films are produced for all of the incident energies considered and for both surface terminations. In contrast, in the case of TiO_2 deposition, three-dimensional islands are formed under all conditions. These predictions are in agreement with experimental data. In the case of mixed beams of SrO and TiO_2, amorphous films are created. However, when alternating layers of SrO and TiO_2 are deposited, films are created with compositions similar to that of bulk STO. Lastly, the deposition of STO clusters produce films that resemble nanocrystalline materials. The simulations indicate the factors that influence the production of these differing morphologies.

This work is supported by the National Science Foundation under grant number DMR-0426870.

Porous Media Microstructure Reconstruction using Pixel-based and Object-based Simulated Annealing - Comparison with other Reconstruction Methods

[1]Alysson Diógenes, [1]Amanda Corrêa, [1]Luís dos Santos, [1]Vicente Fernandes, [2]Carlos Appoloni, [1]Celso Fernandes

[1]Sata Catarina Federal University, Florianópolis, Santa Catarina, Brazil (E-mail: nunes@lmpt.ufsc.br, amanda@lmpt.ufsc.br, emerich@lmpt.ufsc.br, fernandes@lmpt.ufsc.br, celso@lmpt.ufsc.br)
[2]State University of Londrina, Londrina, Brazil (E-mail: appoloni@uel.br)

ABSTRACT

The reservoir rocks physical properties are usually obtained in laboratory, through standard experiments. These experiments are often very expensive and time-consuming. Hence, the digital image analysis techniques advances are a very fast and low cost methodology for physical properties prediction, knowing only geometrical parameters measured from the rock microstructure thin sections. This research presents a new method for reconstruction porous media using the relaxation method simulated annealing. Using geometrical parameters measured from rock thin sections, it is possible to construct a microstructure tridimensional (3D) model. We assume statistical homogeneity and isotropy and the 3D model maintains porosity spatial correlation, chord size distribution and d3-4 distance transform distribution for a pixel-based reconstruction and spatial correlation for a object-based reconstruction. The 2D and 3D preliminary results are compared with microstructures reconstructed by truncated Gaussian methods.

Grain Growth Modeling By A Three Dimensional Vertex Dynamics Simulation

Ling Yue[1], Daniel Weygand[1], Peter Gumbsch[12]

[1]University of Karlsruhe, izbs, Kaiserstr. 12, 76131 Karlsruhe, Germany,
(E-mail: Daniel.Weygand@izbs.uni-karlsruhe.de)
[2]Fraunhofer Institut für Werkstoffmechanik IWM, Wöhlerstr. 9-11,
79108 Freiburg, Germany

ABSTRACT

Grain growth modeling by a three dimensional vertex dynamics simulation Ling Yue, D. Weygand, P. Gumbsch The grain growth for STO is investigated by a three dimensional vertex dynamics model. In this investigation a systematic study of the influence of structure dependent grain boundary properties on statistical observables, e.g. grain size distribution function, grain growth dynamics and correlation function between grain size and number of neighboring grains is presented. These results improve the interpretation of experimental observations on grain growth in STO ceramics as performed within the INCEMS [1] project. The three dimensional vertex dynamics model for grain growth is an interface tracking model [2]. In this approach grain boundaries are discretized and their time evolution is derived from the minimization of the grain boundary (GB) energy. The GB energy is dissipated by the motion of the GBs and triple lines. The original model [2,3] has been extended to handle disorientation and inclination dependent GB energies and mobilities and triple line drag. The improved vertex model is used to explore the three-dimensional analogue of the Neumann-Mullins law. Orientation dependent anisotropic GB properties for STO from experiments are included in the model. The system with anisotropic GB properties is studied and the results of two dimensional cuts through simulated grains structures are compared to experimental observations.

[1] INCEMS: Interfacial Materials - Computational and Experimental Multi-Scale Studies, EU-funded NMP3-CT-2005-013862 http://www.mf.mpg.de/INCEMS/index.html
[2] D. Weygand, Y. Brechet, J. Lepinoux, and W. Gust, Phil. Mag. B **79,** 703, (1999).
[3] D. Weygand, Y. Brechet, J. Lepinoux, Interface Science 7, 287, (1999).

Financial support of the EC under the project number NMP3-CT-2005-013862 (INCEMS) is gratefully acknowledged.

A Coupled Model for Recrystallisation and Creep of Zirconium Alloys

L. Saintoyant[1], L. Legras[1], Y. Bréchet[2]

[1]Electricité de France, R&D division, Material and Mechanics of Components Departement, Les Renardières, 77818 Moret-sur Loing Cedex, France (E-mail: lucie-externe.saintoyant@edf.fr, laurent.legras@edf.fr)
[2]SIMaP - Laboratoire de Themodynamique et Physico-Chimie Métallurgiques, Grenoble INP, Domaine Universitaire Grenoble, BP75, 38402 Saint Martin d'Hères Cedex, France (E-mail: yves.brechet@simap.grenoble-inp.fr)

ABSTRACT

Cold deformed Zr alloy submitted to stress at temperature above 400°C undergo simultaneous recrystallisation and creep. As a consequence, the initial state of the material (uniformly deformed and exhibiting a strong texture) evolves into a complex composite structure where recrystallised grains are imbedded into a non recrystallised matrix, both components of this "composite" having different textures. In addition, the respective volume fractions of the two "phases" of this composite are evolving with time while recrystallisation proceeds. In order to model the macroscopic creep behaviour of such an evolving microstructure, one has to integrate a model for recrystallisation kinetics, a polycrystalline model allowing for at least two major texture components, and a "composite approach" allowing for phases of different hardness. The strategy proposed in the present paper is to rely on internal variable models for grains behaviours [1], on a physically based recrystallisation model [2] and on an advanced polycrystalline plasticity model [3]. This integrated model is the main topic of the present paper. In order to validate this type of models, and to identify the physical parameters, a serie of experiments at various scales have been performed. TEM and SEM analysis of crept materials allows to characterize microstructural evolutions. EBSD and TEM orientation mapping using selected area diffraction allows to quantify texture evolution. Macroscopic tensile creep tests provide the experimental data to be modelled. The comparison between the results of the coupled model described above, and the macroscopic creep deformation is discussed.

[1] J. Dunlop, Y. Bréchet, L. Legras, and Y. Estrin, "Dislocation Density-Based Modelling of Plastic Deformation of Zircaloy-4", Materials Science and Engineering A, **443**, 77 (2007).

[2] J. Dunlop, Y. Bréchet, L. Legras, and H.S. Zurob, "Modelling Isothermal and Non-Isothermal Recrystallisation Kinetics: Application to Zircaloy-4", Journal of Nuclear Materials, **366**, 178 (2007).

[3] P. Pilvin, "Approches Multiéchelles pour la Prévision du Comportement Anélastique des Métaux", Ph.D. thesis, Université de Paris VI (1990).

Multiscale Modeling of Grain Growth

[1]Anthony Rollett, [1]Seth Wilson, [2]Christopher Roberts, [3]Moneesh Upmanyu

[1]Carnegie Mellon University, Pittsburgh, PA 15213, U. S. A.
(E-mails: rollett@andrew.cmu.edu, sethrw@cmu.edu)
[2]Carpenter Technology (CRoberts@cartech.com)
[3]Colorado School of Mines, Golden, CO 80401 USA (mupmanyu@Mines.EDU)

ABSTRACT

Grain growth is a classical problem in materials science that has wide significance for control of microstructure and grain size dependent properties. Grain size is often controlled by introducing second phase particles that exert a pinning effect on grain boundaries. Simulation of the "Zener" pinning of grain growth requires a mesoscopic approach that, even on supercomputers must use second phase particle fractions above 1%, instead of the more typical 0.1-0.5%. New results with careful attention paid to the spatial correlation of particle positions relative to boundaries has shown how it may be possible to nucleate abnormal grain growth. Multiscale modeling is required when solute drag is included because the characteristic length scale for boundary-solute interaction is a few nanometers, as opposed to the micron scale for most grain growth problems. A combined approach is described that uses molecular dynamics for quantifying solute interactions at the atomistic scale and phase field or level set for modeling grain growth at the mesoscale. The ultimate goal of the work is to be able to understand the causes of abnormal grain growth in the presence of second phase particles that may also be evolving.

Implementation of Grain Boundary Property Database for Simulation of Microstructure Evolution based on Realistic Grain Orientations

Byeong-Joo Lee, Je-Wook Jang

Department of Materials Science and Engineering,
Pohang University of Science and Technology, Pohang 790-784, Republic of Korea
(E-mail: calphad@postech.ac.kr)

ABSTRACT

Micro- or meso-scale simulations such as Phase Field or Monte Carlo are widely used for prediction of microstructure evolution in polycrystalline materials. In addition to the valuable insight into the governing mechanism or how to control the microstructure, such simulations provide input data for larger scale simulations (FEM, for example) to predict more practical materials properties. However, it is a common experience that the results of the above mentioned micro-scale simulations are highly sensitive to the grain boundary or interface energy and mobility values given as input data. In order to perform more realistic simulations it is straightforward that realistic values of misorientation, energy and mobility (especially their misorientation dependency) for grain boundaries or interfaces should be used. However, it should be noticed that there exists an infinite number of grain boundaries and interfaces with different misorientation and inclination angles. The difficulty in identifying and arranging all possible grain boundaries or interfaces has been a long problem and prohibited realistic simulations for microstructure evolution. In the present work, a method how to identify a grain boundary (or interface) between two arbitrarily oriented grains and how to arrange all possible grain boundaries (or interfaces) to construct a grain boundary property database will be proposed. Atomistic computation techniques to calculate grain boundary (or interface) energy, diffusivity or mobility will also be introduced. Then it will be shown that the constructed grain boundary (or interface) property database can be successfully implemented in micro-scale simulation codes for prediction of microstructure evolution based on realistic grain orientations.

Modeling and Simulating Polycrystalline Micro Structures: Power Diagrams vs. Particles

Martin Kühn[1], Martin O. Steinhauser[2]

[1]Fraunhofer Institute for Industrial Mathematics (ITWM), Fraunhoferplatz 1, D-67663 Kaiserslautern, Germany (E-mail: Martin.Kuehn@itwm.fraunhofer.de)
[2]Fraunhofer Ernst-Mach Institute for High-Speed Dynamics (EMI), Eckerstrasse 4, D-79104 Freiburg, Germany (E-mail: Martin.Steinhauser@emi.fraunhofer.de)

ABSTRACT

Power diagrams are a generalization of Voronoi diagrams for arbitrary dimensions [1]. A new modeling and optimization scheme for power diagrams in three spatial dimensions based on the statistics of experimental data obtained from cross-section images of polycrystalline materials is presented [2]. The new optimization scheme based on the grains' area and perimeter distributions can be employed to obtain realistic three-dimensional polycrystalline structures which subsequently can be used for numerical FEM simulations. The optimization scheme is applied to high-performance ceramics and the results of shock-impact simulations of the obtained polycrystalline structures are presented. The obtained numerical results agree well with experimental findings concerning fracture and failure behavior of ceramics at high strain rates. Alternatively, we investigate the fracture and failure behavior of polycrystalline materials within the framework of particle dynamics simulations [3] and contrast this method with results obtained from the FEM simulations. We present results for uni-axial quasistatic load simulations which are used for customizing our particle potential parameters to some typical material properties of ceramics. We show that a simple physical model based on particles is capable of reproducing salient features of ceramic behavior upon high strain loadings.

[1] M.O. Steinhauser, "Computational Multiscale Modeling of Fluids and Solids – Theory and Applications", Springer, Berlin, Heidelberg, New York (2008).
[2] M. Kühn, and M. O. Steinhauser, "Modeling and Simulation of Microstructures Using Power Diagrams: Proof of the Concept", Applied Physics Letters, **93**, 034102 (2008).
[3] M.O. Steinhauser, K. Grass, E. Strassburger, and A. Blumen "Impact Failure of Granular Materials – Non-Equilibrium Multiscale Simulations and High-Speed Experiments", Int. Journal of Plasticity, in press, available online (2008).

Grain Growth Mechanisms in Bounded Geometries

Daniel Weygand[1], MarcVerdier[2], Joël Lépinoux[2]

[1] University of Karlsruhe - TH, KIT; izbs, Kaiserstr 12, D76131 Karlsruhe
(E-mail: Daniel.Weygand@izbs)
[2] SIMaP, INPG, CNRS, UJF; Campus Grenoble, F38042 St Martin d'Hères

ABSTRACT

The improvement of global performances in semiconductor devices is limited by the increase of resistivity of metallic line interconnections. Therefore, the control of the time evolution of grain boundaries structures in complex geometries is required. This process is simulated in 2D using the vertex dynamics method extensively applied to bulk problems. This work focus on the evolution of the grain microstructure in films, as a function of its width, with or without a (111) texture enforced along borders.

1. Introduction

Since the integration's scale of interconnects is below 100 nm, roughly the mean free path of electron in Cu, electron scattering takes place at fixed boundaries but also on the remaining grain boundaries. Therefore, the control of the time evolution of grain boundaries structures in complex geometries is required. This work aims at examining the evolution of the grain microstructure in copper lines in the so-called Damascene line structure with a line width in the range of 30-200 nm. Industrially, this geometry is obtained by first patterning a line in the substrate followed by the deposition of a conformal thin diffusion barrier layer and finally by filling up by Cu the line and an overburden continuous thin film. Detailed experimental work by Carreau et al. [1] shows an effect of the overburden film on the final resistivity of the line. The investigated geometry represents a 2D cross section of the Damascene structure in form of a «T» composed of a film (the Cu overburden film) above a narrow rectangle (i.e. the line connection seen end-on) on the substrate side (see Fig. 3). A 2D grain structure is first generated and relaxed then this geometrical mask is applied to get a realistic initial microstructure. Whatever the overburden film thickness, surface effects like grooving will be ignored to simplify.
The evolution of the microstructure is first studied in pure grain growth in bands in isotropic conditions to ensure the absence of artifacts due to the introduction of fixed boundaries. Then a typical initial {111} texture is enforced on the diffusion barrier/metallic film interfaces for all grains in contact with the substrate as observed experimentally. The orientation of the remaining grains is selected at random. Then preliminary results are presented about the final geometry, without or with imposed (111) texture. The technique to compute the evolution of grain populations have been extensively applied to bulk problems (i.e. with periodic boundary

conditions) by Weygand et al. [2-3] within the last decade and more recently to grain growth in encapsulated film, therefore the basic principles will not be recalled here.

2. From infinite medium to a finite width band

2.1 Kinetics of grain growth

The main difference between infinite medium and a film is well-known : due to the finite thickness of the film grain growth cannot proceed indefinitely following a $t^{1/2}$ law as in infinite systems. Depending on the film thickness versus the initial grain size, a transient stage appears more or less rapidly, preceding a saturation stage which ends when grains adopt the so-called "bamboo" structure, i.e. when grain boundaries are normal to the interfaces with an average spacing of the order of the film thickness. Figure 1 illustrates this effect through the comparison of grain size evolution with time and for three band different thickness. At the beginning, the different curves are superimposed, then the time exponent clearly decreases with the thickness band; similarly the time to reach saturation decreases, too.

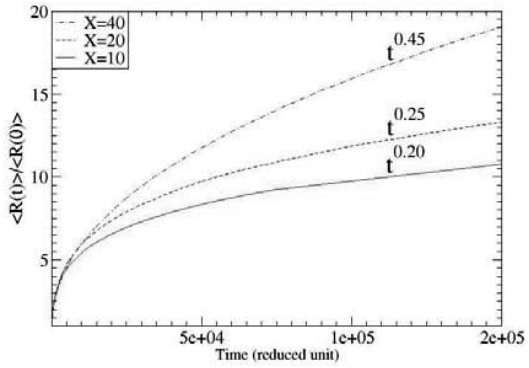

Figure 1: Effect of X, the ratio of the band thickness and initial grain size, on grain growth. For X=10, the final size is almost the equilibrium "bamboo" size.

2.2 Imposing a (111) texture

Experimentally it is observed that the layer of grains initially in contact with the substrate exhibits a (111) texture due to the lower surface energy of this orientation. Here it is necessary to give some details about the computation procedure. Indeed, in the bulk, grain growth is driven by the reduction of the total grain boundary energy, where the misorientation between adjacent grains determines the energy and the mobility of grain boundaries (for sake of simplicity we restrict present investigation to pure isotropic cases). Along a border to the substrate, the driving force is determined by the crystallographic orientation of the intersection plane of grains and the border. For that a true 3D orientation procedure is applied to the grain population and the intersection plane is calculated along borders. To set a (111) texture, we simply impose the orientation of grains along borders to be close to (111) in the initial state. To mimic experimental

conditions the following simple conditions were imposed for surface energies: between grain boundaries, γ=1 (in reduced units); between (111) grains and a border (to simplify all borders are given the same properties), γ=2; between other grains and a border, γ=2+Cos(α) where α is the equilibrium angle between the substrate and the grain boundary between a (111) grain and a grain of different orientation, at such triple junctions.

2.3 Effect of a (111) texture

The main effect of a (111) texture is to introduce a competition between initially (111) oriented grains and other grains reaching the borders. The only way for such a bulk grain to reach a border is to be much larger than the (111) grains. Then whether such grains continue to grow at the expense of neighboring (111) grains depends mostly on the value of α. If wetting is efficient enough, all invaders are systematically repelled back into the bulk. It is even the most efficient growing mechanisms of (111) grains along borders. The asymptotic critical value of Cos(α) preserving the predominance of (111) grains along borders is about 0.4 for present conditions; however the thinner the band the smaller this critical value. Figure 2 shows two different scenarii for a fairly large film: i) Cos(α)=0.25, the (111) grains remains small and vanish before saturation is reached ii) Cos(α)=0.65, the (111) grains continuously expand and finally fill all the film.

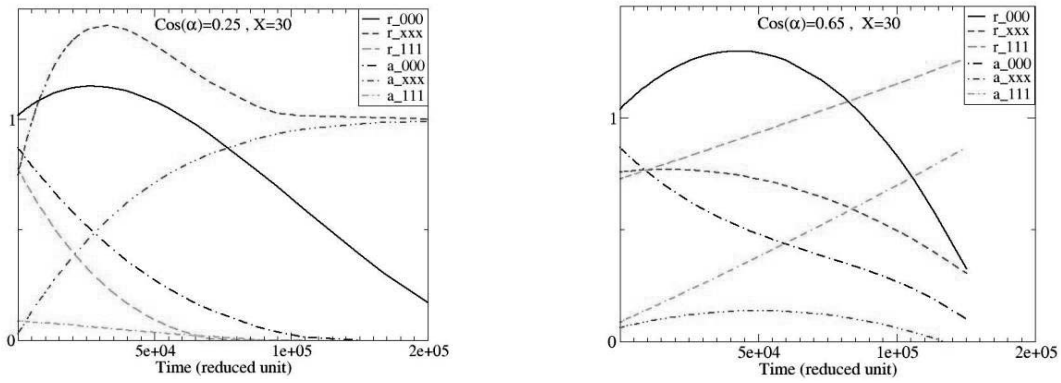

Figure 2. Effect of the value of Cos(α) on the competition between (111) grains along borders and those arriving from the bulk. “a” area fraction; “r”: normalized radius; “111” (111) border grains; “xxx” other border grains; “000” bulk grains. Note the effect of α on the kinetics.

3. From a band to the via geometry

In first approximation the via geometry behaves like two bands. The tip of the line is likely to affect the grain structure depending on the line depth. Similarly the coupling between the film and the line depends on relative thickness of the film and the line. Nevertheless, imposing a sharp transition between the two parts, i.e. a right angle, is a strong condition which prevent extensive exchanges between the grain populations of the two parts, even in absence of imposed (111) texture. Indeed, the grain structure tends to block with grain boundaries aligned either

parallel to one or the other border meeting at a corner or at 45° angle, which considerably reduce grain boundary motion in the vicinity of the corner. Imposing a (111) texture along all borders even amplifies this blockage process, as each border has its preferred grain orientation and therefore an exchange at a corner become almost impossible.

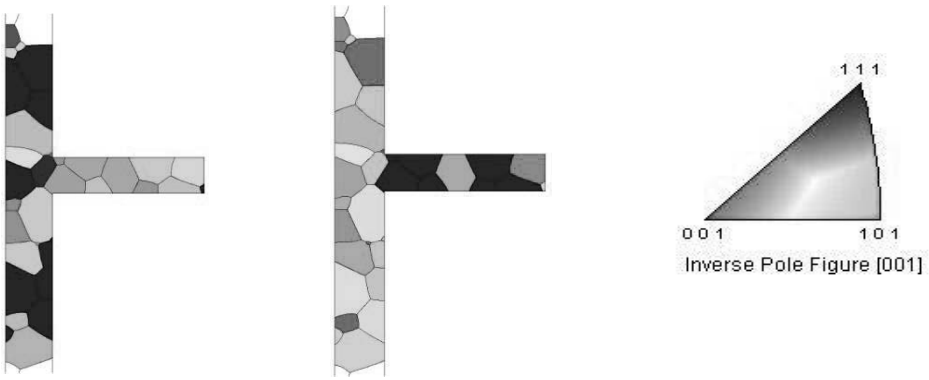

(a) (b) (c)

Figure 3. Texture along the vertical (a) and horizontal (b) directions, during annealing, with color conventions (c) Periodic boundary conditions are applied to the vertical film. In the coupling region between the via and the film there is no clear advantage to one of the two grain populations; here Cos(α)=0.45.

6. Conclusion

Texture effects have been investigated mostly in films. Simulations reveal that depending on the advantage in terms of surface energy, (111) grains initially found along borders might sustain or vanish. In any cases border (111) grains exhibit a smaller size as experimentally observed, and slow down the grain growth kinetics. With present conditions, the coupling of grain evolution in the film and the via are very limited due to efficient blockage at the two right angle between the via and the film.

Acknowledgements

This work has been supported by the french ANR project Cristal N° 06-NANO-024.

References

[1] V. Carreau, S. Maitrejean, M. Verdier, Y. Brechet, A. Roule, A. Toffoli, V. Delaye, G. Passemard, “Evolution of Cu microstructure and resistivity during thermal treatment of damascene line: Influence of line width and temperature”, Microelec. Eng., **84**, 2723 (2007).

[2] D. Weygand, Y. Brechet, and J. Lepinoux, “Zener pinning and grain growth: a two-dimensional vertex computer simulation”, Acta-Materialia, **47,** 961 (1999).

[3] D. Weygand, Y. Brechet, and J. Lepinoux, “On the nucleation of recrystallization by a bulging mechanism: a two-dimensional vertex simulation”, Phil. Mag. B, **80**, 1987 (2000).

Coupling of Direct Finite Element Simulations of Semi-solid Behaviour into Large Strain Deformation Processes

Devashish Fuloria[1], Peter D Lee[1], Warren Poole[2]

[1]Department of Materials, Imperial College London, South Kensington, London, UK
(E-mails: d.fuloria@imperial.ac.uk, p.d.lee@imperial.ac.uk)
[2]University of British Columbia, British Columbia, Canada
(E-mail: warren.poole@ubc.ca)

ABSTRACT

Twin roll casting is one method of directly producing aluminium alloys in near net shape at a fraction of the energy costs of conventional DC casting / hot rolling. However, in some alloys defects can form during the very large strains imposed on the semi-solid material. The formation of these defects cannot be simulated without improved models of the constitutive behaviour of the semi-solid dendrites. Direct finite element simulations of the deformation of semi-solid dendrites were performed using 3D geometries generated via x-ray micro-tomography. These microstructural simulations were combined with high temperature compression tests performed on a Gleeble 3500 thermo-mechanical simulator to derive constitutive equations of the high temperature deformation behaviour semi-solid Al-Cu alloys as a function of: temperature, fraction solid, microstructure, and strain rate. This new micro-scale model derived constitutive equation was implemented in to a macro-model of twin roll casting. The resulting multi-scale model was validated using real-time, in-situ, microfocal x-ray observation of semi-solid deformation processes in aluminium alloys.

Self-Lubrication of Metal Surfaces by Subgrain Evolution During Wear

Corbett C. Battaile, Somuri V. Prasad, and Joseph R. Michael

Sandia National Laboratories, P.O. Box 5800, Albuquerque NM 87111,
(E-mail: ccbatta@sandia.gov)

ABSTRACT

Wear can lead to complex mechanical and microstructural evolution near the worn surface, and these changes can impact the properties of the material. Wear experiments were conducted on Ni single crystals in carefully controlled crystallographic orientations. The formation of microstructure and its effects on wear behavior were found to be sensitive to the crystallography. In particular, wear along <211>-type directions on {110}-type surfaces induced the formation of a nanocrystalline surface layer that served to lubricate the interface. A phenomenological model was developed to analyze the material's wear response at the mesoscale. The model includes the effects of asperity-mediated contact, crystal plasticity, subgrain formation, and grain boundary sliding, and will be used to explain the mechanisms underlying crystallographically-sensitive nanocrystal formation and its effect on friction.

Sandia is a multiprogram laboratory operated by Sandia Corporation, a Lockheed Martin Company, for the United States Department of Energy under contract DE-AC04-94AL85000.

A Level Set Framework for the Numerical Modelling of Primary Recrystallization

Roland E. Logé, Marc Bernacki, Heba Resk, Yvan Chastel, Thierry Coupez

MINES ParisTech, CEMEF – Center for Materials Forming, CNRS UMR 7635, BP 207, 06904 Sophia Antipolis Cedex, France (E-mail: Roland.Loge@ensmp.fr)

ABSTRACT

A generic model for recrystallization in metals that provides quantitatively correct predictions of crystallographic orientations and grain size distributions has long been sought to fill a critical link to model material processing from start to finish. To date, no such theory exists. Grain growth or recrystallization, like many similar state-altering processes that are driven by thermal energy and internal energy of structural defects are not very well understood. Multiscale models are therefore in principle needed to fully describe recrystallization phenomena in a generic way [1,2,3]. Over the last decade, considerable progress has been made in the numerical simulation of primary recrystallization [4]. Common approaches include the Monte Carlo (MC) method [5], the Cellular Automaton (CA) method [5], the phase field method [6] and the level set method [7,8].

In this work, a new level set framework is proposed [8], for the modelling of static primary recrystallization in a polycrystalline material, i.e. where grain boundary motion is due to bulk stored energies. It is shown that the proposed formulation, associated to adaptive anisotropic automatic remeshing, is an efficient and accurate tool. Nucleation phenomena can also be described consistently with experiments.

Test cases are used to validate the model by comparison with other recrystallization models. More complex 2D and 3D simulations are explored, starting from deformed states where realistic FE computations of the stored energy field within the aggregate have been obtained using crystal plasticity based constitutive laws. Finally, the approach is shown to easily adapt to the description of dynamic recrystallization.

[1] D., Rollett, Progress in Mat. Sci., **42**, 77 (1997)
[2] G. Kugler, R. Turk, Comp. Mat. Sc., **37**, 284 (2006)
[3] M. Bernacki & al, Comp. Meth. in Mat. Sc., **7**, 142 (2007)
[4] M.A. Miodownik, J. of Light Metals, **2**, 125 (2002)
[5] A.D. Rollett, D. Raabe, Comp. Mat. Sc., **21**, 69 (2001)
[6] L.Q. Chen, Scripta Metall. Mater., **32**, 115 (1995)
[7] H.-K. Zhao & al, J. Comp. Phys., **127**, 179 (1996)
[8] M. Bernacki & al, Scripta Mat., **58**, 1129 (2008)

Financial support for this work has been provided by the European Commission through contract no NMP3-CT-2006-017105.

Coupling of Atomistic and Meso-scale Phase-field Modeling of Rapid Solidification

J. Belak, P.E.A. Turchi, M.R. Dorr, D.F. Richards, J.-L. Fattebert, M.E. Wickett and F.H. Streitz

Lawrence Livermore National Laboratory
PO Box 808, L-45, Livermore CA 94550
(E-mail: belak@llnl.gov)

ABSTRACT

Meso-scale models have proven extremely successful at predicting the qualitative aspects of microstructure formation and evolution [1]. Unfortunately, quantitative prediction has been limited due to the difficulty in representing the lower length-scale information within the continuum models. Here, we have focused on the phase-field model primarily because of our capability to represent the continuum order parameter in terms of the positions of the atoms. The order parameter represents the local state of the material, whether solid or liquid or, for example, we calculate the local orientation in a crystal from the positions of the surrounding atoms and represent the orientation using the same quaternion order parameter we use in our continuum adaptive-mesh phase-field code.

Recently, phase-field models have been introduced to model the crystallography during polycrystalline microstructure evolution [2,3]. Here, we assess these models with molecular dynamics and phase field simulations that overlap in time and space. Large parallel computers have enabled molecular dynamics simulations of sufficient scale to observe the formation of realistic microstructure [4]. We compare the two methods by calculating the phase-field order parameter (quaternion) from the atomic coordinates and drive the order parameter dynamics with the molecular dynamics. Results will be presented for the solidification of tantalum.

[1] L.-Q. Chen, Annu. Rev. Mater. Res. **32**, 113-1140 (2002).
[2] R. Kobayashi and J.A. Warren, Physica A, **356**, 127-132 (2005).
[3] T. Pusztai, G. Bortel and L. Granasy, Europhys. Lett, 71, 131-137 (2005).
[4] F. H. Streitz, J. N. Glosli, and M. V. Patel, Phys. Rev. Lett. 96, 225701 (2006).

This work performed under the auspices of the U.S. Department of Energy by Lawrence Livermore National Laboratory under Contract DE-AC52-07NA27344.

A Phase Field Crystal Model for Interfacial Evolution Under Stress

P.W. Voorhees[1], K-A Wu[1], K Thornton[2], K.R. Elder[3]

[1]Dept. Materials Science and Engineering, Northwestern University, Evanston IL
(E-mail: p-voorhees@northwestern.edu)
[2]Dept. Materials Science and Engineering, University of Michigan, Ann Arbor MI
[3]Department of Physics, Oakland University, Rochester MI

ABSTRACT

Phase field crystal models have been used to describe a wide range of phenomena from grain growth to solidification. The strength of the method lies in its ability to follow the atomic scale evolution of a process on diffusive timescales. Using this approach the effects of an applied stress on the stability of a solid-liquid interface has been examined. We find that the results of the simulation agree well the predictions of linear stability theory. In the nonlinear regime cusps develop in the solid-liquid interfacial morphology. Unlike standard phase field models, in the phase field crystal model dislocations nucleate at the tip of the cusps and relieve the applied stress. We have extended the model to the case of thin film growth where there is a large density difference between the solid and vapor. To address this large difference we couple a phase field crystal model with a second field describing the average density change between the solid and liquid. Using this approach we can observe steps on surfaces, dipolar stress fields at step edges, and the growth of the thin film from the vapor.

A Phase Field Investigation of the Dynamics of the Martensitic Transition

Alphonse Finel[1], Umut Salman[2], Oleg Shchyglo[2]

[1]ONERA, BP 72, Chatillon, France (E-mail: Alphonse.Finel@onera.fr)
[2]Centre National de la Recherche Scientifique, France
(E-mail: umut.salman@onera.fr, oleg.shchyglo@onera.fr)

ABSTRACT

We will present a recent Phase Field analysis of the dynamics of the martensitic transition. When slowly driven by an external force, a martensitic transition is often characterized by a random sequence of avalanches whose amplitudes and durations display power-law distributions other several decades. This indicates that the transition from austenite to martensite proceeds without characteristic length and time scales, which is the signature of criticality. We present a comparative investigation of this critical dynamics in athermal martensite using both a Time-Dependant-Ginzburg-Landau modeling and a lagrangian method that takes into account inertial effects.

Phase Field Simulation of Void Growth in Irradiated Materials

Srujan K. Rokkam[1], Paul C. Millett[2], Dieter W. Wolf[2], Anter El-Azab[1,3]

[1]Mechanical Engineering Department, Florida State University, Tallahassee, FL 32310
(E-mails: srokkam@fsu.edu, anter@scs.fsu.edu)
[2]Materials Science Department, Idaho National Laboratory, Idaho Falls, ID 83415
(E-mails:paul.millett@inl.gov, dieter.wolf@inl.gov)
[3]School of Computational Science, Florida State University, Tallahassee, FL 32306

ABSTRACT

We present a phase field model for void formation in irradiated metals. The void growth dynamics is characterized by the spatial and temporal evolution of vacancy concentration fields as well as an order-parameter that distinguishes the void and solid regions. We derive a free energy functional that is based on point-defect thermodynamics. The vacancy fluxes and modulations are formulated using a Cahn-Hillard equation. The model also accounts for cascade-induced vacancy production and fluctuations, as well as the nucleation and annihilation of vacancies at void surfaces. Details pertaining to the phenomenological description of the above processes and model capabilities are discussed for the case of pure metals as an example.

1. Introduction

Structural materials in nuclear power systems are subject to neutron irradiation conditions which displaces atoms from their regular lattice sites, producing large numbers of vacancy-interstitial (Frenkel) pairs. The consequent defect fluxes and point defect chemistry can lead to a variety of microstructural features, which can in turn induce physical changes in the material, and adversely affect its mechanical performance. A very important microstructural evolution aspect in this regard is the nucleation and growth of voids (or cavities) which results in swelling of the structural materials [1]. Voids in irradiated materials are three-dimensional clusters of vacancies that precipitate due to a high supersaturation above the thermodynamic equilibrium [2]. In this communication, we present a phase filed model for void nucleation and growth in irradiated pure metals, in which the nucleation and growth (or shrinkage) of voids occurs due to the kinetic evolution of vacancy concentration fields only. The effect of self-insterstials, which we neglect in the present paper, will be incorporated in future work. This paper is organized as follows: the phase-field formulation is briefly described in Section 2, followed by sample numerical results in Section 3, and concluding remarks in Section 4.

2. Phase field model

A diffuse-interface phase field formulation is used to decribe the interface evolution between vacancy agglomerates (or voids) and the solid matrix in nonequilibrium conditions that exist

during irradiation. The void-matrix interface is characterized by an order parameter, $\eta(\mathbf{x},t)$, which varies continously from $\eta=0$ in the matrix phase to $\eta=1$ in the void phase over a narrow diffuse interface. The vacancy distribution in the system is described by the concentration field $c_v(\mathbf{x},t)$. Consistent with the Cahn-Hilliard definition of free energy [3], we describe the non-equilibrium free energy of an irradiated metal comprising vacancies, voids and regular matrix regions as:

$$F(c_v,\eta)=\int_V\Big[h(\eta)G^m(c_v)\ +\ w(c_v,\eta)\ +\ \kappa_v|\nabla c_v|^2+\ \kappa_\eta|\nabla\eta|^2\Big]\,dV\,, \tag{1}$$

where $G^m(c_v)=N\left(E_v^f c_v+k_BT[c_v\log(c_v)+(1-c_v)\log(1-c_v)]\right)$ is the local bulk free energy density of the system which accounts for both the enthalpic and entropic contribution of the vacancy defects; $h(\eta)$ is a shape function which varies continuously from $h(\eta=0)=1$ (in the matrix phase) to $h(\eta=1)=0$ (in the void phase). The term $w(c_v,\eta)=-A\left(c_v-c_v^o\right)^2\eta(\eta+1)(\eta-1)^2+B(c_v-1)^2\eta^2$ induces the bi-stability in the system. The gradient energy coefficients, κ_v and κ_η, correspond to the surface energy by imposing a penalty due to field inhomogeneity across the diffuse void-matrix interface. The constants *A* and *B* are coefficients of the Landau-terms, and *N* is the number of atoms per unit volume of the material. The system energy defined by Eq. (1) defines two stable phases: a matrix phase (with a minimum at $\eta=0$ and $c_v=c_v^o$) and a void phase (with a minimum at $\eta=1$ and $c_v=1$). The evolution of the vacancy concentration field is obtained using a modified Cahn-Hilliard equation that accounts for vacancies entering the system as a result of collision-cascades:

$$\frac{\partial c_v}{\partial t}=\nabla\cdot M_v\nabla\frac{1}{N}\frac{\delta F}{\delta c_v}+\psi_v\,. \tag{2}$$

The kinetics of the order parameter field are obtained by a phenomenological Allen-Cahn type equation:

$$\frac{\partial\eta}{\partial t}=-L\frac{\delta F}{\delta\eta}\,. \tag{3}$$

In Eqs. (2) and (3), M_v is the mobility of the vacancy defects, *L* is the mobility of the void surface, and ψ_v is a vacancy source rate.

3. Numerical results

A series of simulations were performed to study the void phase evolution on a square 2D periodic domain. The kinetic equations (Eqs. (4) and (5)) are discretized using explicit finite differences in space and forward Euler marching scheme in time. For the numerical results

reported herein, the values $E_v^f = 0.8$ eV and $k_B T = 0.12$ eV are used. This choice corresponds to a temperature of $T \approx 1400K$ and an equilibrium vacancy concentration of $c_v^o \approx 0.001272$. Further, the following values are used for reduced parameters in the our simulations: $\widetilde{M}_v = 1$, $\widetilde{L} = 1$, $\widetilde{\kappa}_\eta = 2\widetilde{\kappa}_v = 2$, $A = B = N$. Figure 1 illustrates the evolution dynamics for a single void for both the case of vacancy supersaturation (S_v) leading to void growth (Fig. 1a and 1b) and the case of vacancy undersaturation leading to void shrinkage (Fig. 1c and 1d).

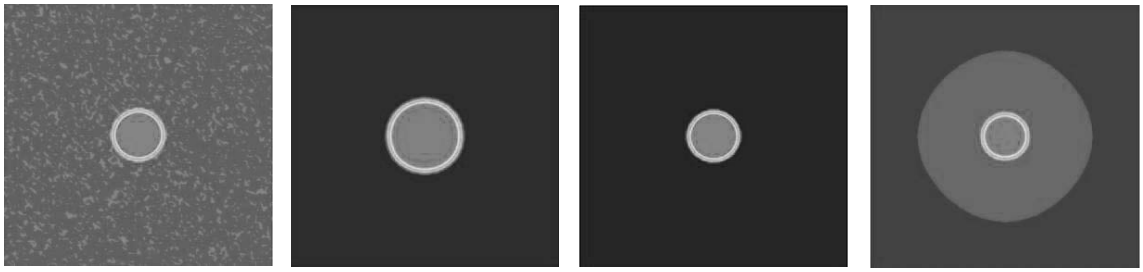

(a) (b) (c) (d)

Figure 1: Void growth and shrinkage dynamics. (a) Void in a matrix of $S_v = 25$ at $\widetilde{t} = 0$, (b)void growth after $\widetilde{t} = 100$, (c) void in an matrix of $S_v = 0.0$, (d) void shrinkage after $\widetilde{t} = 100$.

At higher vacancy supersaturations (shown in Fig. 2), growth of the initial void is accompanied by the nucleation of additional voids, even without a radiation source. It is observed that neighboring voids tend to have a vacancy exchange between them which can cause the growth of larger voids at the expense of the smaller neighbors. Void coalescence is also observed if two voids are very close to one another.

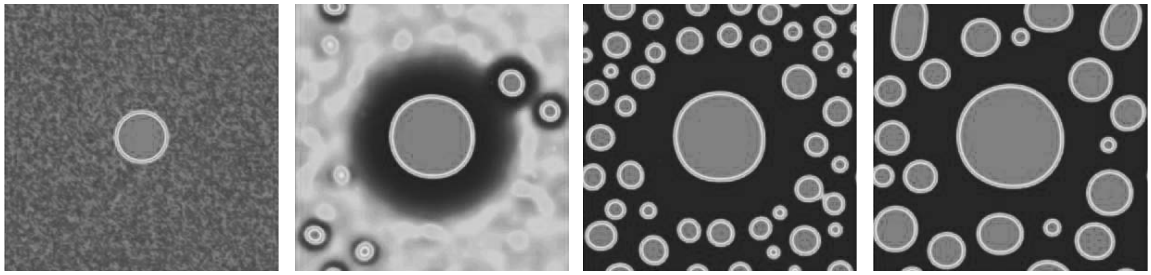

(a) (b) (c) (d)

Figure 2: Concurrent void growth and nucleation in a system containing initial void in a supersaturated matrix ($S_v = 100$), in the absence of radiation induced defect sources. (a) Initial $\widetilde{t} = 0$, (b) $\widetilde{t} = 110$, (c) $\widetilde{t} = 130$, (d) $\widetilde{t} = 500$

Furthermore, a system with vacancy supersaturation in the matrix and source terms due to collision cascade is shown in Fig. 3. These conditions lead to the nucleation of voids and their subsequent growth by vacancy diffusion in the solid and segregation at the void surface.

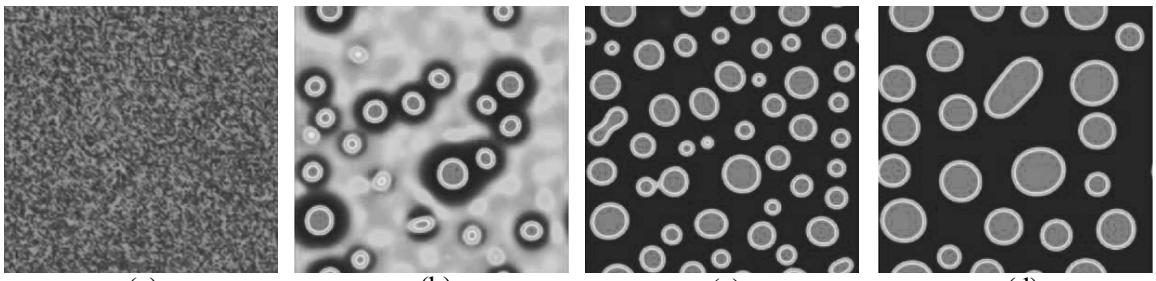

(a) (b) (c) (d)

Figure 3: Void nucleation and growth in a supersaturated system ($S_v = 100$) under the effect of defect source due to radiation damage. (a) Initial $\tilde{t} = 0$, (b) $\tilde{t} = 80$, (c) $\tilde{t} = 100$, (d) $\tilde{t} = 500$

4 . Concluding remarks

A phase field model for tracking void growth dynamics in irradiated materials is presented. Using a unified functional, the free energy of the non-equilibrium system is described in terms of the vacancy concentration field and an order parameter field. The vacancy diffusion in the material is characterized by a modified Cahn-Hilliard equation. We observe that voids grow by vacancy absorption or shrink by vacancy emission, corresponding to the vacancy super- or under-saturation in the matrix. Simultaneous nucleation and growth of voids at higher supersaturations was also demonstrated. Defect sources from collision cascades aid in the nucleation phenomenon. Further aspects of this model, including vacancy-interstitial interactions, thermal fluctuations and stress effects will be reported in future work.

Acknowledgements

The work was supported by DOE/BES funded Computational Materials Science Network (CMSN). Also the support provided by collaborators at Idaho National Laboratory is gratefully acknowledged.

References

[1] J.O. Stiegler and L.K. Mansur, “Radiation effects in structural materials,” Annual Review of Materials Science **9**, 405-454 (1979).
[2] K.C. Russell, “Nucleation of voids in irradiated metals,” Acta Metallurgica **19**, 753-758 (1971).
[3] J. W. Cahn and J. E. Hilliard, “Free energy of a non-uniform system-I. Interfacial free energy,” The Jounral of Chemical Physics **28**, 258-267 (1958)
[4] J. W. Cahn., “On spinodal decomposition,” Acta Metallurgica **9**, 795-801 (1961).
[5] S. M. Allen and J. W. Cahn, “A microscopic theory for antiphase boundary motion and its application to antiphase domain coarsening,” Acta Metallurgica **27**, 1085-1095 (1979).

Phase Field Modeling of Interdiffusion Induced Microstructure Evolution Under Different Driving Forces

Rashmi Ranjan Mohanty[1], Yongho Sohn[2]

[1,2]Advanced Materials Processing and Analysis Center
Department of Mechanical, Materials and Aerospace Engineering
4000 Central Florida Blvd., University of Central Florida, Orlando, Fl-32816

ABSTRACT

Interdiffusion induced microstructure evolution in binary multi-phase alloys was investigated using a phase field model under both isothermal condition and temperature gradient. First, the model was used to simulate microstructure evolution in diffusion couples of Ni-Al alloy system containing γ(fcc) vs. γ+γ′($L1_2$) phases under isothermal condition. Dissolution of the γ′ phase in the two-phase region was well predicted by the model. Second, a new phase field model was devised and employed to investigate the effect of thermotransport or diffusion under a temperature gradient in single-phase and multi-phase alloys of a binary system. Simulation results show that an applied temperature gradient can cause significant redistribution of constituents and phases in the alloy. In multi-phase alloys, the thermomigration effect can cause the formation of single-element rich phases at the cold and hot ends of the alloy.

1. Introduction

Interdiffusion plays an important role in controlling phase transformations and consequent microstructure evolution in multicomponent alloys. During high temperature applications, interdiffusion can significantly alter the microstructure, leading to changes in the physical and mechanical properties of the alloys. Well-known examples, where an understanding of interdiffusion becomes critical, include dissolution of precipitates (e.g., γ matrix and γ' precipitates in Ni-base superalloys), coating-substrate interactions, and nuclear fuel/cladding interactions.

A continuous decrease in length scale and an increase in operating temperatures can produce temperature gradients large enough to influence the diffusion process considerably. It is well known that a temperature gradient can cause a composition gradient to develop in a homogeneous alloy [1]. This phenomenon known as the thermotransport effect, or the Soret effect is gaining importance in many applications, e.g. in superalloy coatings used in gas turbine engines, metallic nuclear fuel alloys, interconnects of electronic circuits, etc. This study is aimed at devising a phase field model to predict the effect of isothermal diffusion and thermotransport on microstructure evolution in binary alloys.

2. Model Description

Two types of driving forces for diffusion have been considered in this model. One is based only on the gradient in chemical composition under isothermal condition, and the second one is due to an applied temperature gradient, which can produce a gradient in composition in the alloy. The model description has been formulated to appropriately represent these two driving forces under the prevailing conditions.

2.1. Isothermal Condition

In phase field model, a binary isothermal system with two phases, which differ in composition and crystal structure, can be described by two field variables: composition (c) and structure-order-parameter (η). With appropriate chemical free energy and interface energy terms, the governing equations for these two field variables can be written as [2]

$$\frac{\partial c(\mathbf{r},t)}{\partial t} = \nabla\left[M_c(c)\nabla\left(\frac{\partial f(c,\eta)}{\partial c} - 2\kappa_c\nabla^2 c\right)\right] \tag{1}$$

and

$$\frac{\partial \eta(\mathbf{r},t)}{\partial t} = -M_\eta\left[\frac{\partial f(c,\eta)}{\partial \eta} - 2\kappa_\eta\nabla^2\eta\right] \tag{2}$$

where, $M_c = c(1-c)\left[c\beta_A + (1-c)\beta_B\right]$ is the chemical mobility, c is the composition in mole fraction, β_A and β_B are the atomic mobility of A and B, respectively, M_η is the kinetic relaxation constant that characterizes the interface mobility, κ_i and κ_η are the gradient energy coefficients associated with gradients of composition and the order parameter, respectively. The chemical free energy density f(c, η) was described by Wang et. al. [3].

2.2. Applied Temperature Gradient

A phase field model was devised to incorporate the thermotransport phenomenon under an applied temperature gradient. The model was applied to a hypothetical binary system whose chemical free energy was approximated by a regular solution model. The governing equation for the composition is

$$\frac{\partial c(x,t)}{\partial t} = \nabla\cdot\left[M_c(c)\nabla\left(\frac{\partial f(c,T)}{\partial c} - 2\kappa_c\nabla^2 c\right) - M_Q\frac{\nabla T}{T}\right] \tag{3}$$

Here, M_c and κ_c have the same meaning as described above, and $M_Q = \rho c(1-c)\left[\beta_A Q_A^{*\prime} - \beta_B Q_B^{*\prime}\right]$ is a combined heat of transport term. $Q_i^{*\prime}$ is the effective heat of transport term, which is a measure of the contribution of the flux of species *i* to the flux of heat [4,5].

The applied temperature field obeys Laplace's equation ($\nabla^2 T = 0$) and boundary conditions, which produces a linear distribution of temperature across the system. The above governing equations were made dimensionless and solved numerically to produce the spatio-temporal evolution of field variables, or in other words, the time evolution of microstructure of the alloys.

3. Results and Discussion

3.1. Isothermal Condition

Interdiffusion microstructures of two γ vs. γ+γ′ diffusion couples in Ni-Cr-Al system with 0.4 and 0.6 volume fractions of γ′ phase are shown in Figs. 1(a) and 1(b). The initial composition profiles or the microstructure of these diffusion couples were prepared by joining single-phase γ alloys with pre-generated two-phase alloys of required volume fractions of γ′ phase in a γ matrix. The evolution of interdiffusion microstructures in these couples were studied by increasing the time of diffusion anneal during simulation.

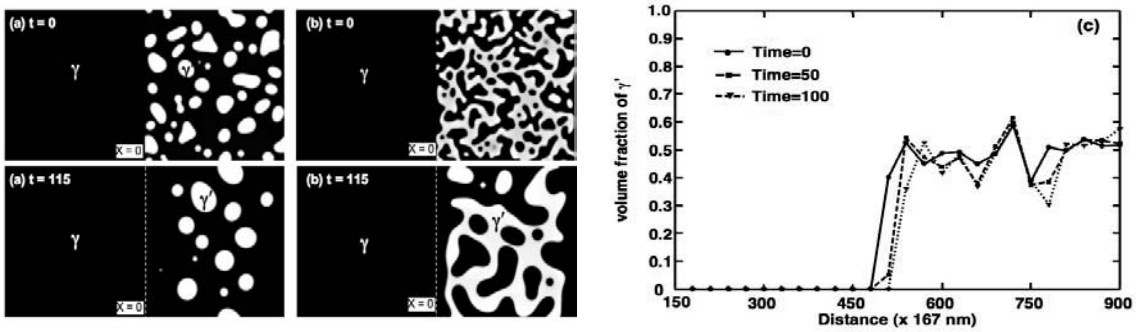

Fig. 1. Interdiffusion microstructures of γ vs. γ+γ′ diffusion couples as a function of time with initial volume fraction of γ′ phase approximately (a) 0.4 and (b) 0.6. (c). Volume fraction profiles of the diffusion couple shown in part (b).

The initial interface between γ and γ+γ′ phase-region is observed to move towards the two-phase region. The volume fraction profile in Fig. 1 (c) shows a decrease in the fraction of γ′ phase near the interface. The γ region grows at the expense of γ+γ′ region by the dissolution of γ′ phase.

3.2. Applied Temperature Gradient

The Soret effect was clearly observed when a temperature gradient was applied to an initially homogeneous single-phase binary alloy. As shown in Fig. 2, a composition gradient developed in the single-phase alloy with preferential movement of atoms towards the hot or cold ends of the alloy.

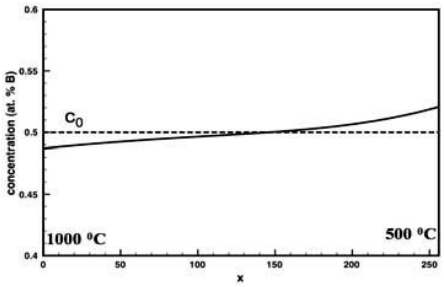

Fig. 2. Composition profile developed in an initially homogeneous single-phase alloy after being subjected to annealing in a temperature gradient.

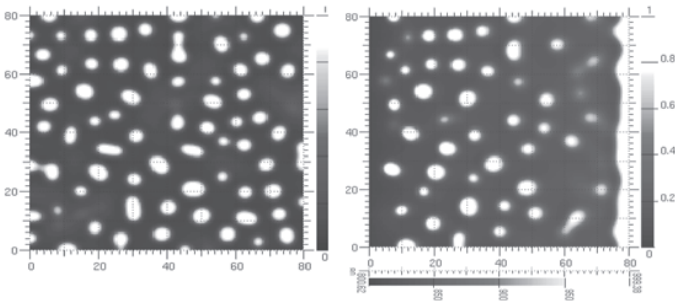

Fig. 3. Two-phase microstructures obtained after annealing (a) isothermally and (b) under a temperature gradient. The bright and dark phases are the B and A rich phases, respectively.

The composition or phase redistribution was also observed in two-phase alloys when a temperature gradient was applied. Microstructures shown in Figs. 3(a) and 3(b) are obtained from the same initial microstructure, but they were annealed isothermally and under a temperature gradient, respectively. It can be seen that no phase redistribution occurred during the isothermal annealing, whereas a considerable redistribution of second phase occurs along with the formation of A and B rich single-phase layers at the hot and cold ends, respectively.

4. Summary

The present phase field model successfully describes the interdiffusion induced microstructure evolution in binary alloys under isothermal annealing and under temperature gradient. Simulation results demonstrated that the dissolution of γ′ phase occurs in γ vs. γ+γ′ diffusion couples with the movement of the initial interface towards the two-phase region. When a temperature gradient was applied, redistribution of both composition and phase occurred in single- and two-phase alloys.

References

[1] A.R. Allnatt and A.V. Chadwick, “thermal Diffusion in Crystalline Solids”, Chem. Rev. 67, 681 (1967).
[2] K. Wu, Y. A. Chang and Y. Wang, “Simulating interdiffusion microstructures in Ni–Al–Cr diffusion couples: a phase field approach coupled with CALPHAD database”, Scripta Mater., 50, 1145, (2004).
[3] Y. Wang, D. Banerjee, C. C. Su and A. G. Khachaturyan, “Field kinetic model and computer simulation of precipitation of $L1_2$ ordered intermetallics from f.c.c. solid solution”, Acta Mater., 46, 2983, (1998).
[4] P. Shewmon, J. Chem. Phys. 29,1032 (1958).
[5] P. Shewmon, Acta Metall. 8, 605 (1960).

Unified Modeling for Microstructure Evolution

K. G. Wang

Physics and Space Sciences Department, Materials Science and Nanotechnology Institute
Florida Institute of Technology, Melbourne, FL 32901
(E-mail: kwang@fit.edu)

ABSTRACT

Microstructural modeling is very important because it can provide a critical link between properties, mesoscopic length scale, and atomistic scale (multiscale modeling). There exist a couple of models and simulations to study microstructural evolution [1]. It will be important and useful to discover unified modeling hidden in microstructure evolution. In this talk, I will derive the unified modeling for microstructure evolution. The governing equations in Lifshitz-Slyozov-Wagner theory and diffusion screening theory [2] that modeled microstructural evolution are derived with some approximations from the unified modeling. The governing equations in multiparticle diffusion simulation and phase-field simulation [3] in microstructure evolution are also derived from the unified modeling. The advantages and limitations for different theories and simulations in microstructure evolution are compared in detail. This comparison can guide scientists to select computational tools for their needs in microstructure evolution. The unified modeling can be applied in many new technological fields, such as self-assembly in nanoscience and pattern formation.

[1] K. G. Wang, and M.E. Glicksman, "Ostwald Ripening in Materials Processing", Chapter 5, *Processing Handbook*, edited by J. Groza et al, CRC Press (2007).
[2] K.G. Wang, M.E. Glicksman, and K. Rajan, "Modeling and Simulation of Phase Coarsening: a Comparison with Experiment", Physical Review E, **69**, 061507 (2004).
[3] L.Q. Chen, "Phase-field Models for Microstructure Evolution", Annual Review Materials Research, **32**, 113 (2002).

Phase field modeling of martensite banding in dual phase steels

Alexandre Viardin[1], **Benoît Appolaire**[1], **Elisabeth Aeby-Gautier**[1], **Mohamed Gouné**[2]

[1] **Nancy Université, LSG2M, École des Mines de Nancy, Parc de Saurupt, 54042 Nancy, France, alexandre.viardin@mines.inpl-nancy.fr**
[2] **Arcelor Research, 57210 Maizières-lès-Metz, France**

ABSTRACT

A comprehensive study of the martensite banding phenomenon in Fe-C-Mn dual phase steels has been undertaken with a 2D phase field model describing the growth of ferrite in austenite, by relating the distribution of martensite to the distribution of remaining austenite at the end of the cooling treatments. After a fine tuning of some parameters to account consistently for paraequilibrium conditions, simulations have been undertaken of the growth of ferrite in complex austenite grain structures. The parameters identified as playing the major role in the build up of the banded structure, i.e. the intensity of Mn segregation and the grain boundary energies, have been investigated.

1 Introduction

After the rolling process of C-Mn steels, microstructural banding may be observed depending on the composition of the alloy, and on the process conditions. This phenomenon can be traced back to the segregation in manganese arising during solidification, which is persistent in spite of subsequent heat treatments. In dual phase steels, these segregated bands are responsible for a banded distribution of martensite, which is detrimental to the mechanical properties. Depending on the temperature of the rolling process, these bands are more or less prominent. Indeed, cold rolling promotes the banding contrary to hot rolling. This is commonly attributed to the difference in austenite (γ) grain size, but the respective role played by nucleation and by growth of ferrite (α) is not completely elucidated yet. For that purpose, we

have thus developed a phase field model for the ferrite growth in γ in C-Mn steels, accounting consistently for both substitutional and interstitial alloying elements.

2 Phase Field Model

Our phase field model is based on the model proposed by Kim et al. [1] (see also [2] for ternary alloys), where the interfacial region is defined as a mixture of α and γ with locally different compositions, but with the same diffusion potential. Thanks to this particular definition, the phase field profile is only weakly coupled to the concentration fields and the asymptotic analysis of the model is greatly simplified.
Contrary to the model of Kim et al., the determination of the phase field mobility does not rely on a perturbation expansion around local equilibrium profiles within the interface, but rather around assumed paraequilibrium conditions. Indeed, preliminary calculations with the mobility proposed in the original model of Kim et al. [1] led to growth rates largely underestimated when compared to experimental measurements. Moreover, it has been observed that the interfacial Mn diffusion speed (which can be seen as the ratio of the diffusion coefficient to the interface thickness D_{Mn}/δ) is a critical parameter to achieve realistic kinetics. A careful calibration of an effective diffusion coefficient for Mn with respect to the interface thickness has thus been undertaken to catch the right kinetics even with large interface width, imposed by computationally tractable discretization of the governing PDEs.
To include the effects of γ/γ grain boundaries on the growth of allotriomorphic α, we have introduced an additional field θ representing the grain orientations, similarly to [3]. To avoid any complications associated with grain boundary movements, the orientation field has been kept constant. The penalizing term proportional to $|\nabla\theta|$ entering the total free energy to mimic the grain boundary energy $\sigma_{\gamma\gamma}$ has been calibrated by performing wetting calculations of ferrite precipitates along grain boundaries. Measuring the static wetting angle and using the Young-Dupré relationship between the interfacial energy, the grain boundary energy and the wetting angle, simply gives $\sigma_{\gamma\gamma}$.
The iron-rich corner of the Fe-C-Mn phase diagram has been simpified by linearizing the limits of the $\alpha + \gamma$ two-phase field, which amounts to consider that α and γ are very dilute regular solid solutions.
Finally, the governing PDEs have been discretized on uniform grids using a finite volume scheme in space, and a first order semi-implicit euler scheme in time. The numerical parameters as well as the time step (10^{-4} s) have been carefully chosen to ensure a good convergence of the iterative numerical scheme. Grids of 500^2 up to 1000^2 volumes have been used to keep the interface thickness below 100 nm so as to

limit as much as possible the spurous effects associated to thick interfaces.

3 Calculations

All the calculations have been undertaken for a steel with 0.07 mass.% C and 1.7 mass.% Mn, similar to grades where martensite banded structure is an industrial issue. In this paper, only isothermal treatments at 700 $^\circ$C are considered.
First, two different γ grain structures system generated with a Voronoi algorithm have been considered in a 20×20 μm^2 system, corresponding to average grain sizes of respectively 12 μm as measured in hot-rolled sheets, and 6 μm as measured in cold-rolled sheets (Figs. 1a and 1c). The grain boundary energies have been set according to the misorientation between adjacent γ grains. In the small grain structure, α nuclei have been distributed at the triple junctions only, whereas in the large grain structure, the same number of nuclei has been distributed both at the triple junctions and along the grain boundaries. The initial Mn field corresponding to the chemical banding has been prescribed by a sine along one direction with a wavelength of 6 μm, as shown in Figs. 1b and 1d.

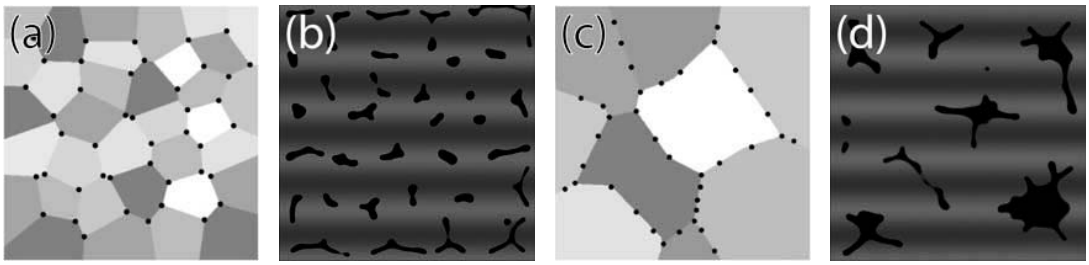

Figure 1: (a) Initial structure with small γ grains (average size of 6 μm); black spots are α nuclei. (b) Final γ distribution (in black) after an isothermal treatment at 700 $^\circ$C during 5 s ; the initial Mn concentration field in γ is superimposed (negatively segregated bands are in dark grey). (c-d) are equivalent to (a-b) for an initial structure with large γ grains (average size of 12 μm).

The final distributions of γ are very different depending on the initial γ grain structure (black regions in Figs. 1b and 1d): for small initial γ grains, it is likely to find martensite banding, whereas for large initial γ grains, martensite islands should be osbserved. These conclusions are in agreement with experimental observations. Two parameters seem to play a major role for explaining the difference between both cases: the grain boundary energies and the intensity of Mn segregation.

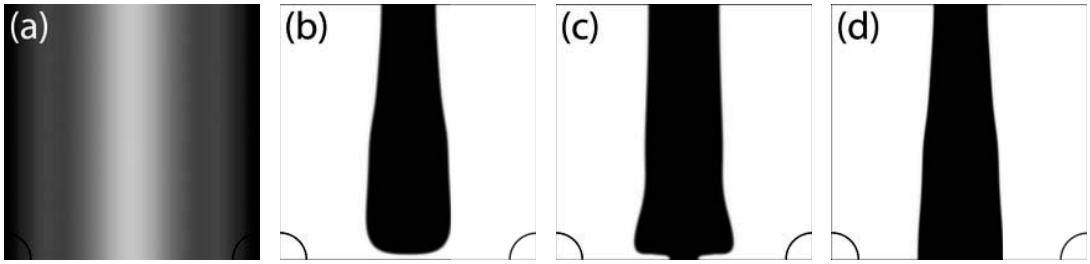

Figure 2: (a) Initial Mn concentration field (wavelength of 5 μm) with an average value of 1.7%. Final ferrite distribution (in white) after an isothermal treatment at 700 $^\circ$C during 3 s with (b) $\Delta c_{\mathrm{Mn}} = 0.8\%$ and $\sigma_{\gamma\gamma} = 0.5$ J/m^2; (c) $\Delta c_{\mathrm{Mn}} = 1.6\%$ and $\sigma_{\gamma\gamma} = 0.5$ J/m^2; (d) $\Delta c_{\mathrm{Mn}} = 0.8\%$ and $\sigma_{\gamma\gamma} = 0$ J/m^2. The initial nuclei at the corners have been superimposed.

In order to investigate in what respect the grain boundaries can break the banded structure by allowing α precipitates to cross the positively segregated bands, a series of calculations has been performed in a 5×5 μm^2 system with only one grain boundary at its bottom side. The Mn segregated bands have been set perpendicular to the grain boundary, and two α nuclei put at the bottom corners aside from the positive band along the grain boundary (Fig. 2).
Three cases are reported in Figs. 2b-d. For a moderate segregation ($\Delta c_{\mathrm{Mn}} = 0.8\%$) and $\sigma_{\gamma\gamma} = 0.5$ J/m^2 (Figs. 2b) α precipitates have grown in the negative bands, but have wetted entirely the grain boundary to bridge both ferrite bands. In Fig. 2c, the segregation is twice that in the previous case: the positive band then prevents the complete wetting of the grain boundary. In the third case (Fig. 2d), the segregation is kept at $\Delta c_{\mathrm{Mn}} = 0.8\%$, but the grain boundary has been suppressed: α precipitates are confined to the negative bands.

References

[1] W.T. Kim, S.G. Kim and T. Suzuki, "Phase-field model for binary alloys", Phys. Rev. E, **60**, 7186 (1999).

[2] M. Ode, W.T. Kim, S.G. Kim and T. Suzuki, "Phase-field model for solidification of ternary alloys", ISIJ Int., **40**, 870 (2000).

[3] J. Warren, R. Kobayashi and W. Craig Carter, "Modeling grain boundaries using a phase-field technique", J. Cryst. Growth, **211**, 18 (2000).

Atomistic Simulation of Nucleation for Multiscale Modeling of Solidification

Ramanarayan Hariharaputran and David T Wu

Institute of High Performance Computing, ASTAR, Singapore
(E-mail: hariharaputran@ihpc.a-star.edu.sg)

ABSTRACT

Solidification plays an important role in industrial processes such as crystal growth from the melt, purification by zone refining, and welding. Hence, it is important to understand the physics of this liquid to solid transformation from a fundamental point of view. Solidification involves nucleation of a crystalline phase from an undercooled, metastable melt. We model solidification using a multiscale approach to bridge atomistic and continuum length/time scales. Parameters such as the nucleation rate and the interfacial energy are difficult to obtain using coarse grained simulations. Insight into these parameters is gained through atomistic simulations using Molecular Dynamics. These parameters are used as input to the coarse grained phase field model to study crystal growth at a larger scale.

Phase-Field Simulation of Microstructure and Void Evolution in Irradiated Materials

Paul C. Millett[1], Tapan Desai[1], Dieter Wolf[1], Srujan Rokkam[2], Anter El-Azab[2]

[1] Materials Sciences Department, Idaho National Laboratory, Idaho Falls, ID 83415, E-mails: paul.millett@inl.gov, tapan.desai@inl.gov, dieter.wolf@inl.gov
[2] Mechanical Engineering Department, Florida State University, Tallahassee, FL 32310, E-mails: srokkam@fsu.edu, anter@scs.fsu.edu

ABSTRACT

The interactive evolution of both polycrystalline microstructure and irradiation-induced defects such as voids and fission gas-filled bubbles in nuclear fuels and structural alloys is complex and critically important to the long-term performance of fission reactors. The excess point defects (i.e., vacancies and self-interstitials) created by on-going displacement cascades either segregate into clusters or annihilate at microstructural sinks including dislocations and grain boundaries. From a simulation standpoint, capturing these complex defect and microstructural evolutions is most feasible at the mesoscale length and time regimes. Here, phase-field modeling is used to simulate grain growth in polycrystalline microstructures containing a distribution of voids that either: (*i*) are initially inserted "by hand" and do not evolve throughout time, and (*ii*) nucleate and grow due to supersaturated vacancy concentrations that evolve according to a Cahn-Hilliard type equation. For the latter case, the phase-field model captures several relevant processes including vacancy fluxes towards sinks (including grain boundaries and void surfaces), void nucleation and growth due to vacancy super-saturation, vacancy annihilation and nucleation at grain boundaries, and finally grain boundary migration (and pinning at voids) resulting in grain growth. Finally, we apply a temperature gradient across the microstructure to determine the overall conductivity of the samples as a function of both grain size and porosity.

This work was supported by the DOE-BES Computational Materials Science Network (CMSN) titled "Multiscale Simulation of Thermo-mechanical Processes in Irradiated Fission-Reactor Materials."

Polarized Dislocation Structures and Directionality of Yield Point in Strain-aged Steels

Vincent Taupin[1], Satya Varadhan[2], Claude Fressemgeas[1], Armand J. Beaudoin[2]

[1]University Paul Verlaine - Metz / CNRS, France
(E-mails : taupin@univ-metz.fr, claude.fressengeas@univ-metz.fr)
[2]University of Illinois at Urbana Champaign, Illinois, USA
(E-mail: varadhan@uiuc.edu, abeaudoi@uiuc.edu)

ABSTRACT

When a low-carbon steel is deformed plastically, then aged and further strained in the same direction, restoration of a sharp yield point is commonly observed. However, if the sample is strained in the direction opposite to that before aging, the sharp yield point phenomenon is usually absent and a Baushinger effect occurs [1]. Such directionality of the yield point phenomenon is of considerable practical importance. It may be useful, as it curbs the return of the yield point in temper-rolled or bake-hardened steels, but it may also limit the benefits of strain aging as a strengthening mechanism. Further, it demonstrates that the strain aging and unpinning mechanisms are dependent upon gradients in the distribution of dislocations, which challenges local interpretations. In the present work, this phenomenon receives interpretation within the framework of a field dislocation theory naturally involving internal length scales through lattice incompatibility and dislocation transport [2]. The model couples the evolution of statistical and polar dislocation densities with that of point defects due to strain-aging [3]. Polar dislocation density reflects incompatible lattice distortion and long-range internal stresses. By assisting yielding in reverse straining, internal stresses are seen as the origin of the Baushinger effect. By promoting dislocation unlocking, they are also found responsible for the absence of yield point in reverse straining. Polarized dislocation structures formed in forward straining in association with internal stress build up may annihilate and inverse polarization in reverse straining. This microstructure evolution is shown to translate into an inflexion of strain hardening after strain path reversal, in agreement with experimental data [4].

[1] R.A. Elliott, E. Orowan, T. Udoguchi, A.S. Argon, Mech. Mat., **36**, 1143 (2004). [2] A. Acharya, J. Mech. Phys. Sol., **49**, 761 (2001).
[3] V. Taupin, S. Varadhan, C. Fressengeas and A.J. Beaudoin, Acta Mater. in press (2008).
[4] T. Hasegawa, T. Yakou and S. Karashima, Mat. Sci. Engng., **20**, 267 (1975).

Modeling Silicon in Demanding Conditions by a New MEAM Potential

Maria Timonova and Barend Thijsse

**Delft University of Technology, Department of Materials Science and Engineering,
Mekelweg 2, 2628 CD Delft, The Netherlands,
(E-mails: m.timonova@tudelft.nl, b.j.thijsse@tudelft.nl)**

ABSTRACT

A recent, new parametrization of Modified Embedded Atom Method potential for Si has been used in molecular dynamics simulations to analyze the results of 500 eV Ar beam sputtering of a Si surface: the amorphous phase, its recrystallization kinetics, and the role of Ar built in during sputtering. To fully test the potential, all these conditions are far from equilibrium. It is found that the structure of the amorphous phase is in reasonable agreement with experiment. Recrystallization obeys the Activation Energy Spectrum model at relatively low temperatures, but the kinetics change towards higher *T*. In the crystallization process, built-in Ar stimulates Si to move over large distances (~12 Å), but, because of the lattice distortions due to the atomic size mismatch, Ar has a net slowing down effect on the crystallization.

1. Introduction

The Modified Embedded Atom Method potential (MEAM), proposed by Baskes in the early nineties [1], allows a systematic and detailed control over angular interaction terms in the atomic forces and thus is a prime candidate for modeling silicon. In fact, it can be shown that by proper choices of its parameters, the MEAM potential can be made to fit the well-known Stillinger-Weber, Tersoff, and EDIP potentials to a high degree of accuracy. This shows that the MEAM potential is more versatile than any of these three and therefore that it promises to be able to model silicon in a superior way. This short communication aims to explore this.

The original Baskes parametrization for Si is not the best one available. We use a recently published MEAM potential for Si [2] that was parametrized by Lee (we will call it MEAM-L) to yield a good description of various *ab initio* energy calculations and selected experimental data. This potential was tested by us in molecular dynamics simulations of 500 eV Ar ion-beam sputtering [2]. It is found that the steady-state sputter yield 1.70 is very close to the experimental value 1.63 [3]. This is a demanding test, which shows that the MEAM-L potential acts properly also under such conditions far from equilibrium. As an interesting side product, this sputtering simulation has produced an amorphous Si phase in natural registry with its crystalline counterpart, i.e. without artificial human construction rules. In this note we analyze the amorphous phase, its recrystallization kinetics at high temperatures, and the role of argon built in during sputtering. Concurrently, the performance of the MEAM-L potential is further put to the test.

2. Properties of the MEAM-L potential

The MEAM-L potential fits *ab initio* energy calculations better than many other potentials [2], and excellently reproduces elastic constants, thermal expansion coefficient, vacancy and

surface formation energies of the diamond cubic phase, as well as the cohesion energies of the Si_2 dimer and the relatively low coordinated simple cubic and beta-tin phases [2]. A property that we found to be quite poorly reproduced is the melting temperature (T_m = 2950 K), which is 75% higher than the experimental value (1683 K). Here we assume that the thermal energy scale of the simulations is correct near and below room temperature, and that elevated temperatures can be expressed relative to the melting point rather than as absolute values. Obviously this matter needs further study. All structural results presented here were obtained after rapidly quenching the systems to 0 K, in order to prevent spurious structural effects due to thermal atomic vibrations.

3. Amorphous phase after sputtering

Experimental high-resolution radial distribution functions (RDF) of Si amorphized by MeV self-implantation [4] show that amorphous Si is 1.8% less dense than the crystal phase and that the coordination number is lower: 3.8. Here we compare the amorphous phase produced by the MEAM-L potential with this experiment. The simulated system, see Fig. 1a, has 4 monolayers removed from a Si surface by 1.5×10^{15} cm^{-2} Ar ions of 500 eV energy, incident at 45° on a 80 Å high Si (001) crystal. The concentration of Ar retained in the system is 0.8 % overall, but only 0.2 % in the crystalline part; these Ar atoms form point defects around themselves: vacancies and Si self-interstitials. To quantify defect concentrations in amorphous and crystal phases alike, we introduce "quasi-vacancies" (QV): an atom i, at position $\mathbf{r}_i$, is said to have an associated QV if the vector $\Delta\mathbf{R}_i \equiv \Sigma_j(\mathbf{r}_j - \mathbf{r}_i)$, with atoms j the neighbors of i, is at least 1.9 Å long. The QV is considered located at $\mathbf{r}_{qv} = \mathbf{r}_i - \Delta\mathbf{R}_i$. QV concentrations thus computed are then divided by the local coordination numbers of the atoms i, in order to give them values that in a crystalline phase exactly match true vacancy concentrations.

Figs. 1a,b show that the amorphous phase is produced in the region above z = 50 Å. It is not significantly denser or less dense than the crystal phase: the normalized density fluctuates around 1. The Si coordination number up to r = 2.83 Å, the first minimum in the RDF (Fig. 1c), is 4.6, which is 0.8 more than in the experiment. The QV density in the amorphous phase has a flat maximum of about 18 %. The Ar concentration peaks at 4%. The amorphous/crystal interface fluctuates within 10 Å around the mean value z = 50 Å.

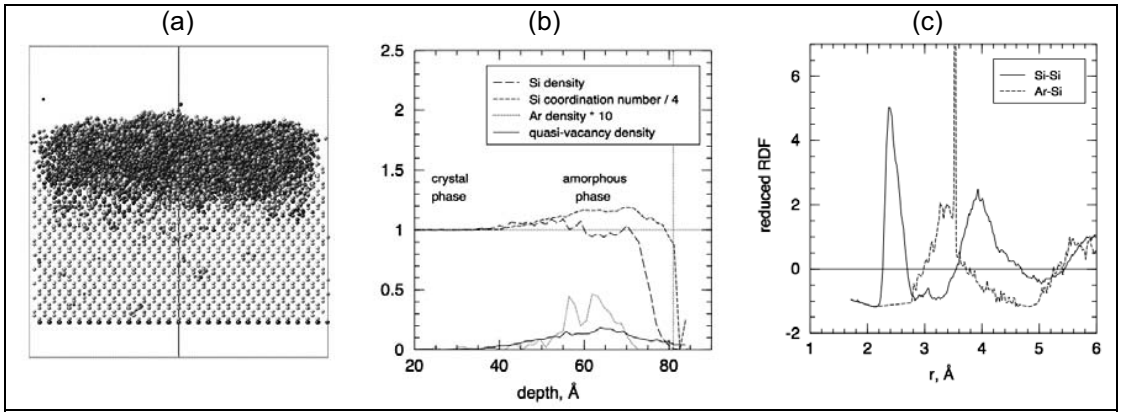

Fig. 1 (a) Simulated Si (001) crystal after ion-beam amorphization and sputter removal of 4 monolayers (<110> view). Atom color indicates coordination number. (b) Profiles of normalized Si, Ar and QV densities and normalized Si coordination number, taken along the vertical (z) direction in picture (a). The vertical line indicates the level of the initial (001) surface, which was dimer-row reconstructed. (c) Reduced RDFs of Si-Si and Ar-Si in the amorphous phase (z > 50 Å) of the system shown in (a).

The RDF for Si-Si in the amorphous phase, Fig. 1c, shows first and second neighbor shells at slightly larger distances (2.37 and 3.95 Å) than found in the experimental RDF (2.35 and 3.80 Å) [4]. For Ar-Si, the broad first neighbor peak in the amorphous phase lies at 3.4 Å. This value is higher than in the crystal phase, where Ar atoms are interstitials (main peaks at 2.47 and 2.83 Å (not shown)), and also higher than 3.05 Å, the value one would expect from the Si and Ar atomic sizes in their respective crystals. The very sharp Ar-Si peak seen at 3.53 Å is caused by the rapid quenching of the simulated system for inspection. All these Ar-Si features are currently not well understood. Angular forces cannot play a troubling role here, because the Ar-Si interaction is modeled by a repulsive Molière pair potential [2].

In summary, the MEAM-L potential produces an amorphous Si phase whose detailed structure deviates slightly from the best experimental RDF data. However, we must keep in mind that the ion energies used for the amorphization in the simulations are four orders lower than in the experiments, and that the room temperature annealing is shorter by at least nine orders.

4. High temperature annealing

The availablility of an amorphous Si phase in natural contact with the crystalline phase is a good starting point for high-temperature recrystallization studies. The system shown in Fig. 1a has been annealed for 8.5 ns at different temperatures T in the range from 0.24 T_m (708 K) to 0.86 T_m (2530 K). The average atomic potential energy U is used as an indicator of the relaxation and crystallization taking place as time evolves. U starts at the value –4.410 eV, the energy per atom in Fig. 1a, and will tend to the value –4.570 eV, the energy of the perfect Si (001) system with dimerized surface. Fig. 2a summarizes the annealing results. U is not shown simply as a function of time but as a function of "time-driven activation energy" Q_t defined as $Q_t = kT \ln(\nu_0 t)$. This choice is inspired by the Activation Energy Spctrum model (AES), according to which relaxation takes place via a large number of initially available relaxation modes of different activation energies. Isothermal annealing at temperature T then produces a time dependence of the relaxing quantity, which – when plotted as a function of Q_t – yields a curve of which the Q_t derivative is equal to minus the initial activation energy spectrum [5]. The value $\nu_0 = 7 \times 10^{11}$ s^{-1} indeed produces perfectly overlapping relaxation curves for the three lowest temperatures, showing that activated events up to at least 1.2 eV (limited by the simulation length) reduce the system energy according to the AES model. At

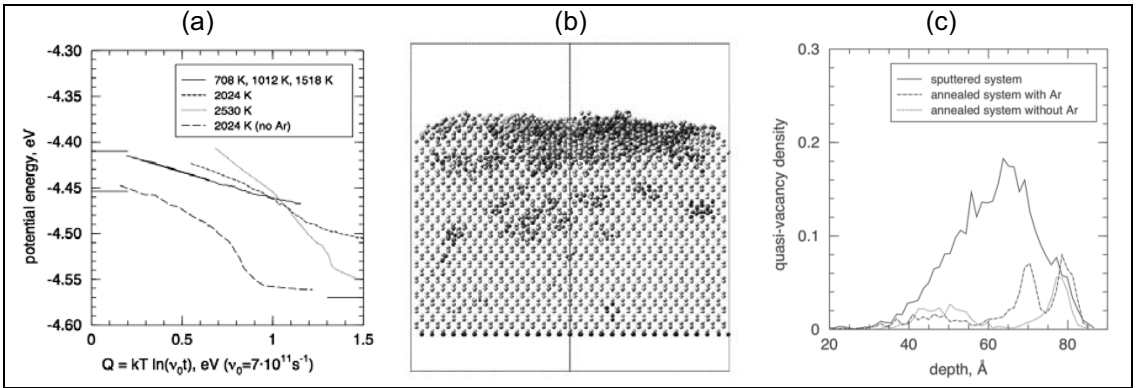

Fig. 2 (a) Average atomic potential energy U during annealing as a function of time-driven activation energy Q_t. Short horizontal lines on the left side are initial potential energies of the system with Ar (higher line) and without Ar (lower line). The short horizontal line on the right side is the potential energy of the completely crystallized structure with dimerized surface. (b) The system with Ar (initially shown in Fig. 1a) after 8.5 ns anneal at 0.69 T_m (2024 K). (c) Normalized QV density profiles, taken along the vertical (z) direction. "Sputtered system" refers to Fig. 1a, "annealed system" to picture (b).

the two higher temperatures, 0.69 T_m (2024 K) and 0.86 T_m (2530 K), the annealing curves no longer obey this relaxation model. The sustained effect of the moving amorphous/crystalline interface during the ongoing crystallization, which constitutes a non-exhaustable supply of activated processes, largely dominates the more subtle AES relaxation effects. Energy changes due to the escape of Ar at these high temperatures have an additional influence: at 0.69 T_m (2024 K), about 12 % of Ar escapes from the system. Fig. 2b shows how far the crystallization has proceeded at the end of the 0.69 T_m (2024 K) anneal. At 0.86 T_m (2530 K) the system has crystallized even more perfectly (not shown), as can be concluded from the final energy value in Fig. 2a.

In order to determine the role of Ar in the process of crystallization, we have artificially removed all Ar atoms from the system of Fig. 1a and allowed it to relax, which significantly decreased U to –4.454 eV. Afterwards the system was annealed at 0.69 T_m (2024 K) just as the system containing the built-in Ar. It is seen (Fig. 2a) that during annealing the potential energy decreases much faster without than with Ar, showing that the presence of Ar slows down the crystallization process. Comparing the annealing with and without Ar in more detail, it is found that in the course of crystallization Ar atoms move up to 15 Å and force Si self-interstitials and vacancies in the crystal phase to annihilate. Si atoms in the amorphous phase move on average up to 5 nearest neighbour distances (12 Å), which is quite considerable. The Ar atoms act as a catalyst for Si atomic motion: in the system without Ar, Si atoms move only half as much. At the same time Ar makes the crystallization process of the amorphous phase more difficult by causing more local lattice distortion. As Fig. 2a shows, the latter effect, retardation of crystallization, is the dominant effect of the built-in Ar.

Quasi-vacancy concentration profiles in the annealed systems with and without Ar are shown in Fig. 2c. It is seen that annealing strongly reduces the concentration of QV defects. The main difference is the QV peak at 70 Å in the system with Ar. This peak is directly associated with Ar atoms which have not yet escaped from the system. Note that the QV peaks at 80 Å are largely an artifact of the definition of a quasi-vacancy. At a surface, however perfect, all atoms generate quasi-vacancies in the empty space above the surface.

5. Conclusions

Amorphous Si produced by 500 eV Ar bombardment of a Si (001) surface was modeled by molecular dynamics simulations using a new MEAM potential. The structural characteristics are in reasonable but not perfect agreement with amorphous Si produced by MeV self-bombardment. Simulation of subsequent crystallization of the amorphous phase at elevated temperatures shows agreement with the AES model up to 0.51 T_m. Built-in Ar atoms significantly slow down crystallization, even though the lattice distortions stimulate Si to move over larger distances in the crystallization process.

References

[1] M.I. Baskes, Phys. Rev. **B 46** (1992) 2727.
[2] M. Timonova, B.-J. Lee and B.J. Thijsse, Nucl. Instr. Meth. **B 225** (2007) 195.
[3] P.C. Zalm, J. Appl. Phys. **54** (1983) 2660; J.G.M. van Berkum and P.C. Zalm, unpublished results (2002).
[4] K. Laaziri, S. Kycia, S. Roorda, M. Chicoine, J.L. Robertson, J. Wang, and S.C. Moss, Phys. Rev. **B 60** (1999) 13520.
[5] T.P.C. Klaver and B.J. Thijsse, Thin Solid Films **413** (2002) 110.

Multi-Phase-Field Study for Pearlite Transformation with Grain Boundary Diffusion

Akinori Yamanaka[1], Takashi Yamamoto[2], Tomohiro Takaki[3], Yoshihiro Tomita[2]

[1]Graduate School of Science and Technology, Kobe University,
1-1, Rokkodai, Nada, Kobe, Hyogo, Japan (E-mail: yamanaka@solid.mech.kobe-u.ac.jp)
[2]Graduate School of Engineering, Kobe University,
1-1, Rokkodai, Nada, Kobe, Hyogo, Japan
[3]Graduate School of Science and Technology, Kyoto Institute of Technology,
Matsugasaki, Sakyo, Kyoto, Japan

ABSTRACT

In order to investigate the effect of grain boundary diffusion (GBD) of carbon on growth velocity of pearlitic microstructure, pearlitic transformation accompanying with the GBD in Fe-C-Mn alloy is simulated by multi-phase-field (MPF) method. The results show that the growth velocity of pearlite decreases with increasing lamellar spacing of pearlite, as suggested by numerical studies using the Zener-Hillert model and experimental studies. And, the present MPF simulation also reveals that the GBD considerably enhances carbon diffusion from ferrite (α) phase to cementite (θ) and assists cooperative growth of α phase and θ. From these results, it can be mentioned that the rate of the GBD largely governs the growth velocity of pearlite.

1. Introduction

Microstructure in steels consists of α phase, pearlite, bainite and martensite phase. In particular, pearlite exhibits lamellar structure of α phase and θ, and possesses good balance between strength and toughness. Therefore, pearlite is widely used as constituent phase in many steels such as ferrite-pearlite (FP) steel. Recently, authors have developed the integrated simulation model for predicting microstructure formation and mechanical properties of steel using the phase-field (PF) method and the homogenization method [1]. Using this model, the mechanical properties of the FP steel depending on the FP microstructure was clarified. However, in order to predict the mechanical properties of the FP steel precisely, morphology of pearlite is needed to be predicted in the PF simulation. For this issue, Steinbach et al. [2] and Nakajima et al. [3] proposed MPF models for the pearlitic transformation and simulated the formation of pearlitic microstructure based on the volume diffusion-controlled mechanism. However, many studies suggest that the GBD of carbon is an essential phenomenon controlling the pearlitic transformation [4]. Thus, the effects of the GBD should be considered in MPF simulation of the pearlitic transformation. Therefore, in this study, the pearlitic transformation is simulated by the MPF method considering both volume diffusion and the GBD of carbon. Furthermore, the role of the GBD on the growth of pearlite is investigated.

2. Multi-Phase-Field Model

In order to simulate the pearlitic transformation in Fe-C-Mn alloy, the generalized multi-phase-field (GMPF) method proposed by Steinbach et al. [5] is used. In the GMPF method, the system of N grains can be considered. Thus, we use N phase field variables, ϕ_i (i = 1, 2, … , N). ϕ_i describes volume fraction of the i th grain and varies smoothly across an interface from $\phi_i = 1$ in the i th grain to $\phi_i = 0$ in other grains. Hereafter, we consider a $\alpha + \gamma + \theta$ three-grain (phase) system for simple description. By using these phase field variables, the total Gibbs free energy of the system, G, is defined by the Ginzburg-Landau type Gibbs free energy functional,

$$G = \int_V \left\{ \sum_{i=1}^{3} \sum_{k=i+1}^{3} \left(-\frac{a_{ik}^2}{2} \nabla\phi_i \cdot \nabla\phi_k + W_{ik}\phi_i\phi_k \right) + g_e \right\} dV , \tag{1}$$

where a_{ij} and W_{ij} are the gradient coefficient and potential height, respectively. The evolution equation of the phase field variable is derived by assuming that the total free energy decreases monotonically with time.

$$\frac{\partial\phi_i}{\partial t} = -\sum_{j=1}^{n} \frac{2M^{\phi}}{n} \left[\sum_{k=1}^{n} \left\{ \left(W_{ik} - W_{jk}\right)\phi_k + \frac{1}{2}\left(a_{ik}^2 - a_{jk}^2\right)\nabla^2\phi_k \right\} - \frac{8}{\pi}\sqrt{\phi_i\phi_j}\,\Delta G_{ij} \right]. \tag{2}$$

Here, n is the number of phase fields in the arbitrary point and is given by $n = \sum_{i=1}^{3} \xi_i$. ξ_i is a step function, which is expressed as $\xi_i = 1$ in a region $0 < \phi_i < 1$ and $\xi_i = 0$ in other region. The third term on the right-hand side of Eqn. (2) is the phenomenological thermodynamic driving force and ΔG_{ij} is its magnitude. To simulate the carbon diffusion during the pearlite transformation in a multiphase system, the total carbon concentration C is defined as a linear function of the local carbon concentration C_λ^i and the phase-field variables ϕ_i. Therefore, when ϕ_1, ϕ_2 and ϕ_3 correspond to α, γ and θ phases, respectively, the total carbon concentration C is written as $C = \phi_1 C_\alpha^1 + \phi_2 C_\gamma^2 + \phi_3 C_\theta^3$. The evolution equation of the total carbon concentration C is expressed by the sum of diffusion fluxes of carbon, J_i, in individual grains as [6],

$$\frac{\partial C}{\partial t} = \nabla\cdot\left(\phi_1 J_1 + \phi_2 J_2 + \phi_3 J_3\right) = \nabla\cdot\left\{\phi_1 D_\alpha^1 \nabla C_\alpha^1 + \phi_2 D_\gamma^2 \nabla C_\gamma^2 + \phi_3 D_\theta^3 \nabla C_\theta^3\right\}. \tag{3}$$

Here, D_λ^i denotes diffusion coefficient of carbon atoms in the i th grain (λ phase). The local concentration C_λ^i is related to the partition coefficient of carbon atoms k_{jr}. The partition coefficient k_{jr} and the driving force ΔG_{ij} are calculated with a linearized phase diagram [7].

3. Computational Model

The growth of a single pearlite lamellar during isothermal pearlitic transformation in Fe-C-Mn alloy is simulated in two-dimensions. Because the diffusion of manganese atoms is much slower

than that of carbon atoms, it is not considered. In this study, the effects of the lamellar spacing λ and the GBD on the growth of pearlite are investigated. When the effect of λ is studied, we use a rectangular computational domain. The size of computational domain along x direction DX, which corresponds to λ, is changed from 0.24 μm to 0.48 μm. And, when the effect of the GBD is studied, λ is set to be constant at 0.24 μm and a $DX \times DY = 0.24 \times 0.48$ μm^2 rectangular computational domain is used. The initial α phase and θ is set at the bottom of the computational domain. Temperature is set to be constant at $T_0 = 973$ K. The interfacial energy of all interfaces is assumed to be constant at 0.5 J/m^2. The initial carbon concentrations of both α phase and θ are in the equilibrium values. The governing equations, Eqns. (2) and (3), are solved by the finite difference method with periodic boundary condition for x direction and zero Neumann boundary condition for y direction. And, the GBD is described by considering k (k = 1, 2, 3, 4) times larger diffusion coefficient than that of bulk phase in the grain boundary region defined as $0 < \phi_i < 1$.

4. Results and Discussions

Figure 1 shows the evolution of carbon concentration field during the growth of pearlite for different λ. From these results, it can be confirmed that the growth velocity of pearlite V decreases with increasing λ, because the increase of λ promotes long diffusion distance of carbon atom from α phase to θ. This dependency of V upon λ is qualitatively identical with the numerical results obtained by the Zener-Hillert model and experiments [7].

Figure 2 shows the distribution of carbon concentration during the pearlitic transformation accompanying with the GBD. It is found that as the carbon partitioning from α phase into θ becomes fast by the GBD, V increases. In the case of k = 4, V equals to 3.0 μm/s. Furthermore, according to Ridley [8], λ and V satisfies the following relationship: λV^m = constant. Here, m is a constant taking the value of m = 2 ~ 3 in the range of the obtained V. Figure 3 shows the relationship between λ and V obtained by the present MFP simulation. It is clarified that the relationship, λV^m = constant, is also satisfied in the present study and the value of m becomes 1.2 ~ 1.4. Although m is smaller than the conventional values (m = 2 ~ 3), m tends to increase

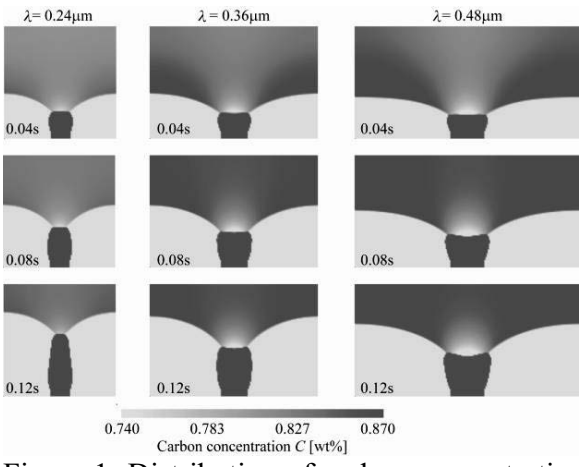

Figure 1. Distribution of carbon concentration during growth of pearlite for different λ.

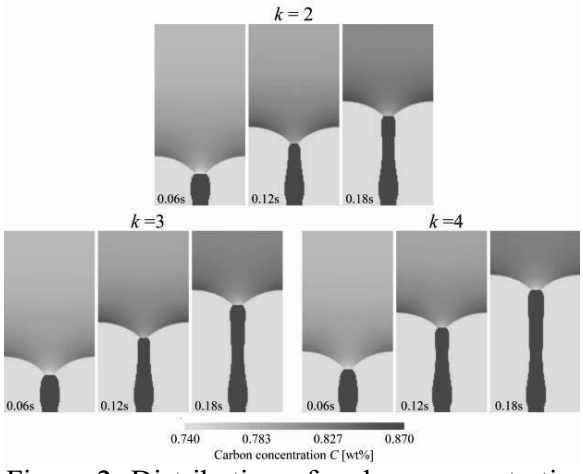

Figure 2. Distribution of carbon concentration during growth of pearlite with GBD.

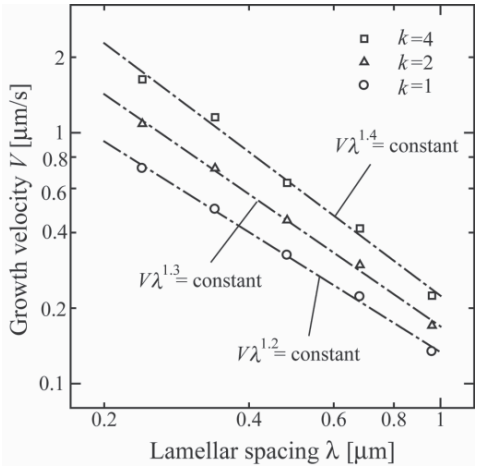

Figure 3. Relationship between lamellar spacing λ and growth velocity of pearlite V.

with increasing the rate of the GBD (the value of k). Therefore, it can be concluded that the growth of pearlite observed in real system can be simulated by considering quite fast GBD.

Acknowledgements

The authors acknowledge the financial support by the Japan Society for the Promotion of Science for Young Scientists and by a Grant-in-Aid for Scientific Research from the Ministry of Education, Culture, Sports, Science and Technology of Japan.

References

[1] A. Yamanaka, T. Takaki and Y. Tomita, "Coupled Simulation of Microstructure Formation and Deformation Behavior of Ferrite-Pearlite Steel by Phase-Field Method and Homogenization Method", Materials Science and Engineering A, **480**, 244-252 (2008).
[2] I. Steinbach and M. Apel, "The Influence of Lattice Strain on Pearlite Formation", Acta Materialia, **55,** 4817-4822 (2007).
[3] K. Nakajima, M. Apel and I. Steinbach, "The Role of Carbon Diffusion in Ferrite on the Kinetics of Cooperative Growth of Pearlite", Acta Materialia, **54**, 3665-3672 (2006).
[4] K. Hashiguchi and J. S. Kirkaldy, "Pearlite Growth by Combined Volume and Phase Boundary Diffusion", Scandinavian Journal of Metallurgy, **13**, 240-248 (1984).
[5] I. Steinbach and F. Pezzolla, "A Generalized Field Method for Multiphase Transformations Using Interface Fields", Physica D, **34**, 385-393 (1999).
[6] J. Tiaden, B. Nestler, H. J. Diepers and I. Steinbach, "The Multiphase-field Model with an Integrated Concept for Modeling Solute Diffusion", Physica D, **115**, 73-86 (1998).
[7] C. Zener, "Kinetics of the Decomposition of Austenite", Transaction of AIME, **167**, 550-595 (1947).
[8] N. Ridley, "A Review of the Data on the Interlamellar Spacing of Pearlite", Metallurgical Transactions, **15A**, 1019-1036 (1984).

Texture Evolution & (Partial) Continuity of the Plastic Strain Rate

Justin Mach[1], Armand J. Beaudoin[1], Amit Acharya[2]

[1]Dept. of Mechanical Science & Engineering, University of Illinois at Urbana-Champaign
1206 W. Green St., MC-244, Urbana, IL 61801
[2]Civil and Environmental Engineering, Carnegie Mellon University,
101 Porter Hall, Pittsburgh, PA 15213
(E-mail: abeaudoi@uiuc.edu)

ABSTRACT

A simple way to introduce multiple scale behavior into a computational material model is to use the equations of crystal plasticity in a finite element framework. The kinematics are based upon a usual decomposition of the deformation gradient, $\boldsymbol{F}=\boldsymbol{F}^{e}\boldsymbol{F}^{p}$. The macroscale field variables are solved in the usual manner while the material response is drawn from the single crystal behavior. The material response depends upon the chosen equations for single crystal slip, hardening, and the evolution of the crystallographic orientation. Classical models for the orientation evolution (in a finite element framework) are entirely local. Independent ODEs are solved for the grain orientation at the level of a Gauss point. Recent work in the area of plasticity modeling based on field dislocation mechanics has shown that one should require a certain level of continuity of the constitutive assumptions in a (classical) plasticity model [1,2]. For the crystal plasticity regime, this leads to a nonlocal evolution equation for the crystallographic orientation, which includes grain neighbor interaction because it is inherent in the continuity requirement. Futhermore, in our simulations, we use a two state variable hardening model at the level of the slip plane, in which the second state variable is computed directly from the incompatible part of the inverse of the elastic deformation gradient—a measure of net dislocation density. The deformation gradient is derived from the finite element solution of the boundary value problem (BVP), therefore the hardening is directly linked with the BVP and a length scale is introduced into the model. We show the application of this model to the simulation and prediction of texture.

[1] A. Acharya, „Jump Condition for GND Evolution as a Constraint on Slip Transmission at Grain Boundaries“, Philosophical Magazine, **87**, 1349 (2007).
[2] A. Acharya, A. Beaudoin and R. Miller, „New Perspectives in Plasticity Theory: Dislocation Nucleation, Waves and Partial Continuity of the Plastic Strain Rate“, Mathematics and Mechanics of Solids, 13, 292 (2008).

This work was supported by a gift from Caterpillar.

An Embedded Statistical Method for Coupling Molecular Dynamics and Finite Element Analyses

Erik Saether[1], Vesselin Yamakov[2], Edward Glaessgen[1]

[1]NASA Langley Research Center, Hampton , Virginia, USA
(E-mails: erik.saether-1@nasa.gov, e.h.glaessgen@nasa.gov)
[2]National Institute of Aerospace, Hampton, Virginia 23666, USA
(E-mail: vesselin.i.yamakov@nasa.gov)

ABSTRACT

The coupling of molecular dynamics (MD) simulations with finite element (FE) analyses yields computationally efficient models that link fundamental material processes at the atomistic level with continuum field responses at higher length scales. The theoretical challenge involves developing a seamless connection along an interface between two inherently different simulation frameworks. Various specialized methods have been developed to solve particular classes of problems. Many of these methods link the kinematics of individual MD atoms with FE nodes at their common interface, necessarily requiring that the finite element mesh be refined to atomic resolution. In the present work, a new approach to MD-FE coupling is developed based on a restatement of the standard boundary value problem used to define a coupled domain. The method replaces a direct linkage of individual MD atoms and FE nodes with a statistical averaging of atomistic displacements in local atomic volumes associated with each FE node in an interface region. The returned FE reaction forces are applied as constant traction boundary conditions to the MD system. The FE and MD computational systems are effectively independent and communicate only through an iterative update of their boundary conditions. With the use of a statistical connection to couple the computational schemes that describe the atomistic quantities and the continuum field, the developed approach is referred to as an embedded statistical coupling method (ESCM). ESCM provides an enhanced coupling methodology that is inherently applicable to three-dimensional domains, avoids discretization of the continuum model to atomic scale resolution, and permits arbitrary temperature states to be applied.

A Quasicontinuum for Multilattice Crystals Exhibiting Martensitic Phase Transformations: Cascading Cauchy-Born Kinematics

Ryan Elliott, Slava Sorkin, Ellad Tadmor

University of Minnesota Minneapolis, Minnesota 55455, USA
(E-mails: elliott@aem.umn.edu, phsorkin@aem.umn.edu, tadmor@aem.umn.edu)

ABSTRACT

The quasicontinuum (QC) method is a multiscale method coupling atomistic regions with a surrounding continuum modeled within a nonlinear finite element formulation. The constitutive response in the continuum is obtained by application of Cauchy-Born (CB) kinematics to the underlying lattice and calculation of the energy and necessary gradients using the same interatomic potentials applied in the atomistic region. Application of QC to multilattice crystals is straightforward in principle, however a question arises as to which description of the crystal structure should be used with CB kinematics. Traditionally, CB kinematics has been interpreted as being applied to the simplest periodic structure that reproduces the crystal. However, with this definition the CB rule can ``fail'' since some deformations require an increase in the periodic size of the unit cell. The problem is that the minimum required cell size cannot be known a priori. Detection of such period extensions can be critical in many cases where martensitic phase transformations occur in the material. To address this issue within QC, a phonon stability analysis is performed locally within each finite element in the continuum region at the end of each load step. This analysis detects the onset of period extension and identifies a new minimal lattice description; a methodology referred to as *Cascading Cauchy-Born kinematics*. Applications to one- and $2^{1/2}$-dimensional test problems that highlight the salient features will be presented. In particular, an *Effective Interaction Potential* material model for a prototypical shape memory alloy is used to simulate a complete shape memory cycle. The results capture both temperature- and stress-induced martensitic transformations.

Finite Element Method and Experimental Approaches in Drawing of Hyper-eutectoid Steel

Byung In Jung

Wire Rod Research Group, POSCO, 1 Goedong-dong, Nam-gu, Pohang, Gyeongbuk 790-785, Korea (E-mail: byungin_jung@posco.com)

ABSTRACT

In the hyper-eutectoid steel wires, the wire drawing process affects their mechanical properties and microstructures tremendously. Among the parameters of drawing process, the approach angle of drawing die is one of the most important parameters in the process. It can create microstructural inhomogeneity inside the material, resulting in the loss of strength and the degradation of ductility. The degradation of ductility in drawn steel wires often causes "delamination," the longitudinal fracture during stranding wires for tire cords or bridge cables. The optimized wire drawing conditions effectively increased the attainable tensile strength and minimized the occurrence of delamination. The effects of several wire drawing parameters on the mechanical properties and microstructures were investigated by finite element analysis and the simulated results were compared to the wire drawing experiments.

1. Introduction

This work is a part of a product development project, dealing with the development of high strength steel wires for bridge cables. The increased strength of the wires allows a reduction of the cable weight, contributing to the cost reduction of bridge construction. Advances in drawing technology have improved the mechanical properties of steel wires continuously, but as the demanded strength of wires in the market has increased, so has the potential of delamination, which is the longitudinal fracture during stranding wires for bridge cables, due to a degradation of ductility. Commercially attainable tensile strength with acceptable level of ductility is approximately 2000MPa to date for bridge cable wire with a diameter of 5.0mm.

The attainable tensile strength of galvanized wires without delamination would be increased by (1) the use of new alloying design, (2) the optimization of drawing process, (3) the minimization of strength decrease of drawn wires by optimizing galvanizing process, etc.

This study focused on the optimization of drawing process in the development of ultra-high strength steel wires. Approach angle of a drawing die is one of the most important parameters for a drawing process [1]. To estimate the effect of approach angle on other parameters, such as pass schedule, friction coefficient, etc. in drawing process, finite element method has been applied. Experiments also have been performed in order to verify the FEM results.

2. Experimental Procedures

The materials used were rods of 13mm diameter of Fe-0.96C-1.0Si-0.6Mn (wt.%) rolled in a wire rod factory in POSCO, Korea. The rods were then drawn using several combinations of different pass schedule and the approach angles of 8, 12, and 16 degrees. The changes of mechanical properties of drawn wires by continuous drawing were evaluated by torsion and tensile tests after each drawing. The microstructural variation was investigated by scanning electron microscope and transmission electron microscope. Finite element analysis of a drawing process has been carried out by Deform3D software using an elasto-plastic approach. A stress-strain curve of the material has been obtained from compression tests under two different strain rate conditions. The workpiece consists of 10000 tetrahedral elements in quarter sectioned cylinder for a length of 10mm. The die used in the simulations were assumed to be rigid. Due to axisymmetry along the longitudinal midplane only quarter of the billet was analyzed. The initial mesh size was determined by running a series of simulations with increasing mesh refinement, using between 10,000 and 100,000 elements. The workpiece was set to 30,000 tetrahedral elements in quarter sectioned cylinder for a length of 10mm, which was found to be sufficient to show local deformation of the sample. The actual numbers of elements automatically assigned were 25,806 tetrahedral elements and 5,843 nodes. The remeshing was done automatically based on a criterion of 0.3 relative interference depth. The friction coefficient used in the simulation was obtained by comparing the load predictions of FEM simulations with varying friction coefficients to the load required for actual drawing.

3. Results

The results presented are about the effect of approaching angle of drawing dies on the properties of cold-drawn hyper-eutectoid steel wires, that is, a part of the optimization of drawing process.
Pearlitic microstructures are highly deformable under wire drawing conditions [2]. As strain increases, cementite lamellar in a favorable position in relation to the drawing axis tended to align itself parallel to the longitudinal wire axis, whereas those in a relatively unfavorable position to the axis deformed plastically or fractured in a brittle manner [3]. It was shown that approach angle affected the strain distribution severely. As the angle increases, strain in a surface region increased whereas strain below about 10% of a diameter of wire changed little, resulting in increased inhomogeneity of strain distribution. This predicted result was validated in microstructural observations of actually drawn wire. In a drawn wire with higher apporach angle, fragmented or severely distorted cementite lamellar structures were observed more frequently than in a lower angle die, resulting in poorer torsion properties, that is, lower attainable tensile strength of bridge cable wire.

References

[1] L. Godecki, “Influence of the Schedule and Die Angle on Properties of Steel Spring Wire”, Wire Industry, **39**, 518-521 (1972).
[2] M. Umemoto, Y. Todaka, and K. Tsuchiya, “Mechanical Properties of Cementite and Fabrication of Artificial Pearlite”, Materials Science Forum, **426-432**, 859-864 (2003).
[3] J. Toribio and E. Ovejero, “Effect of Cumulative Cold Drawing on the Pearlite Interlamellar Spacing in Eutectoid Steel”, Scripta Materialia, **39**, 323-328 (1998)

Breakdown of Self-Similar Hardening Behavior in Au Nanopillar Microplasticity

Jaime Marian, Jaroslaw Knap

Lawrence Livermore National Laboratory, Livermore, California 94550, USA
(E-mail: marian1@llnl.gov)

ABSTRACT

In this work we study of scale effects in Au nanopillars under compression. We propose that plastic yielding in these nanostructures is characterized by a critical lengthscale at which a transition from volumetric to surface dominated plasticity takes place. This transition effectively sets a lower-bound on the self-similar behavior commonly assumed in nanostrength models. Using Quasicontinuum simulations we study the subcritical regime and find that plasticity at these scales is governed by dislocation emission at surface irregularities.

Texture Evolution: New Perspectives

Maria Emelianenko[1], Dmitry Golovaty[2], David Kinderlehrer[3]

[1]George Mason University, Fairfax, VA 22030, USA (E-mail: memelian@gmu.edu)
[2]University of Akron, Ohio, USA (E-mail: dmitry@math.uakron.edu)
[3]Carnegie Mellon University, Pittsburg, PA, USA
(E-mail: davidk@andrew.cmu.edu)

ABSTRACT

Facet interchange and grain deletion, coarsening induced variations in topology, introduce network level changes in the system which are stochastic in nature. Understanding these effects is crucial to the development of a complete theory of grain growth and is the focus of our investigations. We outline several recently developed theoretical approaches aimed at obtaining a mesoscopic description of texture evolution in polycrystalline materials and summarize their advantages and difficulties. Key observations, such as time and space correlations, as well as the resulting master equations and steady-state solutions, are discussed, with theoretical predictions further compared to the results obtained via large-scale simulations and experiments. Newly discovered features of the dynamics underlying microstructure evolution have implications for a wide class of materials science applications.

Kinetic Monte Carlo Simulation Study of The Evolution of Surface Structures During Sub-monolayer Thin Film Growth of Ge on Clean and Patterned Si(001) Substrates

Avinash M. Dongare[1] and Leonid V. Zhigilei[2]

1- Department of Materials Science and Engineering, North Carolina State University, Raleigh, NC (E-mail: amdongare@ncsu.edu)

2-Department of Materials Science and Engineering, University of Virginia, Charlottesville, VA

ABSTRACT

Patterning of semiconductor surfaces is one of the most promising techniques that is being explored for guided nucleation and growth of nano-scale islands during thin film deposition. While the effect of substrate patterning on surface diffusion and self assembly of growing islands is a very complex one at the atomic scale, the fundamental processes responsible for the creation of preferred sites for nucleation of two-dimensional (2D) islands during the initial (sub-monolayer) stages of the deposition can be identified in atomic-level computer modeling. We present a new kinetic Monte Carlo (kMC) model that enables us to study the evolution of surface structures during the deposition of Si/Ge adatoms on a Si(001) substrate at time scales comparable to the experimental ones.

Molecular dynamics (MD) simulations are used to investigate the relation between the surface structure and the corresponding changes in the anisotropic diffusion barriers for Si/Ge adatoms. The MD simulations are preformed for a set of representative surfaces that incorporate strain and chemical modification (intermixed Au-Si surface region). The diffusion pathways and activation energy barriers for Ge adatoms on these model surfaces are obtained from MD simulations and used for parameterization of the kMC model. The effect of the chemical and strain-patterning on the nucleation and growth of 2D Ge islands during the initial (sub-monolayer) stage of the heteroepitaxial thin film growth is investigated in kMC simulations. The results of kMC simulations suggest that chemical patterning can be used to localize the nucleation of 2D Ge islands during sub-monolayer growth. The modification of surface strain (strain patterning), on the other hand, is found to have a negligible effect on the nucleation density of 2D Ge islands.

This work is funded by the National Science Foundation through the Materials Research Science and Engineering Center for Nanoscopic Materials Design at the University of Virginia.

Many Body Atomic Interaction for Uranium

María I. Pascuet[1,2], Julián R. Fernández[1,3,4] and Ana M. Monti[3,4]

[1]Consejo Nacional de Investigaciones Científicas y Tecnológicas, Avda. Rivadavia 1917, C1033AAJ, Buenos Aires, Argentina (E-mail: julrfern@cnea.gov.ar)
[2]Ciclo Básico Común, Univ. de Buenos Aires, Av. Cantilo S/N, Buenos Aires, Argentina;
[3]Depto. de Materiales, Comisión Nacional de Energía Atómica, Av. General Paz 1499, B1650KNA, San Martín, Buenos Aires, Argentina
[4]Instituto Sabato, Univ. Nac. de San Martín / CNEA, Av. General Paz 1499, B1650KNA, San Martin, Buenos Aires, Argentina.

ABSTRACT

Uranium metal transforms allotropically from α (orthorhombic, T<940K) to β (tetragonal, 940K<T<1045K) and then to γ phase (bcc, 1045K<T<1405K). In the present work, an EAM model potential is developed for this pure metal. The potential reproduces the stability of the α phase at low temperatures and a transformation to the γ phase at higher temperatures. Elastic properties, thermal expansion and selfdiffusion by vacancy mechanism are also studied and results compared with available experimental data.

1. Introduction

Uranium suffers different allotropic transformations as temperature increases. The low temperature phase α (*struckturbericht* A20) is stable at T<940K. It consists of a face centered orthorhombic structure with two atoms per primitive cell at atomic positions $(\pm y,\mp y,\mp 1/4)$, expressed in units of the lattice vectors (a/2,–b/2,0), (a/2,b/2,0) and (0,0,c), see Figure 1.

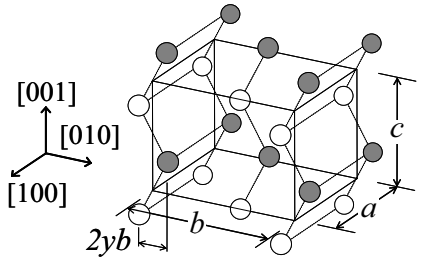

Figure 1. Orthorhombic unit cell and lattice parameters in αU.

At intermediate temperatures (940K<T<1045K) β phase occurs, which has a quite complex tetragonal structure. Finally, the bcc γ phase is stable up to the melting point (T_m=1405K). In this work, an interatomic potential of the EAM type is developed for pure U. In the EAM framework, the total energy of a one component system is

$$E = \frac{1}{2}\sum_{i\neq j} V(r_{ij}) + \sum_i F(\rho_i) \tag{1}$$

where $V(r_{ij})$ is the pair energy between atoms i and j at distance r_{ij}, and $F(\rho_i)$ is the embedding function of atom i in an environment of electronic density $\rho_i = \Sigma_{i\neq j}\phi(r_{ij})$ where $\phi(r_{ij})$ is the contribution of the rigid electronic density of atom j to site i. In this case, ϕ is taken as the Thomas-Fermi screening function, $\phi(r)\sim\exp(-\beta r/a_0)$, being a_0 the equilibrium value of lattice parameter a in αU and $\beta\sim 5$. The pair potential is given as m cubic splines of the form

$$V(r) = \sum_{k=1}^{m} A_k (R_k - r)^3 H(R_k - r) \tag{2}$$

where $H(r)$ is the Heaviside function, R_k the knot points and A_k the fitting parameters. The embedding function is obtained from eq. (1) and Rose et al. equation [1]

$$E(r) = -E_c(1+\tilde{a})e^{-\tilde{a}};\ \tilde{a} = 3\sqrt{\frac{\Omega B}{E_c}}(r/a_0 - 1) \tag{3}$$

where Ω is the equilibrium atomic volume, B the bulk modulus and E_c the cohesion energy. This allows $F(\rho)$ to be tabulated to perform the energy calculations. Equilibrium conditions (null forces and stresses on each atom) and an estimated vacancy formation energy of ~1.4eV for αU constitute the set of conditions to be imposed to fit the parameters. The obtained equations are solved under the assumption that $r_1=r_2$ and $r_3=r_4$, being r_i the i-th neighbour distance. Such restrictions impose the following relationship between lattice parameters

$$\frac{b}{a} = \frac{1}{\sqrt{2y}};\quad \frac{c}{a} = 2\sqrt{1-2y} \tag{4}$$

The lattice stability of the αU against simple hexagonal, hcp, bcc and fcc was imposed. Table 1 shows the quantities used in the fitting and Table 2 the fitted values of R_k and A_k.

Table 1. Fitted, experimental (exp.) and first principles (FP) values for αU [2,3].

	Fitted	exp.	FP
a (Å)	2.7745	2.836	2.845
b (Å)	6.0718	5.866	5.818
c (Å)	4.9358	4.935	4.996
y	0.1044	0.1017	0.1025
Ω (Å^3)	20.79	20.52	20.67
E_c (eV)	5.773	---	5.773
B (eV/Å^3)	0.83	0.846	0.83

Table 2. Fitted values of R_k (in Å) and A_k (in eV/Å^3)

R_1	4.50	A_1	-2.6217703
R_2	4.35	A_2	5.5043693
R_3	4.20	A_3	-2.8225308

2. Property calculations

Nine elastic constants are necessary to describe the elastic behaviour of the orthorhombic αU. As the present potential reproduces correctly only volume changes, it is useful to study its behaviour under more general deformations. To calculate each of the elastic constants C_{ij}, the αU structure is homogeneously distorted in small amounts and, due to its internal degree of freedom y, further relaxed to obtain an energy vs strain plot. The C_{ij} values are extracted from the second derivative of such plots (Table 3). Although there are some important differences, it is seen that C_{ij} involving normal stresses are larger than those corresponding to shear stresses, as reported in [2].

Table 3. Calculated (EAM), first principles (FP) and experimental values (Exp.) [2] of the elastic constants C_{ij} in αU. All values are expressed in eV/Å^3.

	C_{11}	C_{22}	C_{33}	C_{44}	C_{55}	C_{66}	C_{12}	C_{13}	C_{23}
EAM	1.19	0.88	1.07	0.16	0.14	0.13	0.68	0.81	0.67
FP	1.87	1.37	2.00	0.94	0.58	0.75	0.31	0.03	0.67
Exp.	1.31	1.34	1.85	0.91	0.59	0.54	–	–	–

Standard molecular dynamics (MD) simulations for a relatively small system (N=180 atoms) were performed in the range $0<T<1400$K. Fig 2 shows the atomic volume Ω as a function of temperature. Two discontinuities are observed at around 650K and 1200K corresponding to phase changes, which could be identified as αU(ort)→γU(bcc) and γU(bcc)→U(liquid).

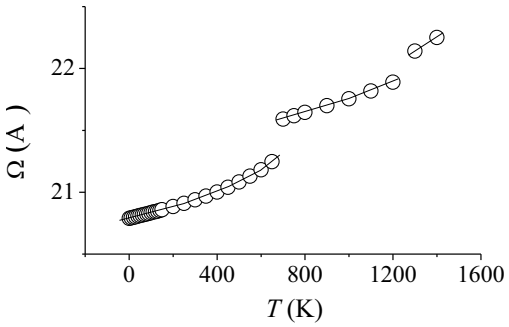

Figure 2. Atomic volume Ω as a function of temperature T.

MD simulations show a linear expansion in the a and c lattice parameters while b contracts with increasing T, which agrees with experimental evidence [4]. Bulk modulus is calculated from its definition $B=-\Omega\partial p/\partial\Omega|_T$, where p is the hydrostatic pressure, and p vs Ω plots obtained from MD at $p\neq0$ and T=const. B decreases with increasing T and $B_{\alpha U}>B_{\gamma U}$, as observed experimentally [5].

Vacancy formation E^f and migration E^m energies have also been studied. Standard molecular statics (MS) simulations (N~4000 atoms), which can be performed only at T=0 on αU, give E^f=1.36eV. MD simulations were used to study E^f at non zero temperatures. Values in the range 1.39–1.50eV ($500\text{K}<T<600\text{K}$) for αU and 1.75eV ($800\text{K}<T<900\text{K}$) for γU were obtained. First principles calculations show that E^f=1.08eV for γU [6]. Self diffusion by vacancy mechanism was calculated from mean square displacements $\langle x^2\rangle$ by using both MD and lattice kinetic Monte Carlo (MC) simulations. The latter method uses vacancy jump values of E^m obtained from

MS, which range from 0.18 (1st neighbors jump) to 0.69eV (4th neighbors jump). MD results show that diffusion is faster in the [100] direction than in the [010] and [001] (see Fig.1), in good agreement with experimental results [7]. MC results show that fast diffusivity occurs also in the [001] direction. Average values of E^m in each direction for both αU and γU were obtained by fitting an Arrhenius behavior, $\langle x^2\rangle/2t \sim \exp(-E^m/kT)$, where t is time. Results are 0.1, 0.3 and 0.4 eV for a, b and c axes, respectively, in αU using MD. The corresponding values for MC are 0.2, 0.3 and 0.2 eV. In γU a value of 0.7 eV was obtained for MD. The sums E^f+E^m are in good agreement with the self diffusion activation energy of 1.78eV reported for αU [8].

3. Conclusions

The obtained EAM potential to model pure U reproduces the stability of the orthorhombic αU at low temperatures and the transformation to bcc γU at high temperatures, as in the real metal. It fits correctly the elastic behaviour under volume changes and only approximately more general deformations. Although differences are obtained between MD and MC, results for diffusion predict that transport is faster in a (and possibly c) axis than in the b, as observed experimentally.

Acknowledgements

This work has been performed under projects PIP 5062 (CONICET) and C047 (UNSAM).

References

[1] J. H. Rose, J. R. Smith, F. Guinea and J. Ferrante, "Universal Features of the Equation of State of Metals", Physical Review B, **29**,2963 (1984).
[2] P. Söderlind, "First-Principles Elastic and Structural Properties of Uranium Metal", Physical Review B, **66**, 085113 (2002).
[3] J. E.Garcés, A. C. Marino and G. Bozzolo, "Atomistic Modeling of the Interdiffusion of Al in the UMo Based Fuel", 24th International Meeting on RERTR, Bariloche, Argentina, 2002.
[4] H. H. Chiswik, A. E. Dwight, L. T. Lloyd, M. V. Nevitt, S. T. Zegler, "Advances in the Physical Metallurgy of Uranium and its Alloys", Proc. of the 2nd United Nation International Conference on the Peaceful Uses of Atomic Energy (United Nations, Geneva, 1958).
[5] P. E. Armstrong, D. T. Eash and J. E. Hockett, "Elastic Moduli of Alpha, Beta and Gamma Polycrystalline Uranium", Journal of Nuclear Materials, **45**, 211 (1972/73).
[6] S. Xiang, H. Huang, L. M. Hsiung, "Quantum Mechanical Calculations of Uranium Phases and Niobium defects in Gamma-Uranium", Journal of Nuclear Materials, **375**, 113 (2008).
[7] R. Resnick and L. L. Seigle, "The self-diffusion of alpha-uranium", Journal of Nuclear Materials, **5**, 5 (1962).
[8] P. Ehrhart, P. Jung, H. Schultz , H. Ullmaier, "Atomic Defects in Metals", ed. H. Ullmaier, Landolt-Börnstein, New Series, Group III, Vol. 25 (Springer-Verlag, Berlin, 1991).

Molecular Dynamics Simulations and Kinetic Models of Fracture under High Strain Rate.

A. Kuksin[1,2], G. Norman[1], V. Pisarev[2], V. Stegailov[1], A. Yanilkin[1,2]

[1]Joint Institute for High Temperatures of RAS, Moscow, Russia;
[2]Moscow Institute of Physics and Technology (State University), Dolgoprudny, Russia
(E-mail: yanilkin@ihed.ras.ru)

ABSTRACT

The verification of models for void nucleation and growth under high strain rates and at the heavily metastable states of liquids and solids is presented. Our analysis is based on data of equilibrium and non-equilibrium MD simulations of LJ substance and aluminum as described by EAM interatomic potential [1]. Void nucleation rates and some substance properties used in the models (such as surface tension) are evaluated independently. It gives a possibility to compare theoretical predictions with direct estimation of nucleation and growth kinetics in the scope of common model systems. Several models are considered: classical nucleation theory [2], viscous void growth kinetics, constitutive relations for prediction of the spall strength [3]. The models are widely used in modern hydrocodes for description of fracture of materials in metastable states. The spall strength obtained from MD simulations and models are compared with experimental data. Also the influence of nanoprecipitates and grain boundaries on fracture kinetics and spall strength is discussed.

[1] X.-Y. Liu, Xu Wei, M.M. Foiles, J.B. Adams, “Atomistic studies of segregation and diffusion in Al-Cu grain boundaries”, Applied Physics Letter, **72**, 1578 (1998).
[2] V.P. Skripov, M. Z. Faisulin, “Phase tranforamtions crystal-liquid-gas and thermodynamic similarity”. Moscow.: Fizmatlit, 160 (2003).
[3] D.E. Grady, “The Spall strength of condensed matter”, Journal of the Mechanics and Physics of Solids, **36**, 353 (1988).

This work was partially supported by the RAS programs 3, 9 and 14.

The Influence of Temperature on Plasticity of Al Alloys: Molecular Dynamics Study

Alexey Yu. Kuksin, Genri E. Norman, Vladimir V. Stegailov, Alexey V. Yanilkin

Joint Institute for High Temperatures of Russian Academy of Sciences – JIHT RAS,
13/2 Izhorskaya Street, Moscow 125412, Russia
(E-mail: kuksin@ihed.ras.ru)

ABSTRACT

A high strain-rate plastic deformation of single crystal Al with precipitates is studied by means of molecular dynamics. The dynamic regime is considered when dislocation velocity is high and limited by a phonon drag. The temperature dependence of the drag coefficient of an edge dislocation is evaluated. The stresses and corresponding delay times required to penetrate precipitates and voids are calculated. The kinetics of the plastic flow activation is determined from a direct simulation of the shock wave loading. Possible interpretation of the experimental data on a dynamic yield stress from the shock wave tests is discussed.

1. Introduction

The molecular dynamic (MD) simulations presented are devoted to study the mechanisms and kinetics of plasticity of Al and its alloys under strain rates ~ 10^5 s^{-1} and more. Under such a high strain rate the value of a dynamic yield stress is not equal to a steady-state one and depends on the strain rate [1,2]. The high strain rate is provided by a sufficient density of mobile dislocations and a high dislocation velocity. This is reflected in a well-known Orowan's equation: $d\varepsilon/dt = \rho_m bv$. Since a dislocation density changes during an intensive loading, kinetics of the nucleation process along with dislocation mobility are two temperature-dependant factors that influence on a variation of a dynamic yield stress with temperature. The kinetic models of the mentioned processes may provide a useful link between atomistic simulations and a dislocation dynamics description of plasticity [3]. Thus we focus our study on: a) the mobility of dislocations in single crystal Al with pores or doped with Cu precipitates; b) the initiation of a plastic flow behind a shock wave front.

2. Mobility of Individual Dislocations

Simulation model for evaluation of the mobility represents single crystal with unit edge dislocation. Periodic boundary conditions are applied along the dislocation line and in the direction of Burgers vector. A detailed discussion of similar models one can find in [4]. An edge dislocation is introduced in the simulation by removing atoms that belong to one (1-10) half

plane and subsequent equilibration of the system. A perfect edge dislocation in a fcc crystal is energetically unstable and dissociates into two partials separated by a stacking fault region. Several atomic layers near the lower and upper boundaries represent a perfect lattice and form two rigid blocks. Shear stress is applied by a shift of the upper block under the action of a preset external force, while the lower block is fixed. Embedded atom method potential [5] for Al-Cu alloys is involved.

Dynamic regime of dislocation motion is studied: the shear stress is high enough (above 10 MPa) for dislocations to overcome Peierls barriers. In this case dislocation velocity is high and limited by an interaction of dislocations with crystal lattice vibrations (phonon drag [1]). The dislocation velocity $v(\sigma)$ in aluminum single crystal evaluated from the MD simulations increases with an applied shear stress σ. It is linearly proportional to σ at relatively small stresses and approaches asymptotically to a terminal value further. The linear part of the dependence is characterized by the drag coefficient B of dislocations: $\sigma b=Bv$. An increase in the temperature T results in decreasing dislocation velocity v. It manifests that dislocation motion in the dynamic regime requires no thermal excitation. The temperature dependence of the drag coefficient B(T) of an edge dissociated dislocation calculated is the increasing function of T and close to linear in all the temperature range but the region near the melting point. The obtained temperature dependence of the phonon drag coefficient agrees at low temperatures with the available experimental data and with the existing theoretical predictions [1].

Critical resolved shear stresses required for dislocation to penetrate nanosize obstacle (precipitates or voids of typical diameter $d = 0.5 – 3$ nm) are calculated. The distance between obstacles L considered in the simulations varies from 10 to 60 nm. The straightening effects of voids and non-coherent precipitates are comparable at 300 K (up to ~ 300 MPa at the mentioned range of d and L). The influence of temperature is stronger in a case of voids and the temperature increase to 800 K result in a drop of the critical stress to a value of several tens of MPa, which is close to the stress in a defect-free single crystal under similar strain-rate. The decrease of the critical resolved stress in systems with precipitates is substantially smaller in magnitude. Inverse temperature dependence can be observed for clusters which size is smaller than dissociation width between partials (approximately 1 nm). A delay time (until the dislocation depinning) increases at elevated temperature in accordance with the growing phonon drag.

3. Activation of Plastic Flow

The onset of a plastic flow is studied by non-equilibrium MD simulation of the shock wave initiated via an impact of a piston and a target. The structure of the shock wave is derived from the direct simulations: distribution of normal and shear stresses, dislocation loops and other defects arising during plastic deformation. The value of the shear stress necessary to initiate plastic flow and the types of defects appeared are determined. While the stacking faults pattern in moderate shock waves is similar to what was obtained for fcc crystals with the Lennard-Jones pair potential [6] dislocation twins are observed at higher piston velocities. The results for several EAM potentials [5,7] for Al are similar except the interatomic potential [8] with the extremely low energy of the stacking fault. Simulations with the latter potential reveal that the critical shear stress for plasticity is much lower.

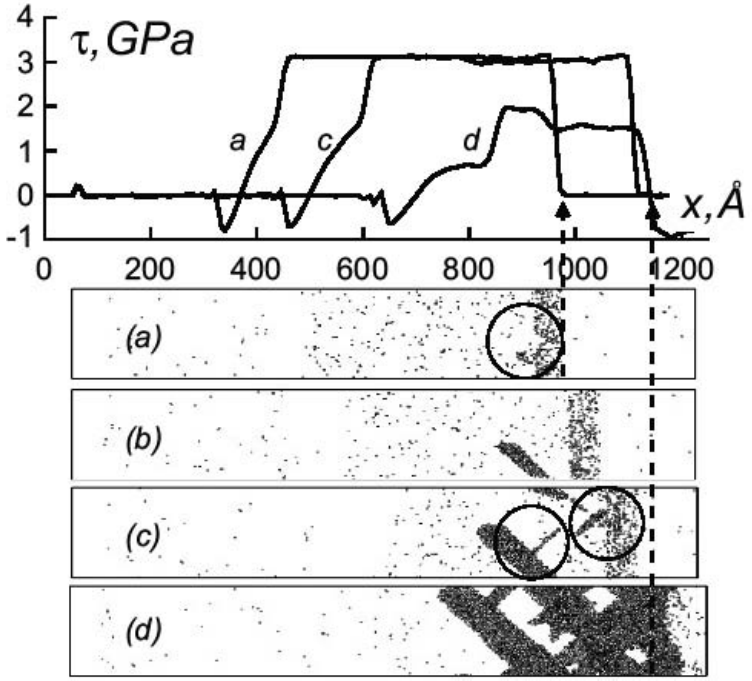

Figure 1. The formation of the stacking faults under shock wave loading. The profiles of a shear stress $\tau = 3/4\ (\sigma_{xx} - p)$ are shown on the top. The snapshots of the system at four moments of time are presented below: (a) 9 ps; (b) 10 ps; (c) 11 ps; (d) 14 ps. Atoms with a local environment corresponding to a perfect fcc structure (according to the value of a central symmetry parameter) are not shown.

A typical shock wave profile obtained with the potential [7] is shown on Fig. 1. The shock wave along [100] was generated in a perfect single crystal 300x50x50 fcc unit cells in size thermalized at 300 K by an impact of a piston (the piston width is 75 unit cells). Under conditions described the piston velocity larger than 1.5 km/s is needed for dislocation loops to appear. The very case is shown on Fig. 1 and it is seen a certain delay before slippage occurs. Indeed, while Fig. 1a corresponds to the moment of 9 ps after the impact, the critical shear stress τ of approximately 3 GPa have been achieved notably earlier. A certain time needed to form stacking faults points out to a fluctuation nature of the onset of slippage. The rate of the subsequent growth of the slipped region is close to the terminal value of dislocation velocity (~ 3 m/s). Since a shock wave front propagation velocity (~ 7 m/s) is relatively higher the shear stress right behind the front remains on the critical value and formation of a new slippage planes takes place (see Fig. 1c). A density of dislocation loops formed and their propagation velocity lead to a timescale of substantial stress relaxation is several tens of ps. A major part of the stacking fault pattern disappears during a subsequent propagation of a release waves. It is seen to the right from the dashed vertical line on Fig. 1d.

The effect of temperature and presence of the precipitates and voids on the activation of the plastic flow is considered. The activation of the stacking faults becomes easier at elevated temperature while the relaxation of shear strain can be slower due to a decrease in dislocation velocity. Hence smaller stress relaxation is observed for several interatomic potentials at the same loading conditions.

4. Discussion

The temperature dependence of the dynamic yield stress of single crystal Al obtained in the shock wave tests [2] is described well by the temperature dependence of the phonon drag coefficient B(T) obtained in the simulations assuming the dislocation density ρ_m to be temperature independent and equal to $\sim 7\times10^8$ cm^{-2}. The difference of one or two orders of magnitude in comparison to the typical density of mobile dislocations in single crystal aluminum under normal conditions (10^6–10^7 cm^{-2}) can be explained by an increase in the dislocation density as a result of material compression in the shock wave. The data on aluminum alloy [2] demonstrates that the dynamic yield stress approaches to the single-crystalline value at elevated temperature. The latter results are in a qualitative agreement with our observations for Al with voids and precipitates.

Acknowledgements

This work was performed at the MFTI-60 cluster of the Moscow Institute of Physics and Technology and supported by the Program for Basic Research of RAS “Investigation of Matter under Extreme Conditions” and the Analytical Program of the Ministry of Education and Science of the Russian Federation “Development of Scientific Potential of Higher Schools 2006–2008”.

References

[1] V.I. Al’shits and V.L. Indenbom, “Dynamic Drag of Dislocations”, Soviet Physicks Uspechi, **115,** 3 (1975).
[2] G.I. Kanel’, V.E. Fortov, S.V. Razorenov, “Shock Waves in Condensed-State Physics”, Soviet Physics Uspechi **50,** 771 (2007).
[3] J.A. Moriarty, V. Vitek, V.V. Bulatov, S. Yip, “Atomistic simulations of dislocations and defects”, Journal of Computer-Aided Materials Design, **9,** 99 (2002).
[4] Yu.N. Osetsky and D.J. Bacon, “An atomic-level model for studying the dynamics of edge dislocations in metals”, Modelling and Simulation in Materials Science and Engineering, **11,** 427 (2003).
[5] X.-Y. Liu, Wei Xu, S.M. Foiles, J.B. Adams, “Atomistic Studies of Segregation and Diffusion in Al-Cu Grain Boundaries”, Applied Physics Letters, **72,** 1578 (1998).
[6] B.L. Holian and P.S. Lomdahl, “Plasticity Induced by Shock Waves in Nonequilibrium Molecular-Dynamics Simulations”, Science, **280,** 2085 (1998).
[7] Y. Mishin, D. Farkas, M.J. Mehl, D.A. Papaconstantopoulos, “Interatomic potentials for monoatomic metals from experimental data and ab initio calculations”, Physical Review B **59,** 3393 (1999).
[8] J. Cai and Y.Y. Ye, “Simple analytical embedded-atom-potential model including a long-range force for fcc metals and their alloys”, Physical Review B, 54, 8398 (1996).

Atomic Ordering in Nano-Layered $L1_0$ AB Binaries: Multiscale Monte-Carlo Simulations

M. Kozlowski[1], R. Kozubski[1], J. Wróbel[2], T. Wejrzanowski[2], K.J. Kurzydłowski[2], Ch. Goyhenex[3], V. Pierron-Bohnes[3], M. Rennhofer[4], S. Malinov[5]

[1]Interdisciplinary Centre for Materials Modelling, M Smoluchowski Institute of Physics, Jagiellonian University, Reymonta 4, 30-059 Krakow, Poland (rafal.kozubski@uj.edu.pl);
[2]Warsaw University of Technology, Faculty of Materials Science and Engineering, Woloska 141, 02-507 Warszawa, Poland (twejrzan@inmat.pw.edu.pl);
[3]IPCMS, 23 rue du Loess, BP 43, F-67034 Strasbourg, France (vero@ipcms.u-strasbg.fr);
[4]Faculty of Physics, University Vienna, Strudlhofg.4, A-1090 Vienna, Austria (marcus.rennhofer@univie.ac.at);
[5]School of Mechanical and Aerospace Engineering, Queen's University Belfast, Stranmills Road, Belfast BT9 5AH, UK (S.Malinov@qub.ac.uk)

ABSTRACT

Combined nano- and mesoscale simulation of chemical ordering kinetics in nano-layered $L1_0$ AB binary intermetallics was performed. In the nano- (atomistic) scale Monte Carlo (MC) technique implemented with vacancy mechanism of atomic migration and diverse models for the system energetics were used. The meso-scale microstructure evolution was, in turn, modelled by means of a Monte Carlo procedure simulating antiphase-domain-boundary (APB) motion as controlled by antiphase-boundary energies evaluated within the nano-scale simulations. The study addressed FePt thin layers considered as a material for ultra-high-density magnetic storage media and revealed metastability of the $L1_0$ *c*-variant superstructure with monoatomic planes parallel to the (001) layer surface and off-plane easy magnetization. The layers, originally perfectly ordered in a *c*-variant of the $L1_0$ superstructure, showed homogeneous disordering running in parallel with a spontaneous re-orientation of the monoatomic planes leading to a mosaic microstructure composed of *a*- and *b*-$L1_0$-variant domains. The domains nucleated heterogeneously on the free surface of the layer and grew discontinuously inward its volume. Finally, the domains relaxed towards an equilibrium microstructure of the system. Two "atomistic-scale" processes: (i) homogeneous disordering and (ii) nucleation of the *a*- and *b*-$L1_0$-variant domains showed characteristic time scales. The same was observed for the meso-scale processes: (i) heterogeneous $L1_0$-variant domain growth and (ii) domain microstructure relaxation. The above complex structural evolution anticipated by the multiscale MC simulations has recently been observed experimentally in epitaxially deposited thin films of FePt.

1. Introduction

FePt, FePd and CoPt: the $L1_0$- ordered intermetallics (Fig. 1.) with high magnetocrystaline anisotropy are perceived as functional materials for high-density magnetic data storage devices. Since FePt shows the highest superstructure stability, it seems to be the most promising

candidate for the application. Recent experimental studies [1], and computer simulations [2], have consistently indicated that $L1_0$ superstructure in FePt nano-particles or nano-layers is destabilised by free surfaces. However, the atomistic origin of the observed behaviour is still an open question. Recent MC simulations suggested the explanation in terms of either surface Pt precipitation [3], or surface induced disorder [2]. The present study yields further elucidation of the problem.

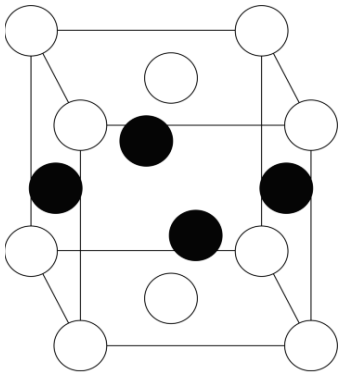

Figure 1. $L1_0$ unit cell:
● A-sublattice, ○ B-sublattice

2. Atomistic simulations

Simulated samples were built of 40^3 fcc unit cells (256000 atoms) initially perfectly ordered in a *c*-variant $L1_0$ superstructure. Layers limited by (001) free surfaces were modelled by imposing periodic boundary conditions in [100] and [010] directions only. Ising Hamiltonian with nn and nnn pair interactions was used. The pair-interaction energies were evaluated for FePt within a combined ab-initio - Cluster Expansion procedure [4,5] and yielded the "order-disorder" transition temperature T_t = 1580 K in the bulk system [5]. After introducing one vacancy into the system isothermal evolutions of its atomic configuration were simulated allowing the atoms to change their positions exclusively by jumping to nn vacancies with probabilities following from Glauber dynamics (see [5]). Results were averaged over 32 independent parallel simulation runs. The most important parameters, whose MC-time dependence was monitored were: total configurational energy *E* of the system and Bragg-Williams LRO parameter η_C defined for the *c*-variant $L1_0$ superstructure.

The MC simulations revealed four processes occurring in the FePt layers at T > 0 K and showing specific time scales:

1. Homogeneous disordering (generation of antisite defects all over the layer volume). The process exhibited exactly the same range and time scale as in the bulk.
2. Nucleation of *a*- and *b*-variant $L1_0$ domains within the $L1_0$ unit cells touching the Fe free surface of the layer.
3. Growth of the nucleated *a*- and *b*-variant $L1_0$ domains inward the layer. Fluctuating character of the APB motion was observed and definite temperature dependence of an effective layer penetration depth of the process was recognised only after averaging over independent simulatons.
4. Relaxation of the microstructure of *a*- and *b*-variant $L1_0$ domains. This process was studied mainly by means of mesoscale simulations (see Section 3), but was also reflected by the atomistic ones as the related relaxation of the system configurational energy.

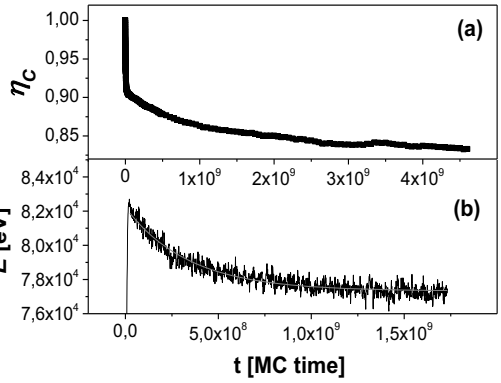

Figure 2. MC-time dependence of surface LRO parameter η and configurational energy *E* at fixed temperature.

The processes 1 and 2 showed up as specific relaxations of η_C definitely exhibiting two distinct time scales (Fig. 2a): the shorter one assigned to the nucleation of *a*- and *b*-variant domains. The process 3 resulted in a relaxation of E (Fig.2b) [6].

3. Voxel-based meso-scale simulations of $L1_0$ APD microstructure relaxation

The simulated sample was built of 128 x 128 x 10 adjacent cubes (voxels) treated as antiphase microdomains and interacting mutually with APB energies evaluated within the atomistic simulations (Section 2). Similarly as in Section 2 two-dimmensional periodic boundary conditions were applied and, therefore, the sample was limited by two free surfaces. The value of the energy loss resulting from a c-variant voxel located at the surface also stemmed from atomistic simulations. Voxels representing particular $L1_0$ variants were initially distributed at random. Specific Glauber-type MC procedure [7] simulated the spontaneous re-orientation of the neighbouring voxels and, in consequence, formation of the equilibrium APB microstructure characterized by the volume fraction and average size of the domains. The resulting surface domain microstructures are shown in Figs. 3 and 4.

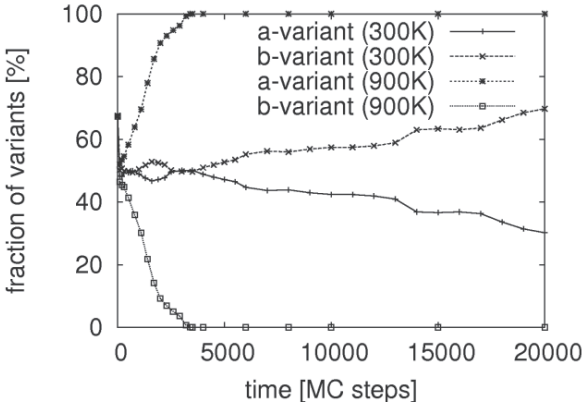

Figure 3. MC-time dependence of the a- and b- $L1_0$ variant surface domain fractions at 300K and 900K.

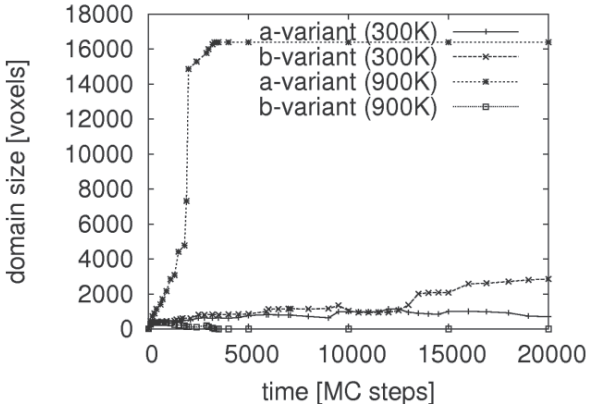

Figure 4. MC-time dependence of average volume of the a- and b- $L1_0$ variant domains at 300K and 900K.

After an immediate escape of the c-variant voxels from the surface, its microstructure was composed of a- and b-variant domains, whose volume fractions and average sizes evolved in time. At higher temperature the coagulation process markedly dominated leading to a reduction of the APB density.

f4. Discussion

The (001) free-surface-induced destabilisation of the $L1_0$ superstructue *c*-variant in a layer of FePt was revealed by atomistic MC simulation of the Ising system. The phenomenon may be of substantial importance for the technology of high-density magnetic storage devices basing on this material as just the chemical ordering in the $L1_0$ *c*-variant yields the off-plane easy magnetisation, crucial for the technology. The $L1_0$ *c*-variant re-orientation into a mosaic of *a*- and *b*-variants predicted by our simple model has recently been experimentally observed in FePt by means of CEMS [8].

5. Acknowledgements

Work pursued within the European Action COST P19; supported by the Polish Ministry of Science and Higher Education (Grant no. COST/202/2006), by the governments of France and Poland (POLONIUM) and by PW ICM Warsaw (grant G31-5). R.K. and S.M. collaborated within the International Fellowship at Queen's University, Belfast, UK.

References

[1] T. Miyazaki, O. Kitakami, S. Okamoto, Y. Shimada, Z. Akase, Y. Murakami, D. Shindo, Y. K. Takahashi, K. Hono, "Size Effect on the Ordering of $L1_0$ FePt Nanoparticles", Physical Review B, **72,** 144419 (2005).

[2] M. Müller, P. Erhart, K. Albe, "Thermodynamics of $L1_0$ Ordering in FePt Nanoparticles Studied by Monte Carlo Simulations Based on an Analytic Bond-Order Potential", Physical Review B, **76,** 155412 (2007).

[3] B. Yang, M. Asta, O.N. Mryasov, T.J. Klemmer, R.W. Chantrell, "Equilibrium Monte Carlo Simulations of A1–$L1_0$ Ordering in FePt Nanoparticles", Scripta Materialia, **53,** 417 (2005).

[4] T. Mohri, Y. Chen, "First-Principles Investigation of $L1_0$ - Disordered Phase Equilibrium in Fe-Pt System", Materials Transactions, **43**, 2104 (2002).

[5] M. Kozłowski, R. Kozubski, V. Pierron-Bohnes, W. Pfeiler, "$L1_0$-Ordering Kinetics in FePt Nano-Layers: Monte Carlo Simulation, Computational Materials Science, **33,** 287 (2005).

[6] M. Kozłowski, R. Kozubski, J. Wrobel, T. Wejrzanowski, K.J. Kurzydlowski, Ch. Goyhenex, V. Pierron-Bohnes, M. Rennhofer, S. Malinov, "Atomic Ordering in Nano-Layered $L1_0$ AB Binaries: Multiscale Monte Carlo Simulation" – submitted for publication in Intermetallics.

[7] Q. Yu, S.K. Esche, "Three-Dimensional Grain Growth Modeling with a Monte Carlo Algorithm, Materials Letters **57**, 4622 (2003).

[8] M. Rennhofer, B. Sepiol, G. Vogl, M. Kozlowski, R. Kozubski, B. Laenens, A. Vantomme, J. Meersschaut, "Re-Orientation Behaviour of c-Variant FePt Thin Films", Diffusion-Fundamentals, **6,** 45.1 (2007); Physical Review Letters – submitted for publication.

Modeling Dynamic Behavior of Nanowires by Using a Semi-Continuum Approach

Guoliang Huang[1,2] and Fei Song[2]

[1]Department of Systems Engineering, University of Arkansas at Little Rock, Little Rock, Arkansas, 72204, USA
[2]Department of Applied Science, University of Arkansas at Little Rock, Little Rock, Arkansas, 72204, USA
(E-mail: glhuang@ualr.edu)

ABSTRACT

The extensive computing effort of molecular dynamics (MD) boosted the motivation of developing new tools that can offer the similar simplicity of continuum mechanics and the ability to account for the nano-characteristics of the material. In the study, we propose a semi-continuum approach to model the dynamic behavior of nanowires. The surface relaxation is also taken into account by using the proposed imperfection of the coordination numbers (CNs) of a surface atom. In the model, the continuum description is used along the length direction, and the discrete feature is kept in both the width and thickness directions considering the real geometry of the nanowires. The equation of motion of the nanowires can be derived by using the energy approach. The accuracy of the model is verified by comparing the dispersion relations of the longitudinal wave propagation obtained from the current model with those obtained from the lattice model. The size dependent Young's modulus of the nanowires is found and discussed. The influences of coupled size dependence and surface relaxation on the dynamic behavior of nanowires are demonstrated.

1. Introduction

Nanowires and nanotubes are attractive components for future multifunctional nanoelectromechanical systems (NEMS) because they can serve as basic building blocks for the bottom-up assembly of integrated nanosystems, and simultaneously function as bridging wires that access and interconnect devices. For long-term reliability of various devices at nanoscale, researchers should deeply understand the mechanical properties of nanowires. One primary reason for such an intense interest in nanowires lies in the unique physical properties due to their small sizes, which are not seen in the corresponding bulk material. Such nonbulk phenomena has been found in mechanical, electrical, thermal, and optical properties of both metallic, polymer, and semiconducting nanowires.

Due to the nanometer dimensions of nanowire structures, these materials are characterized by having a relatively large surface area to volume ratio, which has an appreciable effect on material mechanical properties at nanoscale as what is experimentally observed and theoretically predicted. Many different approaches have been developed to try to understand the size-dependent elastic behavior and surface relaxation of the nanowires. Molecular dynamics (MD) could be a solution in the long run [1]. However, it is well known the capability of this approach is limited by its need of prohibitive computing efforts. It is essential to develop new tools that

offer the similar simplicity of continuum mechanics and the ability to account for the nano-characteristics of the material.

In this study, a multiscale semi-continuum approach is proposed to study the mechanical behavior of the nanwire. Specific attention will be paid to discussing the dynamic behavior of the nanowire considering the coupled the size and surface relaxation effects. In the approach, the discrete atomic characteristics in the width/thickness direction of the nanowires are retained. However, the continuum description can be applied in the remaining length direction to achieve simplicity since their length dimension is much larger. Meanwhile, the surface relaxation effects are considered by using the proposed imperfection of the coordination numbers (CNs) of a surface atom [2]. The accuracy of the model is verified by comparing the dispersion relations of the longitudinal wave propagation obtained from the current model with those obtained from the lattice model. The size dependent Young's modulus of the nanowires is found and discussed. Finally, the influences of coupled size and surface relaxation on the dynamic behavior of nanowires are demonstrated quantitatively.

2. Semi – continuum model of nanowires

For simplification and comparison, a simple cubic lattice model is used to represent a square cross-sectional nanowire with the uniform width and thickness *h* and infinite length, as shown in Fig 1. The discrete solid dots denote atoms *m* and the short solid lines connecting these dots denote atomic bonds. Along both the width and the thickness directions, the model is assumed to have $2N+1$ (N=1, 2, 3,…,) atom layers starting from the $-N$th layer to Nth layer. The x axis is along the length direction of the nanowire, and y and z axes are along the width and thickness directions, respectively. The origin of the coordinate is located at the center of the nanowire. Although ideal cubic nanostructure is chosen for simplicity, the approach proposed can be readily extended to the nanowires with other crystal structures. To calculate deformation energy of the nanowires, nine kinds of representative cells in total are considered, as shown in Fig 1.

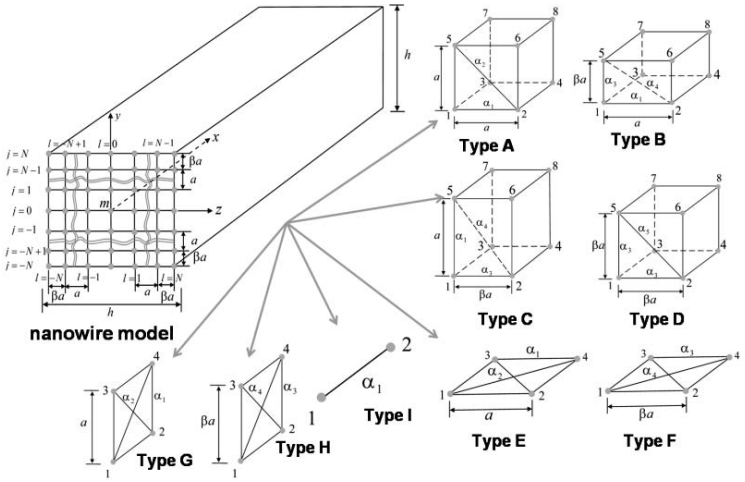

Figure 1. Nanowire model and its nine types of representative cells.

To consider the surface relaxation effect in this model, the proposed imperfection of the coordination numbers (CNs) of a surface atom, which causes the remaining bonds of the surface

atom to relax spontaneously, will be employed [2]. The CN-imperfection-induced bond relaxation can be defined as $a_i = \beta_i a$, where a represents the bulk value of bond length, the subscript i is the ith atomic layer, and β_i is the relaxation coefficient. The relaxation may be in expansion (β_i>1) or in contraction (β_i<1).

Then the total deformation energy of the nanowire, W_T can be obtained by summing up the deformation energy of all the cells [3]. The total kinetic energy of the atoms in the representative volume element of the nanowire is

$$T_T = \frac{1}{2} m \sum_j \sum_l [(\dot{u}_{(j,l)})^2 + (\dot{v}_{(j,l)})^2 + (\dot{w}_{(j,l)})^2] \quad (1)$$

where m is the mass of each atom, and a dot represents the derivative with respect to time t. Considering the assumption of small deformation, the elastic strains in the nanowire can be defined as [3]

$$\varepsilon_{xx}^{(j,l)} = \frac{\partial u_{(j,l)}}{\partial x}, \ \overset{\Delta}{\varepsilon}{}_{yy}^{(j,l)} = \frac{v_{(j+1,l)} - v_{(j,l)}}{y_{j+1} - y_j}, \ \overset{\Delta}{\varepsilon}{}_{zz}^{(j,l)} = \frac{w_{(j,l+1)} - w_{(j,l)}}{z_{l+1} - z_l}, \overset{\Delta}{\gamma}{}_{xy}^{(j,l)} = \frac{\partial v_{(j,l)}}{\partial x} + \frac{u_{(j+1,l)} - u_{(j,l)}}{y_{j+1} - y_j} \quad (2a)$$

$$\overset{\Delta}{\gamma}{}_{yz}^{(j,l)} = \frac{v_{(j,l+1)} - v_{(j,l)}}{z_{l+1} - z_l} + \frac{w_{(j+1,l)} - w_{(j,l)}}{y_{j+1} - y_j}, \overset{\Delta}{\gamma}{}_{xz}^{(j,l)} = \frac{\partial w_{(j,l)}}{\partial x} + \frac{u_{(j,l+1)} - u_{(j,l)}}{z_{l+1} - z_l} \quad (2b)$$

Therefore, energy density W_0 and T_0 can be expressed in terms of elastic strains. The equations of motion of the nanowire material can be obtained by using the Hamilton's principle

.

3. Elastic constants of nanowires

Fig 3 shows the Young's modulus E with respect to the number of atomic layers (2N+1) for different relaxation coefficients β. It is evident that the Young's Modulus E is all size dependent for each given relaxation coefficient β. The Young's modulus E varies with the decrease of the atomic layer number as the atomic layer numbers are less than 40. It varies significantly when the atomic layer numbers are less than 15. The surface relaxation has also a remarkable effect on the Young's modulus of nanowires especially when the numbers of atomic layers are small.

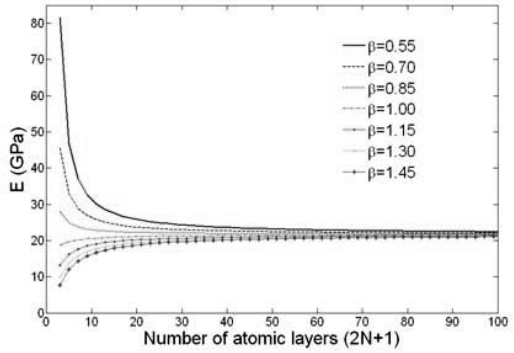

Figure 2. Young's modulus E as a function of number of atomic layers for different relaxation coefficients β.

4. Longitudinal wave propagation in nanowires

Fig 3(a) shows the comparison of dispersion curves obtained by the exact solution and the semi-continuum model. The good agreement between the two models can be observed for ka<1.0.

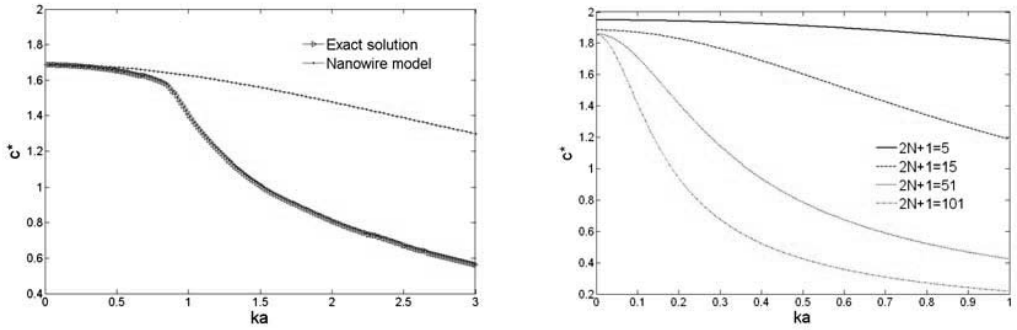

(a) (b)

Figure 3. (a). Model validation,
(b). Dispersion curves for the nanowires with varying atomic layer numbers.

Fig 3(b) shows the nanowire's size effects upon the longitudinal wave dispersion relations. In the figure, the atomic layer number (2N+1) is selected as 5, 15, 51 and 101, respectively. With the increase of the nondimensional wave number ka, the nondimensional phase velocity c^* becomes more dependent on the atomic layer numbers of the nanowire for the given relaxation coefficient β.

5. Conclusions

In this study, a semi-continuum approach has been developed to model the mechanical behavior of the nanowire. Surface relaxation effects are considered. The size dependent Young's modulus and Poisson's ratio of the nanowire are observed. The influences of atomic layer numbers and surface relaxation on the dynamic behavior of the nanowires are examined.

Acknowledgements

This research was funded, in part, by the National Science Foundation EPSCoR Grant # EPS 0701890.

References

[1] S. J. A. Koh, H. P. Lee, C. Lu, and Q. H. Cheng, "Molecular dynamics simulation of a solid platinum nanowire under uniaxial tensile strain: Temperature and strain-rate effects", Physical Review B **72**, 085414 (2005).
[2] C. Q. Sun, B. K. Tay, X. T. Zeng, S. Li, T. P. Chen, J, Zhou, H. L. Bai, and E. Y. Jiang, "Bond-order–bond-length–bond-strength (bond-OLS) correlation mechanism for the shape-and-size dependence of a nanosolid", Journal of Physics: Condensed Matter **14**, 7781 (2002).
[3] C. T. Sun and H. Zhang, "Size-dependent elastic moduli of platelike nanomaterials", Journal of Applied Physics **93**, 1212 (2003).

Self-healing of Aluminum Oxide Films: Construction of a High-precision Al-O Potential for Molecular Dynamics

Ivan Lazic[1] and Barend J. Thijsse[1]

[1]Department of Materials Science and Engineering, Delft University of Technology, Mekelweg 2, 2628 CD Delft, (E-mail: I.Lazic@tudelft.nl)

ABSTRACT

Molecular Dynamics simulations of the self-healing capacity of Al oxide coatings, e.g. after scratching, demand the best possible description of Al oxide growth. Only with a fully developed and well-calibrated potential, the factors that control the diffusion of Al and O under locally varying Al/O ratios can be studied. To obtain this, a new "reference free" version of the Modified Embedded Atom Method (RFMEAM) potential is developed, together with a Charge Transfer Ionic Potential (CTIP). This allows a highly advanced description of atomic interaction: angular forces for the relatively low-coordinated crystal structures such as metal oxides, and dynamic charge transfer between Al and O to handle instantaneous local composition variations. As Coulomb solver we use PPPM. We present the most accurate Al-O potential up to now, being the result of fitting RFMEAM+CTIP to a large *ab initio* database of Al-O structural energies using a recent method which separates the electrostatic and non-electrostatic fitting steps.

1. Introduction

Surface oxides on Al alloys are "self-healing" in that they quickly re-form after damaging. Studying such a phenomenon using molecular dynamics (MD) requires sophisticated interatomic potentials. In such metal/metal-oxide systems, ionic bonds give rise to long-range Coulomb interaction, and at interfaces, surfaces, and defects the atomic charges are not fixed but vary with local conditions. Al oxides have a relatively open structure, suggesting that angular terms in the potential play an important role. We present a potential that combines a new „Reference Free" Modified Embedded Atom Method (RFMEAM) potential (explained below) for the non-electrostatic interactions with a Charge Transfer Ionic Potential (CTIP) [1] for the electrostatics. We aim at a general potential model, applicable also to other technologically important materials such as the relatively open oxides of Si and to the mildly ionic III-V and II-VI semiconductors Here we report the successful and demanding fit of this potential for the Al-O system, aplying a novel fitting method [2] to *ab initio* computed energies for Al_xO_y compounds. We have used the iterative Particle-Particle-Particle-Mesh (PPPM) method as Coulomb solver [3] and the Vienna Ab initio Simulation Package (VASP) [4] for the *ab initio* energies.

2. The RFMEAM+CTIP potential

The energy U of a system of N atoms is the sum of a non-electrostatic and an electrostatic part, $U = U_{nes} + U_{es}$, where

$$U_{nes} = \sum_{i=1}^{N} \sum_{\substack{j=1 \\ j \neq i}}^{N} \frac{1}{2} \Phi_{ij}(r_{ij}) + \sum_{i=1}^{N} F_i(x_i) \tag{1}$$

is the non-electrostatic (RFMEAM) part. The embedding functions $F(x)$ for each chemical type (in this work Al and O) and the pair potential functions $\Phi(r)$ for each chemical type combination (AlAl, AlO, and OO) are given by

$$\Phi(r) = -E_p(1 + \eta + c_p\eta^2 + d_p\eta^3)e^{-\eta}, \;\; \eta = \alpha_p\left(r/r_p - 1\right) \;\; F(x) = A_e\sqrt{x}\ln\sqrt{x} + C_e x, \tag{2}$$

where p and e denote fitparameters; x_i is proportional to the square of the "background electron density at atom i" and contains all dependencies on the i-angle in the ijk atom triplets,

$$x_i = \sum_{l=0}^{3} t_i^{(l)} \sum_{j \neq i} \sum_{k \neq i} p_j^{(l)} e^{-q_j^{(l)} r_{ij}} \, p_k^{(l)} e^{-q_k^{(l)} r_{ik}} P^{(l)}(\cos\theta_{jik}). \tag{3}$$

Here, $t^{(l)}$, $p^{(l)}$, $q^{(l)}$ (l = 0, 1, 2, 3) are fitparameters for each chemical type (except $t^{(0)} = 1$), and $P^{(l)}$ is the Legendre polynomial of order l. For simplicity, Eqs. (1-3) are given without angular and radial cutoff functions. New in this RFMEAM format, compared to classical MEAM [5], is the extension of the embedding function by one term and the abandonment of the concept of "reference structures". The pair potentials are parametrized (Morse-like) functions rather than functions prescribed by equations of state of particular crystal phases. Eqs. (1-3) are computationally easier to handle and more powerful than the classical MEAM format.

For the electrostatic (CTIP) part we use the potential model proposed by Zhou and coworkers [1]. The electrostatic energy U_{es} is given as ionization plus Coulomb energy,

$$\begin{aligned} U_{es} = {} & \frac{1}{2}\sum_{i=1}^{N} 2\omega\left(\left(1 - \frac{q_i - q_{\min,i}}{|q_i - q_{\min,i}|}\right)(q_i - q_{\min,i})^2 + \left(1 - \frac{q_{\max,i} - q_i}{|q_i - q_{\max,i}|}\right)(q_i - q_{\max,i})^2\right) + \frac{1}{2}\sum_{i=1}^{N}\left(2\chi_i q_i + J_i q_i^2 + q_i(\varphi_{mesh}(\mathbf{q}) - \varphi_{self}(q_i))\right) + \\ & \frac{1}{2}\sum_{i=1}^{N}\sum_{\substack{j=1 \\ j \neq i}}^{N} k_c\left(q_i Z_j([j \mid f_i] - [f_i \mid f_j]) + q_j Z_i([i \mid f_j] - [f_i \mid f_j])\right) + \frac{1}{2}\sum_{i=1}^{N}\sum_{\substack{j=1 \\ j \neq i}}^{N} k_c q_i q_j\left(\frac{1}{r_{ij}} erfc\left(\frac{r_{ij}}{\sigma}\right) + ([f_i \mid f_j] - \frac{1}{r_{ij}})\right), \end{aligned} \tag{4}$$

where χ and J are electronegativity and electrostatic hardness, and $[a \mid f_b]$ and $[f_a \mid f_b]$ denote the Coulomb integrals $[a \mid f_b] = \int_{V_b} \frac{f_b(r_b)}{r_{av}} dV_b$ and $[f_a \mid f_b] = \int_{V_a}\int_{V_b} \frac{f_a(r_a) f_b(r_b)}{r_{vv}} dV_a dV_b$, with dV_a

and dV_b the two integrating volume units; r_a the center distance between atom a and dV_a; r_b between atom b and dV_b; r_{av} between atom a and dV_b; and r_{vv} between dV_a and dV_b. This is according to [1], in which an atom does not have a single pointlike charge, but a pointlike part and a distributed part, $\rho_i^{atom}(r) = Z_i\delta(r) + (q_i - Z_i)f_i(r)$ with Z_i is a model parameter for each chemical type. The distributed part has the form $f_i(r) = \xi_i^3 \exp(-2\xi_i r)/\pi$, with ξ_i also a parameter. The first term in Eq. (4) softly limits an atom's charge between $q_{\min}$ and $q_{\max}$ to account for chemical valence (ω = 20.0 eV/e^2). The vector $\mathbf{q} = (q_1, q_2, q_3, ..., q_N)$ symbolizes all charges, $\varphi_{self}(q_i) = 2k_c q_i / \sigma\sqrt{\pi}$ is the self-electrostatic potential ($k_c = 1/4\pi\varepsilon_0$) and $\varphi_{mesh}(\mathbf{q})$ is the long-ranged Coulomb part determined by solving Poisson equation within the PPPM method [3]. The charges on the atoms are determined by minimizing the total electrostatic energy U_{es} under the condition $\sum_{i=1}^{N} q_i = 0$, using the conjugate gradient method [6]. We explore the property that the non-electrostatic, Eq. (1), and the electrostatic part, Eq. (4), are completely independent.

3. Fitting the potential to *ab initio* Al/O data

In this work we determine the RFMEAM+CTIP parameters for the Al/O system according to a two-step strategy analogous to the one in ref. [2]. First, we determine the seven electrostatic CTIP parameters $\Delta\chi_{\text{O-Al}}$, J_{Al}, Z_{Al}, ξ_{Al}, J_{O}, Z_{O}, ξ_{O}, such that the electrostatic potential field $\varphi(\mathbf{r})$ calculated using the CTIP model (similarly to Eq. (4)) optimally fits the *ab initio* field in a large number of mesh points 1.5 Å outside the atomic cores. The regions inside the atomic cores are avoided because here the *ab initio* results cannot be trusted [2]. The $\varphi(\mathbf{r})$ fits are performed for Al_xO_y crystal structures of fourteen different types (Tab. 1).

Table 1. Charges on the Al and O atoms according to the CTIP model using parameters optimized in this work. Compounds in parentheses are standard crystal structures. An asterisk denotes a value averaged over non-equivalent atoms.

Crystal structure	q_{Al} [e]	q_{O} [e]	Crystal structure	q_{Al} [e]	q_{O} [e]
AlO_2 (CaF_2)	2.02	-1.01	AlO (CuAu)	1.46	-1.46
α-Al_2O_3	2.90	-1.93	$Al_{20}O_{16}$ (*I4$_1$/amd*) *	1.63	-2.04
γ-Al_2O_3 - Fd3m *	2.74	-1.83	Al_2O (Co_2B) *	1.02	-2.04
γ-Al_2O_3 – I4$_1$/amd*	2.74	-1.83	Al_3O (Fe_3B) *	0.69	-2.07
AlO (ZnS)	2.09	-2.09	Al_4O (Fe_4C) *	0.53	-2.11
AlO (NaCl)	2.07	-2.07	O in fcc Al ($Al_{32}O$) *	0.06	-2.04
AlO (CsCl)	2.04	-2.04	fcc Al	0	0

Second, the remaining non-electrostatic RFMEAM parameters of the potential (of which there are 60 in total, namely 39 in Eqs. (2-3) and 21 in the cutoff functions [7]) are determined by fitting Eq. (1) to the *ab initio* energies calculated for the Al-O systems of Tab. 1 over a range of lattice constants. From these *ab initio* energies the electrostatic CTIP part optimized in the previous step was first subtracted. This controls the charge transfer optimization without having to assume charges, while keeping the best accuracy for the total energies.

4. Results and conclusions

Fig. 1a shows the *ab initio* values of φ in an array of **r** points for the two most important Al oxides, α-Al_2O_3 and γ-Al_2O_3. Fig. 1b shows the fit errors of the best fit, with average values 0.27 eV/*e* and 0.92 eV/*e*, respectively. In [1] these values are 0.61 eV/*e* and 0.87 eV/*e*, implying that our CTIP fit for α-Al_2O_3 (the crystalline ground state) is better by more than a factor two, while for γ-Al_2O_3 it is approximately the same. The charges on the atoms, which were not explicitly included in the fit, are listed in Tab. 1 and have very realistic values. Note especially that in the structures important for the beginning of oxidation (large Al/O ratio), O atoms obtain charge values close to the valence (–2 *e*) as they should. A single O in fcc Al, for example, obtains –2.04 *e*, which is an improvement over the value –0.96 *e* resulting from the parameters in [1].

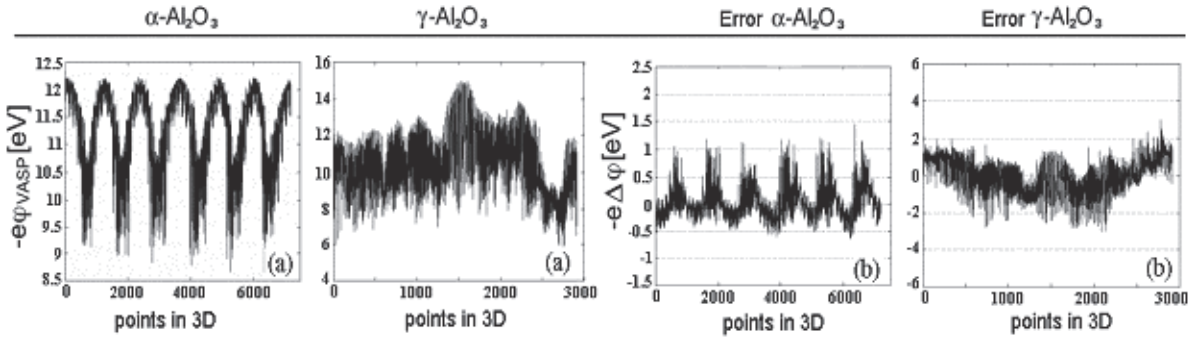

Figure 1. Electrostatic potential field φ multiplied by elementary charge (–*e*) in the 3D mesh points 1.5 Å away from the atom centers. The horizontal axis numbers the points in which the field is shown. (a) calculated *ab initio* for α-Al_2O_3 (left) and γ-Al_2O_3 (right), (b) Fit errors of the best fit of the CTIP potential.

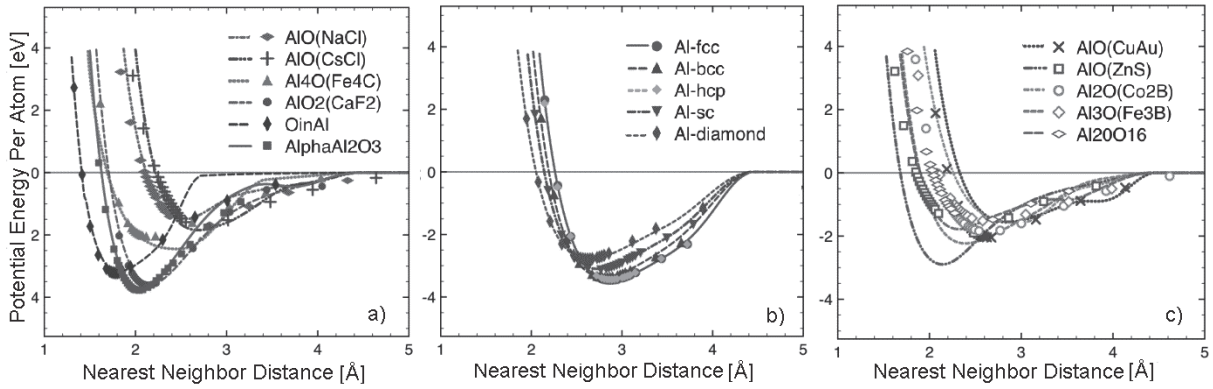

Figure 2. Fit of the non-electrostatic RFMEAM part of the potential. Data points are *ab initio* energies from which the electrostatic energy has been subtracted. Lines show the best simultaneous fit of all equations of state $U_{nes}(R)$, Eq. (1), with *R* the nearest neighbor distance. a) Al_xO_y structures with relatively low minimum energies, b) various Al structures, c) Al_xO_y structures with relatively high minimum energies.

The fit result for the remaining, non-electrostatic part of the potential (RFMEAM) is shown in Fig 2. All structures of Tab. 1 were included in the fit, together with bcc, fcc, hcp, sc and dc Al. With the exception of a few Al_xO_y structures with relatively high minimum energies and therefore of less importance in structural competition (Fig. 2c), the fit is excellent (Fig. 2a), even for pure Al (Fig. 2b).

In conclusion, Tab. 1 and Figs. 1 and 2 show that a new, high-precision Al-O potential has been constructed in this work. Molecular dynamics simulations of initial oxidation are underway.

References

[1] X.W. Zhou, H. N. G Wadley, J.-S. Filhol and M.N. Neurock, Phys. Rev. B **69**, 035402 (2004).
[2] E. Bourasseau, J.B. Millet, L. Mondelain and P.M. Anglade, Mol. Simulat. **31**, 705 (2005).
[3] R.W. Hockney and J.W. Eastwood, *Computer Simulation Using Particles*, McGraw-Hill, New York (1981).
[4] G. Kresse and J. Furthmuller, Phys. Rev. B **54**, 11169 (1996).
[5] M.I. Baskes, Phys. Rev. B **46**, 2727 (1992).
[6] W.H. Press, S.A. Teukolsky, W.T. Vetterling and B.P. Flannery, *Numerical Recipes in C*, Cambridge University Press, 2nd edition (1992).
[7] B.J. Thijsse, Nucl. Instrum. Methods Phys. Res. B **288**, 198 (2005).
[8] M.I. Baskes, *Modified Embedded Atom Method Calculations of Interfaces*, Sandia National Laboratories Livermore, CA 94551-0969, Edited by S. Nishijuna and H. Ondera (1996).

The Influence of Fe on the Zr Self-diffusion: An Ab-initio Assessment

R.C. Pasianot[1,2,3], V.P. Ramunni[2], R.A. Pérez[1,2], M. Weissman[2,4], J.R. Fernández[1,2,3]

[1]Depto. Materiales CNEA-CAC, Avda. Gral. Paz 1499, 1650 San Martín, Argentina, (E-mail: pasianot@cnea.gov.ar)
[2]CONICET, Avda. Rivadavia 1917, 1033 Buenos Aires, Argentina;
[3]Instituto Sábato UNSAM/CNEA, Avda. Gral. Paz 1499, 1650 San Martín, Argentina;
[4]Depto. Física CNEA-CAC, Avda. Gral. Paz 1499, 1650 San Martín, Argentina.

ABSTRACT

As is well known the diffusion in hcp-Zr does not follow the accepted common behavior for metals, namely,
i) Arrhenius law is not obeyed.
ii) Some 3d transition elements, Fe, Co, and Ni among them, are ultra fast diffusers, with diffusivities exceeding in about 9 orders of magnitude the one for Zr self-diffusion.
iii) Small amounts, such as some few tens of ppm, of the above elements seem to be responsible for a remarkable enhancement of self and substitutional diffusion. Particularly Fe because of its unavoidable presence in commercial Zr samples.

In the present work we apply the ab-initio electronic structure code Siesta, coupled with a recently developed transition state finding technique, the MONOMER, in an effort to assess the equilibrium and barrier, structure and energy, of some point defects in the vicinity of the Fe impurity. The results are discussed in the light of experimental measurements and available semiempirical models.

Scale Dependent Micro-structural Evolution of Snow

Henning Löwe, Johanna Spiegel, Bernd Pinzer, Martin Schneebeli

WSL, Swiss Federal Institute of Snow and Avalanche Research, SLF
Flüelastrasse 11, 7260 Davos Dorf, Switzerland
(E-mail: loewe@slf.ch)

ABSTRACT

From a material science point of view, snow is a polycrystalline, porous aggregate of ice particles and must be regarded as a complex system far from equilibrium on all experimentally relevant timescales. The evolution of the microstructure, commonly referred to as snow metamorphism is very sensitive to the externally applied driving mechanisms which are strongly varying in nature. To understand the evolution of the microstructure under idealized conditions we have analyzed the dynamics of snow in a controlled, isothermal environment in a cold lab at different temperatures by means of computer tomography. We characterize the dynamics of the microstructure in terms of the evolution of characteristic length scales of the structure. The long-time evolution of the characteristic size of the ice-network follows a dynamic scaling relation which is in agreement with coarsening theory of a conserved order parameter field. In contrast, the characteristic size of the pore network shows a different time evolution indicating the simultaneous densification of the snow sample. This must be thus attributed to a different mechanism, i.e. gravity. An outlook is given for the evolution of macroscopic length scales during metamorphism embodied in the thermal conductivity or the algebraic connectivity of the ice-network.

Multi-scale Modeling of Unoriented Thermoplastic Elastomers with Lamellar Morphology

Vikranth Racherla[1] and Pedro Ponte Castañeda[2]

[1]Laboratoire de Mécanique des Solides, Ecole Polytechnique, 91128 Palaiseau, France (E-mail: vikranth@lms.polytechnique.fr)
[2]Department of Mechanical Engineering and Applied Mechanics, University of Pennsylvania, Philadelphia, PA 19104 (E-mail: ponte@seas.upenn.edu)

ABSTRACT

The finite-deformation behavior of unoriented thermoplastic elastomers (TPEs) with lamellar morphology is investigated using a two-scale homogenization procedure. For the class of microstructures considered here, a representative volume element in the undeformed configuration is composed of a large number of randomly oriented grains made up of perfect lamellar structures of hard (glassy or crystalline) and soft (rubbery) phases. The procedure adopted here directly accounts for the initial volume fraction of the hard and soft phases, the initial distribution of the lamination orientations, the average grain shape, and the mechanical behavior of the individual phases. This method can be used not only to estimate the overall stress-strain behavior of TPEs but also to estimate the microstructure evolution (e.g. the evolution of average lamination directions in grains) and to predict the onset of macroscopic instabilities (i.e., loss of strong ellipticity). For unoriented TPEs with lamellar morphology, in line with small-angle X-ray scattering observations, the model predicts that at finite deformations the majority of the lamination orientations are at around 20 degrees from the largest principal stretch direction (as opposed to being perfectly aligned with the principal stretch direction). Large rotations of the layers are observed even at moderate strains - particularly when there is a large contrast in mechanical properties of hard and soft phases - leading to a softening effect in the overall stress-strain behavior and to the onset of macroscopic instabilities.

We thank the Agence Nationale de la Recherche (France) and the National Science Foundation (USA) through the grant CMMI-0654063 for funding the work of V. R. and P.P.C, respectively.

Interfacial Microstructures in Martensitic Transitions: From Optical Observations to Mathematical Modeling

Hanuš Seiner[1,2], Ondřej Glatz[1,2], Lucie Bicanová[1,2], Petr Sedlák[1,2]

[1]Laboratory of Ultrasonic Methods, Institute of Thermomechanics ASCR, Dolejškova 5, 18200 Prague 8, Czech Republic
[2]Faculty of Nuclear Sciences and Physical Engineering, Czech Technical University in Prague, Trojanova 13, 12000 Prague 2
(E-mails: hseiner@it.cas.cz, o.glatz@glatz.cz, bicanova@it.cas.cz, psedlak@it.cas.cz)

ABSTRACT

A phenomenological mathematical model of thermally driven martensitic transitions in shape memory alloys is constructed, such that it adopts all main findings from the optical observations done recently on single crystals of the Cu-Al-Ni alloy. Based on the assumption of minimal mechanical work being done by the transitions front, this model shows that the formation of the X-interfaces (i.e. of interfacial microstructures which are not energy minimizers) is more efficient than any transition via fully compatible (i.e. energy minimizing) microstructures.

1. Introduction

Although the materials with reversible martensitic transitions (especially the shape memory alloys, [1]) have been a subject of an intensive theoretical research in the past thirty years, the rules governing the coupling between thermal and mechanical phenomena in these materials are still not sufficiently known. One of the cases where such kind of coupling plays a key role is the phenomenon of the mechanical stabilization: For some purely thermally driven transitions in these materials, the transition fronts must be accompanied by collective reorientation of the microstructure, i.e. by formation and propagation of the so-called interfacial microstructures. As the reorientation of the microstructure is energetically costly, this effect shifts the transition temperatures. In a recent paper [2], the authors have brought an experimental evidence that these interfacial microstructures, at least for the Cu-Al-Ni alloy, always have a very specific morphology, for which a mutual intersection of two habit planes is typical (so-called X-interfaces, firstly observed in In-Tl alloy by Basinski and Christian [3]). An example of such X-interface in the Cu-Al-Ni alloy is given in Fig.1.

From the optical observations, the authors have also identified the micromechanisms of motion of these microstructures under thermal loading, showing that the mobility is always enabled by nucleation and growth of individual martensitic needles, i.e. thin sharp plates of one martensitic variant in another. The elastic resistance of the material against such nucleation-and-growth process seems to be the main reason for the mechanical stabilization.

2. Mathematical model

The classical *mathematical theory of martensitic microstructures* (developed in 1980s by Ball and James [4]) predicts formation of such microstructures that the entire Helmoltz free energy of the observed volume of the material is minimal for given boundary conditions. However, as shown by Ruddock [5], the X-interfaces cannot be such energy minimizers, as the compatibility conditions in this microstructure can be achieved only by presence of elastic strains. Recently, the theory has been partially revised by the authors [6], suggesting that the microstructures forming dynamically during the transition do not necessarily minimize the entire energy, but follow optimal paths along which is the *mechanical work done by the transition front minimal*. Here, we will show that such hypothesis enables a construction of a phenomenological 2D model which sufficiently explains all the main properties of the interfacial microstructures documented in [2].

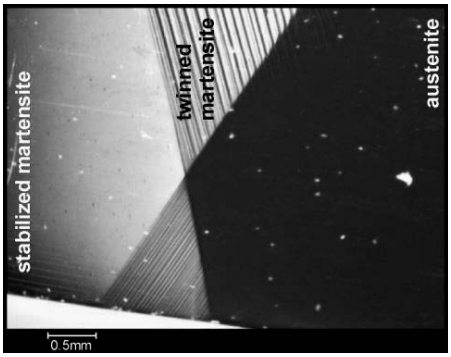

Figure 1. Optical micrograph of an X-interface observed in the Cu-Al-Ni alloy.

Consider now a crystal of a shape memory alloy, undergoing a thermally driven transition from a state with some Helmoltz energy Φ_1 into another state with energy $\Phi_2 < \Phi_1$, and consider that such transition is provided via formation and propagation of some interfacial microstructure. In a (spatially) discrete approximation, the assumption of the minimal work being done by the interface during the transition can be replaced by the assumption that the system always tends jumps to that consecutive state from which is the actual configuration separated by the lowest energetic barrier. In agreement with [7], we can assume that the jumps between individual configurations are enabled by thermal fluctuation. In such case, the probability of a stable jump of the system into another, energetically more preferred configuration is proportional to

$$p(b,T,\Delta\Phi) = \exp(-b/kT) - \exp[-(b+\Delta\Phi)/kT], \tag{1}$$

where is b is the height of the energetic barrier separating the two configurations between which the system jumps, T is the temperature, k is the Boltzmann constant, and $\Delta\Phi$ is the difference (the decrease) of the Helmholtz energy. Obviously, from all possible states with the same energy decrease $\Delta\Phi$, the system most probably chooses such configuration that the barrier b is minimal.

A simplified 2D model was constructed, adopting all the main findings from the optical observations, and following the above outlined hypothesis of thermal fluctuations. The main properties of the model were following:

1. A 2D specimen was considered to undergo a transition from a mechanically stabilized martensite (a single variant) into austenite. The starting configuration included always a small nucleus of austenite separated from the stabilized martensite by a twinned region such that the whole microstructure was fully compatible (i.e. no elastic strains were present). The driving force of the transition was implemented by a difference between the free energy density for martensite (both single variant and twinned) and austenite. Thus, the entire energy of the specimen decreased with increasing volume of austenite.
2. The evolution of the microstructure was parameterized by the location of the crossing point of the habit planes (the centre of the X-interface). Such parameterization restricted the system such that it was able to form either fully compatible interfacial microstructures (as in the starting configuration), or the X-interfaces only. The specimen was, thus covered by a grid of possible states (possible locations of the crossing point) between which it jumped via thermal fluctuations.
3. The presence of the elastic strains was embodied by an increase of the Helmholtz free energy function by some quantity Φ_E, which was considered to be zero for fully compatible microstructures and to increase continuously with the location of the crossing point moving towards the centre of the specimen (similar effect to e.g. the shape function in fracture mechanics).
4. The energetic barriers (the mechanical works being done in each jump) were considered as proportional to the volumes of the martensite being reoriented during the jump. More detailed, this work is equivalent to the work done by growth of individual martensitic needles in the interfacial microstructure, moving the energy concentrations around the tips of the needles through the material. Quantitatively, this work can be evaluated by FEM modeling (Fig. 2).

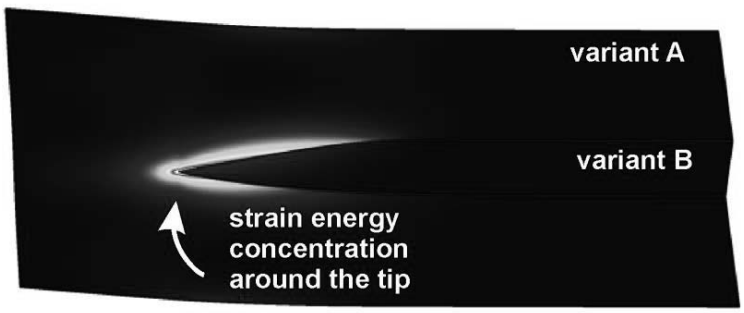

Figure 2. FEM modeling of a martensitic needle of one variant penetrating another variant (two-dimensional model, plane strain, plotted quantity is the strain energy density).

Such model enabled us to find for each configuration the distribution of probability given by Eqn. (1), and, consequently, to find the most probable path of the transition. These results are shown in Fig. 3, where this probability is plotted as a function of the crossing point location of the next, consecutive configuration. In other words, the crossing point will, most probably, jump to the maximum of this function in the next step. Obviously, for the fully compatible configurations (a)-(c), the most probable jumps are into the X-interfaces, whereas for the X-interfaces already formed (d)-(f), the crossing point is attracted to the centre of the specimen. No tendency of the system to return back to fully compatible configuration was observed.

3. Summary

A phenomenological model of thermally induced martensitic transitions in shape memory alloy single crystals was presented. Based on the hypothesis of the minimal mechanical work being done by the transition front during the transition, the model was shown to be able to predict the formation of interfacial microstructures which are not energy minimizers, namely of the X-interfaces.

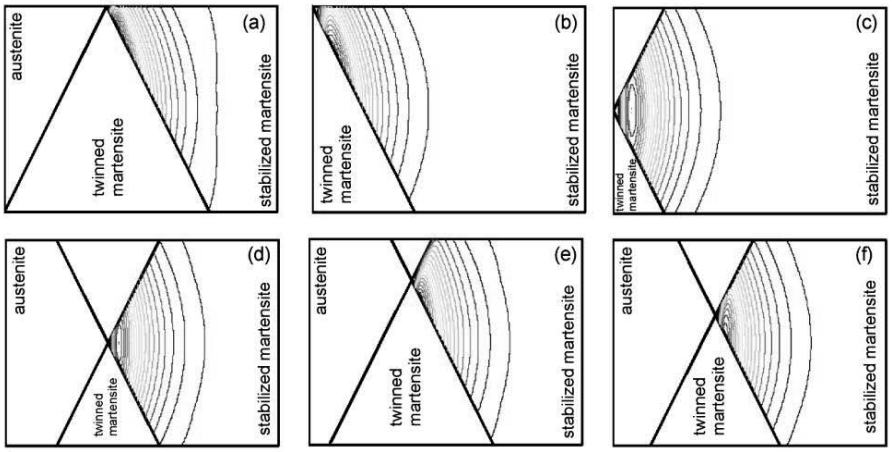

Figure 3. Spatial distributions of probability (1) as a function of the location of the crossing point for various interfacial microstructures.

Acknowledgements

This work was supported by the project A200100627 of the Grant Agency of ASCR, the institutional project of IT ASCR , v.v.i., CEZ:AV0Z20760514, and from the research center 1M06031 of the Ministry of Education of the Czech Republic.

References

[1] K. Bhattacharya, “Microstructure of Martensite”, Oxford University Press, New York, 2003.
[2] H. Seiner, P.Sedlák and M. Landa, “Shape recovery mechanism observed in single crystals of Cu-Al-Ni shape memory alloy”, Phase Transitions, **81**, 537 (2008).
[3] Z.S. Basinski and J.W. Christian “Experiments on the martensitic trasformation in single crystals of Indium-Thallium alloys”, Acta Metallurgica, **2**, 148 (1954).
[4] J.M. Ball and R.D. James, “Fine phase mixtures as minimizers of energy”, Archive for Rational Mechanics and Analysis, **100**, 13 (1987).
[5] G. Ruddock, “A microstructure of martensite which is not a minimiser of energy: the X-interface”, Archive for Rational Mechanics and Analysis, **127**, 1 (1994).
[6] H. Seiner, in preparation, to be submitted to Phys. Rev. Letters, 2008.
[7] R. Abeyaratne and J. K. Knowles, “Evolution of Phase Transitions”, Cambridge University Press, New York, 2006.

Morphology Evolution of Stressed Fiber due to Surface Diffusion

Zhen Liu, Honghui Yu

Mechanical Engineering Department, The City College and Graduate Center of CUNY, New York, NY 10031
(E-mails: liu9419@me.ccny.cuny.edu, yu@me.ccny.cuny.edu)

ABSTRACT

For a cylindrical fiber under annealing, Rayleigh instability is a well known phenomenon. But a stressed fiber is not always stable even its perturbation wavelength is smaller than its circumference. In this work, we developed a numerical scheme, based on a variational principle, to simulate morphology evolution of a stressed fiber due to surface diffusion. The axisymmetric elastic stress field is solved by using boundary element method and morphology evolution is simulated by using an integral formulation. Under a periodic perturbation, it is found that the stressed fiber can still stay stable, or develop grooves then approach to a steady state shape, or develop cusps and break into droplets. Our simulation will roughly obtain these two stress threshold conditions corresponding to different fiber wavelengths.

1. Introduction

Rayleigh [1] demonstrated that a cylinder of water is unstable in front of sinusoidal perturbations when wavelength is greater than the cylinder circumference, which is well known as Rayleigh instability. Nichols and Mullins [2] obtained same threshold condition for solid cylinder rods under annealing: to minimize the surface energy, a small perturbation may grow and break the cylinder. When a fibre is stressed, it is more unstable. Instabilities exist even the wavelength of the fiber is smaller than the circumference to relax the elastic energy. Colin et al [3] introduced a linear analysis of the morphology instabilities of stressed pore channel. Their calculations showed that the critical wavelength of stressed cylinder is shifted toward shorter values as the stress increases. Our work set up a numerical scheme to simulate the morphology evolution of stressed fiber. The numerical results not only reproduce the linear instability behaviour but also show what will happen after grooves are developed.

2. Numerical Methods

The numerical procedure is similar as our previous work [4]. The difference is that here we focus on axisymmetric surface. In this section, we simply review the procedure.

1.1 Weak Statement for Combined Surface Diffusion and Evaporation-Condensation

Imagine two concurrent processes on a solid surface, surface diffusion and evaporation-condensation. The driving forces F and p for the two processes can be defined by

$$\int_{surface} (F \cdot \delta I + p\,\delta i) dA = -\delta G \tag{1}$$

where $\delta \boldsymbol{I}$ is virtual mass displacement associated with surface diffusion, δi the virtual volume of mass added to a unit area of the solid surface from vapor and δG is the virtual free energy reduction associated with virtual motion of the surface. Since $\delta \boldsymbol{I}$ and δi are independent and arbitrary, Equ (1) defines the driving forces for the two processes locally along the surface. From mass conservation law, $\delta \boldsymbol{I}$ and δi together generate the virtual normal displacement of surface $\delta r_{\mathbf{n}} = \delta i - \nabla \cdot \delta I$. Denote $v_{\mathbf{n}}$ the actual normal velocity of the surface; J the atomic flux and j the volume of mass deposited on a unit surface area per unit time. Assuming linear kinetics laws, we have $J = MF$ and $j = mp$ (Herring [5]), where M and m are mobilities of surface diffusion and evaporation-condensation, respectively. Combining the kinetic laws and the mass conservation law, we have the *weak statement* for combined surface diffusion and evaporation-condensation

$$\int \left\{ \frac{J \cdot \delta I}{M} + \frac{\left(v_n + \nabla \cdot J\right)\left[\delta r_n + \nabla \cdot (\delta I)\right]}{m} \right\} dA = -\delta G \tag{2}$$

We only consider surface diffusion in this work and let the dimensionless group ml_e^2 / M be a small number to ignore evaporation-condensation, where l_e is a representative length, usually the size of the simulation cell or the required resolution in the simulation.

1.2 Axisymmetric Finite Elements

Following Yu and Suo [6], we formulate the axisymmetric finite element. An axisymmetric surface is generated by rotating a plane curve around an axis lying on the same plane. We divide the generating curve into many small straight elements; the surface is then represented by the coordinates of all the nodal points. The coordinates, together with mass displacement $\boldsymbol{I}$ at all the nodal points and mid-points of all elements form generalized coordinates, q_1, q_2,…, q_{n-1}, q_n, where n is total degrees of freedom. The generalized velocities are q_1, q_2,…, q_{n-1}, q_n and the virtual motion of the surface is represented by δq_1, δq_2,…, δq_{n-1}, δq_n. The velocity and virtual motion of any point on the surface can be interpolated by the corresponding values at the nodes. Integrating the Equ (2) element by element, we get a bilinear form in $\dot{q}$ and δq. The right-hand side of Equ (2) is the total free energy change associated with the virtual motion, $\delta \boldsymbol{G} = -\sum f_i \delta q_i$, which allows us to compute the generalized forces $f_1, f_2, \ldots, f_{n-1}, f_n$. Collect the coefficient of δq_i, giving $\sum H_{ij} \dot{q}_j = f_i$. The equation is a set of nonlinear ordinary deferential equations and is solved by using Runge-Kuta method. Assuming the mechanical load is given as displacement controlled, there is no work done by the external load in the surface evolution process. For one element the surface area is $A = \pi(x_1 + x_2)l$, where x_1 and x_2 are the radii at the two nodes of the element. The virtual volume change near to surface is $\delta v = 2\pi r \boldsymbol{s} \delta r_{\mathbf{n}}$. The free energy reduction of

the element is $-\delta G = f_1\delta x_1 + f_2\delta y_1 + f_3\delta x_2 + f_4\delta y_2$. The force components acting on the two nodes due to element surface tension and elastic energy are

$$\begin{bmatrix} f_1 \\ f_2 \\ f_3 \\ f_4 \end{bmatrix} = \pi\gamma \begin{bmatrix} -l + (x_1 + x_2)\cos\theta \\ (x_1 + x_2)\sin\theta \\ -l - (x_1 + x_2)\cos\theta \\ -(x_1 + x_2)\sin\theta \end{bmatrix} + \frac{\pi l w}{3} \begin{bmatrix} -(2x_1 + x_2)\sin\theta \\ (2x_1 + x_2)\cos\theta \\ -(x_1 + 2x_2)\sin\theta \\ (x_1 + 2x_2)\cos\theta \end{bmatrix} \tag{3}$$

where γ is the surface tension and w is the strain energy density of the element.

4. Simulation Results

Considering a fibre under a constant and uniaxial stress σ with a sinusoidal perturbation $R=R_0(1-\varepsilon^2/4+\varepsilon\cos kz)$, where R_0 is the initial radius, ε the perturbation amplitude, $k=2\pi/\lambda$ the wave vector, introduced into the lateral surface of the fibre, we can derive the perturbation growth rate $\varepsilon=\varepsilon(0)e^{t/\tau}$. The characteristic time is

$$\frac{1}{\tau} = \frac{M\gamma}{R_0^4}\omega^2(1-\omega^2 + \frac{(1+\nu)\omega}{2\pi}\Lambda f(\frac{2\pi}{\omega})) \tag{4}$$

$$f(\frac{2\pi}{\omega}) = \frac{(3-2\nu)I_0(\omega) - I_1^2(\omega) - 4(1-\nu)I_0(\omega)I_1(\omega)/\omega}{I_0^2(\omega) - I_1^2(\omega) - 2(1-\nu)I_1^2(\omega)/\omega^2} \tag{5}$$

where $\omega=2\pi R_0/\lambda$, $\Lambda=\sigma^2\lambda/E\gamma$, E and υ are the elastic modules and Possion ratio respectively, and I_0 and I_1 are modified Bessel functions. Fig 1 shows the perturbation growth rate under different uniaxial stresses.

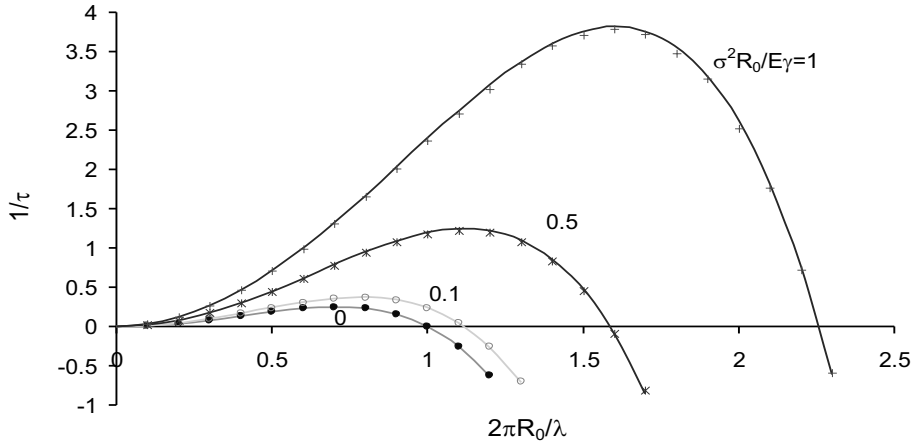

Figure 1. Perturbation growth rate of stressed fibre

From Equ (4), we obtained the stress criteria Λ for the instabilities of the fibre corresponding to different wavelength. For example, $\Lambda_c = 3.1$ when $\lambda = 0.3 \times (2\pi R_0)$. Our simulation shows that the fibre may keep stable (Fig. 2 Λ=2.8); or develop grooves then approach to a steady state shape (Fig. 2 Λ=9.4, 47), or develop cusps and break into droplets (Fig. 2 Λ=53). We may roughly get another threshold between steady state and break of fibre from a serial of simulations. It provides us a possibility to avoid stressed fibre break by controlling its wavelength.

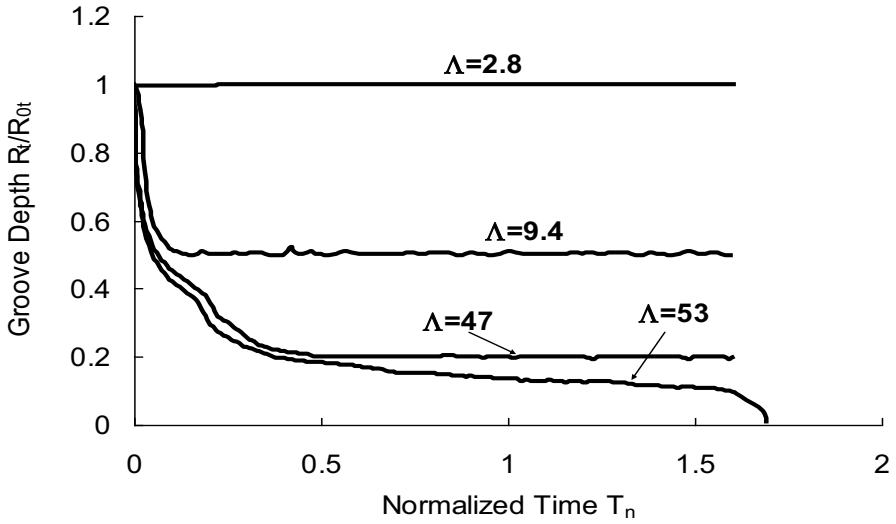

Figure 2. Groove depth grows at different stress level

Acknowledgements

The work is supported by a grant from DOE under contract DE-FG02-06ER46284 with the City University of New York.

References

[1] Lord Rayleigh, "On the Instability of Jets", Proceedings of the London Mathematical Society, **10**, 4 (1878).
[2] F. A. Nichols and W. W. Mullins, "Surface (Interface) and Volume Diffusion Contributions to Morphological Changes Driven by Capillarity:" Trans. AIME **233**, 1840 (1965).
[3] J. Colin, J. Grilhe, and N. Junqua, "Morphological Instabilities of a Stressed Pore Channel", Acta Mater, **45**, 3835 (1997).
[4] Z. Liu and H-H Yu, "A Numerical Study on the Effect of Mobilities and Initial Profile in Thin Film Morphology Evolution", Thin Solid Films, **513**, 391 (2006)
[5] C. Herring "Surface Tension as a Motivation for Sintering", in *The Physics of Powder Metallurgy*, edited by W. E. Kingston (McGraw-Hill, New York, 1951) 143-179.
[6] H-H. Yu and Z. Suo, "An Axisymmetric Model of Pore-grain Boundary Separation", Journal of Mechanics and Physics of Solids, **47**, 1131 (1999)

Nanostructure-Bulk Interfaces Formed by Directed Self-Assembly

Ongi Englander

Department of Mechanical Engineering, FAMU-FSU College of Engineering
2525 Pottsdamer St, Tallahassee, FL 32310 (E-mail: englander@eng.fsu.edu)

ABSTRACT

Self-assembled nanoscale systems offer tremendous advantages in terms of large scale production and manufacturing of nanoscale devices. The premise of the self-assembled process, however, is that nanostructure contact with larger scale components forms in-situ leaving many questions regarding contact attributes and interfacial properties. Developing better understanding of these contact mechanisms is intriguing from a scientific perspective and essential as we pursue these methodologies for device applications. Here we describe a method for self-assembly and direct integration of one-dimensional nanostructures among bulk structures and discuss various system configurations that may result.

1. Introduction

One of the major challenges to the uptake and integration of nanoscale based technologies in applications and devices lies with significant limitations of nanoscale manufacturing capabilities and the inability to effectively and reliably integrate nanoscale building blocks with larger scale systems. This work focuses on integrating 1-D nanostructures. Nanoscale contacts are present in any system or device containing a nanoscale component. Understanding these contacts and their role in nanosystem performance is critical as we design and engineer next generation nanoscale devices. A nanoscale contact forms as a 1-D nanostructure contacts a larger scale component leading to an abruptly changing interface geometry which may take either a *side contact* or an *end contact* configuration. Side contact configurations generally result when a portion of the length of the nanostructure contacts a bulk surface while an end or essentially a point contact configuration is defined as a contact formed when a nanostructure's cross section contacts the bulk. The latter contact is characterized by a limited contact area often defined only by the nanostructure's diameter. Self-assembled mechanisms often yield end contact configurations while top-down processes commonly yield side contacts.

Recent experimental results with side contact configurations conclusively illustrate that electrical contact resistance increases with decreasing contact length [1]. Additionally, extensive modelling and simulation efforts suggest both electrical and thermal transport limitations across abruptly changing interfaces. In the end contact configuration, Hu el al showed that contact electrical resistance increases with decreasing nanowire diameter [2]. Similarly, thermal resistance was shown to increase with decreasing nanowire diameter [3] and as a function of material properties

at the interface [4]. The availability of experimental data with respect to end contact configurations is limited at this time.

2. Experimental Methods

Two-terminal micro-nano systems were fabricated using localized and directed self-assembly methods described elsewhere [5, 6, 7]. The technique allows site-specific catalyst-assisted chemical vapor deposition (CVD) techniques for 1-D nanostructure synthesis to be carried out on suspended MEMS silicon heaters. By applying a localized electric-field during the synthesis process, the directed self-assembly of either silicon nanowires or carbon nanotubes has been demonstrated. This method is unique as it eliminates post-synthesis nanostructure organization and contact formation. The advantages of confining the thermal environment, as utilized in this approach, include the ability to maintain a room temperature environment on-chip near devices and materials sensitive to high temperatures, the ability to readily integrate in-situ monitoring, control and characterization tools, and strong compatibility with standard microfabrication techniques. The resulting two-terminal configuration can be realized in a horizontal or vertical configuration (Fig. 1) and suspended nanostructure-based systems may serve sensing, resonator and other NEMS applications.

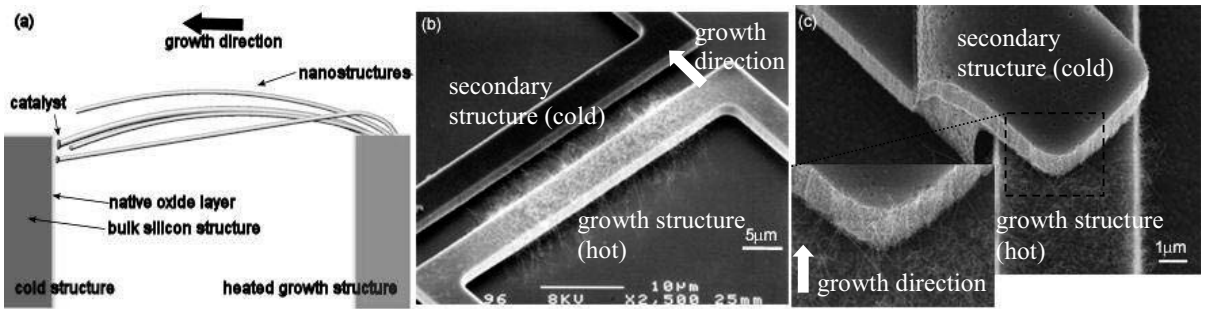

Figure 1. Localized self-assembled architecture. (a) A schematic of process (b) horizontal self-assembly (c) vertical self-assembly.

3. Results

The typical experimental setup yields suspended silicon nanowires or multiwalled carbon nanotubes connected to highly doped silicon structures in a doubly clamped nanostructure configuration. The resulting self-assembled systems present interesting device architectures. A schematic of a typically realized system is seen in Fig. 1a. The growth begins on the top surface of the heated structure as the catalyst required for the reaction is only applied to the top surface using directional evaporation processes. The second contact most often forms to the sidewall of the secondary cold structure (Fig. 2). The contact to the secondary structure is determined by the location of the catalyst and the strength of the applied electric-field. The synthesis reaction continues as long as the local temperature is above the eutectic temperature of the metallic catalyst-vapor phase reactant combination. Under tip growth conditions, as in the case of silicon nanowires, the catalyst is at the free end of the nanowire and hence upon contact with a bulk room temperature structure, we expect a temperature drop and thus the termination of the

synthesis process. In this case, the cold structure serves as the secondary contact location and termination point for the reaction. The liquid alloy is believed to spread upon contact [8]. The termination of the reaction becomes more complex with base growth conditions which carbon nanotubes may exhibit. In this case, the catalyst remains on the surface of the hot growth structure and hence tip contact to the secondary structure may not terminate the reaction if sufficient heating is available at the base. In fact, carbon nanotubes 'walking' along the sidewalls of the secondary structure have been noted. Another possible configuration occurs when the contact to the cold structure forms along the top surface. As discussed in the following section, in this case, contact geometry more closely resembles a side contact configuration (Fig. 2c).

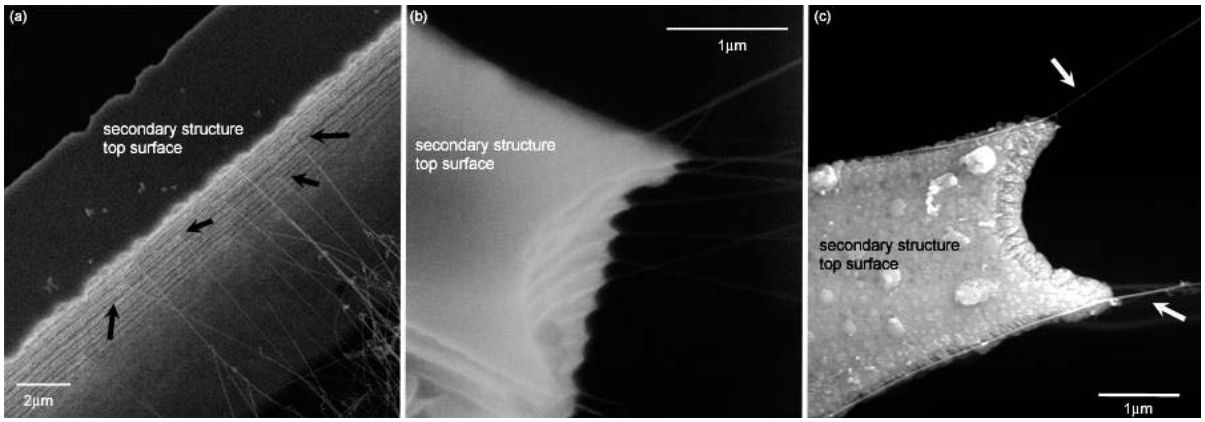

Figure 2. Contact formation of self-assembled 1-D nanostructures to cold secondary structures. (a) Contact formation and process termination along sidewall (b) contact formation well below top surface (c) contact formation and continued growth (beyond initial contact) in the vicinity of the top surface of the cold bulk structure.

4. Discussion

The self-assembly process results in system architectures that are asymmetric in nature. First, the approach yields only an initial contact to the bulk that is annealed throughout the duration of the synthesis process. While on the other hand, the secondary contact in a tip growth configuration forms instantaneously at room temperature. Since annealing is known to effectively reduce contact resistance, improved contact properties at one end may result. Furthermore, the reaction catalyst is present along the interface at either the initial or secondary contact but not both contacts. Location and type of catalyst may affect system properties. Contact formation at the secondary structure which is not directly mitigated by the catalyst presents yet another configuration. Either base growth behavior or weak electric-fields may yield this result. The trajectory of the nanostructure during growth is affected by thermal vibrations and the applied electric-field. Contacts to the top surface most often occur when weak or no electric-field is applied. Contacts to the top surface may result in an end contact configuration but more often resemble a side contact configuration. Although the contact area is increased in this scenario the contact area is limited to roughly a tangent line contact and a weaker mechanical bond is expected. In the vertical self-assembly configuration, a mix of end contacts and point contacts along the length of the nanostructure are seen (Fig. 1c). Analysis of the relative bond strengths

among the different contacts indicates that the initial contact is mechanically more robust than the secondary contact. This qualitative analysis is based on the force required to break the bond and the response of the each contact to surface tension forces inflicted in an aqueous environment [6]. Characterization and modelling efforts of the self-assembled systems must consider additional system attributes. A native oxide layer is present along all bulk silicon surfaces prior to catalyst evaporation and synthesis. The role of the native oxide layer on the interface properties as well as diffusion of the catalyst at the contact is unknown. This could be of importance particularly in light of modelling work which suggests that the mass and stiffness ratios of the materials coming together at the contact do affect phonon transmission across the interface [4]. Additionally, the exact contact area is difficult to determine and is believed to be slightly smaller than the measured diameter. The rough sidewalls of the bulk structures, as seen in Fig. 2 (due to the microfabrication (etching) processes), could further contribute to a reduced contact area. Finally, mechanical strains in the nanostructures may affect system behavior.

5. Conclusions

Novel self-assembled nano-micro system architectures are described. Understanding these self-assembled architectures and the properties of the resulting systems is essential as we seek to utilize this approach in the fabrication of nanoscale systems and devices. Furthermore, effectively controlling the various potential configurations is a prerequisite for effectively utilizing this assembly and integration approach.

References

[1] C. Lan, D. N. Zakharov, and R. G. Reifenberger, "Determining the optimal contact length for a metal/multiwalled carbon nanotube interconnect", Applied Physics Letters, **92**, 213112 (2008).
[2] J. Hu, Y. Liu, C. Z. Ning, R. Dutton, and S. M. Kang, "Fringing field effects on electrical resistivity of semiconductor nanowire-metal contacts", Applied Physics Letters, **92**, 083503 (2008).
[3] W. Zhang, N. Mingo, and T. S. Fisher, "Simulation of phonon transport across a non-polar nanowire junction using an atomistic Green's function method", Physical Review B, **76**, 195429 (2007).
[4] M. A. Panzer and K. E. Goodson, "Thermal resistance between low-dimensional nanostructures and semi-infinite media", Journal of Applied Physics, **103**, 094301 (2008).
[5] O. Englander, D. Christensen, and L. Lin, "Local synthesis of silicon nanowires and carbon nanotubes on microbridges", Applied Physics Letters, **82**, 4797 (2003).
[6] O. Englander, D. Christensen, J. Kim, and L. W. Lin, "Post-processing techniques for locally self-assembled silicon nanowires", Sensors and Actuators a-Physical, **135**, 10 (2007).
[7] O. Englander, D. Christensen, J. Kim, L. W. Lin, and S. J. S. Morris, "Electric-field assisted growth and self-assembly of intrinsic silicon nanowires", Nano Letters, **5**, 705 (2005).
[8] S. Sharma, T. I. Kamins, M. S. Islam, R. S. Williams, and A. F. Marshall, "Structural characteristics and connection mechanism of gold-catalyzed bridging silicon nanowires", Journal of Crystal Growth, **280**, 562 (2005).

Atomistic Modeling of Screw Dislocations in BCC iron: Inter-atomic Potentials and Boundary Conditions

David Stewart[1], Yuri Osetsky[1], Roger Stoller[1], Stanislav Golubov[1], Byeong-Joo Lee[2], Young-Min Kim[2]

[1]Oak Ridge National Laboratory, Oak Ridge, Tennessee, USA
(E-mails: stewartdm@ornl.gov, osetskiyyn@ornl.gov, stollerre@ornl.gov, golubovsi@ornl.gov)
[2]Pohang University of Science and Technology
(E-mails: calphad@postech.ac.kr, ymfrog@postech.ac.kr)

ABSTRACT

It is necessary to be able to use molecular dynamics to model screw dislocations in iron. Screw dislocations modeled using the Ackland embedded atom method (EAM) potential [1] show an unrealistic degenerate structure [3]. With the Mendelev EAM potential [2] they show a non-degenerate structure, but their behavior is not entirely satisfactory [3,4]. We investigate the modified embedded atom (MEAM) [5] and bond order potential (BOP) [6] methods. Screw dislocations in BCC materials are sensitive to non-glide stress components, and therefore boundary conditions can have a large effect on their properties [4]. We investigate the effect of periodic and Green's function boundary conditions.

[1] Ackland et al, Phil. Mag. 75, 713 (1997)
[2] Mendelev et al, Philos. Mag. 83 3977 (2003)
[3] Domain et al, Phys. Rev. Lett. 95, 215506 (2005)
[4] Chaussidon et al, Acta Mater 54, 3407 (2006)
[5] Lee et al, Phys. Rev. B. 64, 184102 (2001)
[6] Müller et al, J. Phys.: Condens. Matter 19, 326220 (2007)

Dynamic Recrystallization Simulation by Phase - Field Method

Tomohiro Takaki[1], Yousuke Hisakuni[2], Akinori Yamanaka[3], Yoshihiro Tomita[2]

[1]Graduate School of Science and Technology, Kyoto Institute of Technology, Matsugasaki, Sakyo, Kyoto 606-8585, Japan, takaki@kit.ac.jp; [2]Graduate School of Engineering, Kobe University, 1-1, Rokkodai, Nada, Kobe 657-8501, Japan; [3]Graduate School of Science and Technology, Kobe University, 1-1, Rokkodai, Nada, Kobe 657-8501, Japan.

ABSTRACT

We developed a novel numerical scheme, which can take topological volume constant deformation into consideration, using multi-phase-field dynamic recrystallization (MPF-DRX) model that we have proposed. In this scheme, the size of finite difference grid is simply changed so as to keep the volume constant. Throughout a series of numerical simulations, we investigated macroscopic stress-strain curves, variations of average grain size, variations of DRX fraction and microstructure evolutions during DRX and evaluated the effects of topological deformation introduced in this study on their performances.

1. Introduction

Dynamic recrystallization (DRX) occurs during hot working of metals with low to medium SFE. The macroscopic stress-strain relation during DRX exhibits characteristic curves depending on the microstructure. Therefore, the phenomena caused during DRX are multi-scale problem and it is essential for hot working process design to develop a numerical model which can simulate the macroscopic behaviors depending on the microstructure variations. Ding and Guo [1] have proposed DRX model that couples cellular automaton (CA) method and fundamental metallurgical principles of DRX. Their model has been developed by some groups [2]. The authors have proposed the MPF-DRX method [3] by employing phase-field (PF) method instead of CA method and pointed out that CA method could not simulate DRX accurately. Furthermore, Xiao et al. [4] have developed the topology deformation technique for DRX and concluded that the change of grain topology results in that the kinetics of DRX becomes faster and final average grain size becomes finer than those simulated by the conventional CA method [1, 2].
In this study, we develop the topology deformation scheme for MPF-DRX model. Throughout a series of numerical simulations, we investigated macroscopic stress-strain curves, variations of average grain size, variations of DRX fraction and microstructure evolutions during DRX and evaluated the effects of topological deformation introduced in this study on their performances.

2. MPF-DRX model

In MPF-DRX model [3], the grain growth driven by stored energy is simulated by the MPF method and the dislocation density evolution due to plastic deformation and dynamic recovery

(DRV) is expressed by the Kocks-Meching (KM) model. And, a macroscopic stress-strain curve is obtained from the Bailey-Hirsch relation using the average dislocation density.
The growth of grain i is expressed by the equation

$$\dot{\phi}_i = -\sum_{j=1}^{n} \frac{2M_{ij}^{\phi}}{n} \left[\sum_{k=1}^{n} \left\{ \left(W_{ik} - W_{jk} \right) \phi_k + \frac{1}{2} \left(a_{ik}^2 - a_{jk}^2 \right) \nabla^2 \phi_k \right\} - \frac{8}{\pi} \sqrt{\phi_i \phi_j} \Delta E_{ij} \right], \tag{1}$$

where ϕ_i is phase field which takes 1 inside grain i and 0 inside the other grains. a_{ij}, W_{ij} and M^{ϕ}_{ij} are the gradient coefficient, the height of the energy barrier and the phase field mobility, respectively, and can be related to the grain boundary thickness δ, grain boundary energy γ and grain boundary mobility M. ΔE_{ij} is the driving force calculated as the difference of stored energies between grain i and grain j.
The accumulation of dislocations due to plastic deformation and DRV is expressed by the KM model as a relationship between dislocation density ρ and true strain ε,

$$\frac{d\rho}{d\varepsilon} = k_1 \sqrt{\rho} - k_2 \rho \,. \tag{2}$$

Here, the first term of the right-hand side expresses the work hardening, where k_1 is a constant that represents hardening. The second term is the DRV term, where k_2 is a function of temperature T and strain rate $\dot{\varepsilon}$. The macroscopic stress is related to the average dislocation density ρ_{ave} as follows:

$$\sigma = \alpha \mu b \sqrt{\rho_{ave}} \,, \tag{3}$$

where α is a dislocation interaction coefficient of approximately 0.5, μ is the shear modulus and b is the magnitude of the Burgers vector. From eqs. (2) and (3), a macroscopic stress-strain curve can be determined.

4. Topological Constant Volume Deformation Scheme and Computational Conditions

The topological constant volume deformation during DRX is simulated by simply changing finite difference grid size. In case of compression simulation, the grid size in x-direction at true strain ε (positive in compression) is set to be $\Delta x = \{2\text{-}\exp(\text{-}\varepsilon)\}\Delta x_{ini}$ and that in y-direction is $\Delta y = \Delta x_{ini}\Delta y_{ini}/\Delta x$, where Δx_{ini} and Δy_{ini} are the initial grid sizes in x- and y-directions respectively.
We use the following three computational models:
Model A (712.5x740.0 μm, 1425x1480 lattices, $\Delta x = \Delta y = 0.5$ μm constant)
Model B (713.5x741.0 μm, 1855x1140 lattices, $\Delta x = 0.5/1.3$ μm and $\Delta y = 0.5$x1.3 μm constant)
Model C (713.5x741.0 μm, 1855x1140 lattices, $\Delta x_{ini} = 0.5/1.3$ μm and $\Delta y_{ini} = 0.5$x1.3 μm with topological deformation scheme). Almost all computational conditions are identical with those used in Ref. [3] except for $\delta = 7$ times of maximum lattice size or 0.5x1.3 μm. Furthermore, we employ two kinds of interface mobility $M = M_{ori}$ and $M = M_{ori}/5$, where M_{ori} is the mobility used in Ref. [3]. Initial grain shape is set to the regular hexagon and its average grain diameter is set to be $D_0 = 150$ μm.

5. Numerical Results and Discussion

Figure 1 shows the microstructure evolutions for Models B-1, B-2 and C-2, where -1 means $M = M_{ori}$ and -2 means $M = M_{ori}/5$. The grey grains correspond to initial grains. We can observe the typical necklace structures at the beginning of DRX. From Fig. 1(c) or Model C-2, it is

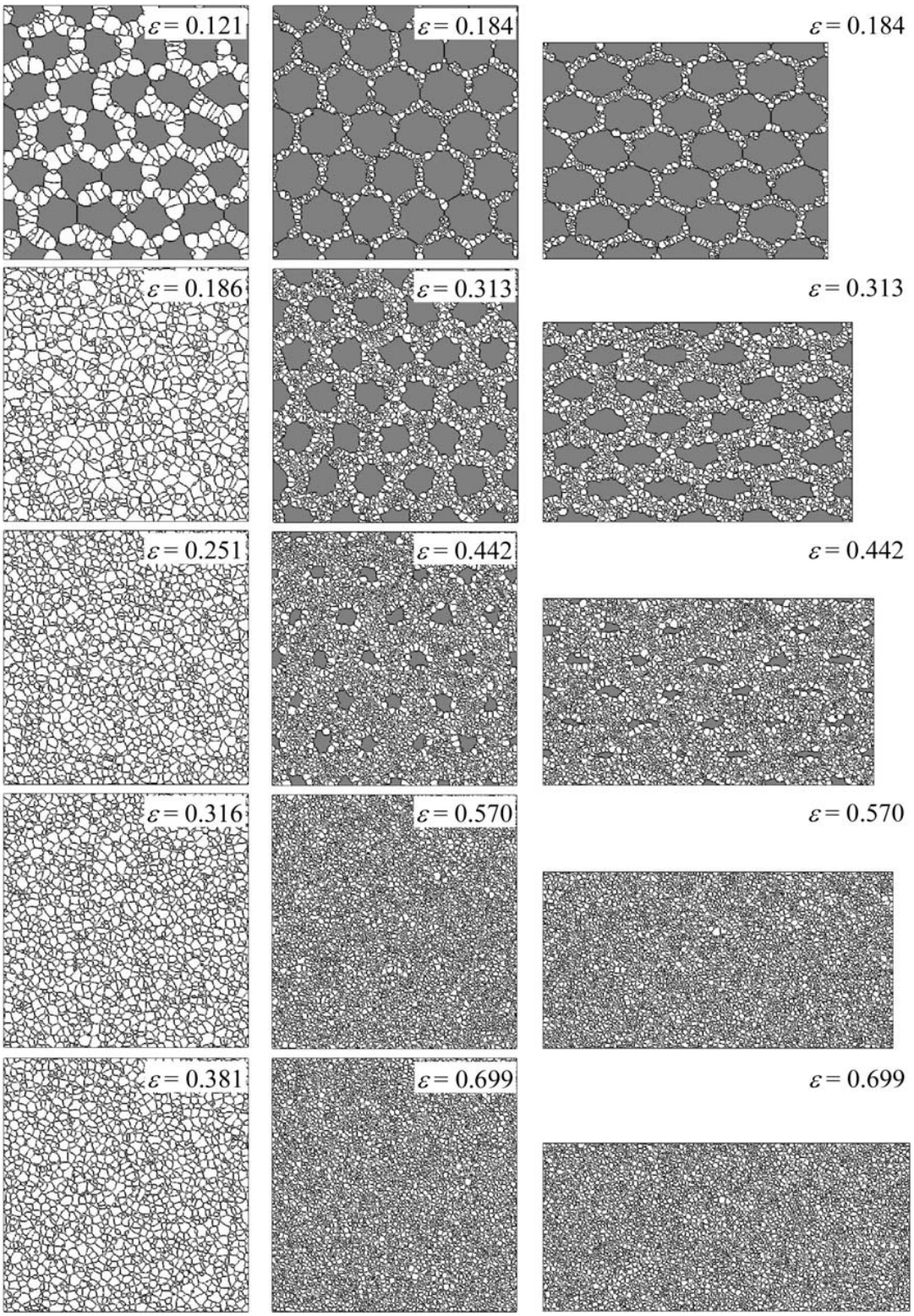

(a) Model B-1 (b) Model B-2 (c) Model C-2

Figure 1. DRX microstructure evolutions.

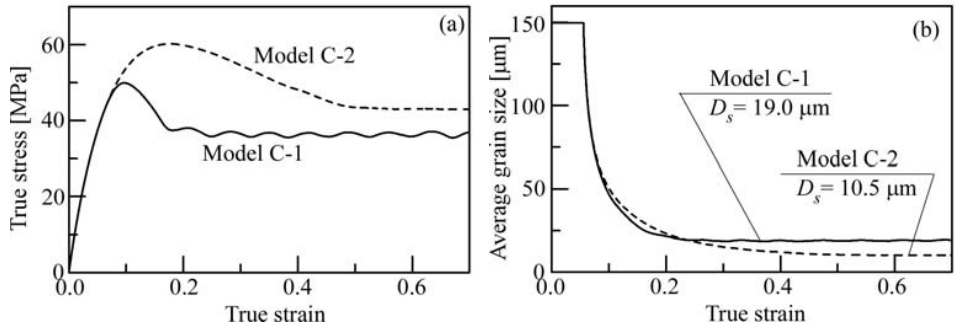

Figure 2. (a) Stress – strain curves and (b) variations in average grain size for Model C.

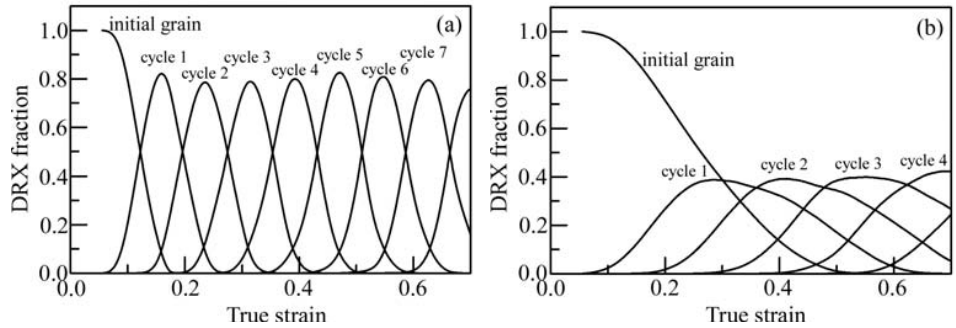

Figure 3. Variations in DRX fractions for each DRX cycle for (a) Model C-1 and (b) Model C-2.

confirmed that the topological constant volume deformation can be simulated. To our surprise, however, the macroscopic stress-strain curves, variations of average grain size and variations in DRX fractions among Models A, B and C agree perfectly. Therefore, in Figs. 2 and 3, the results for only Model C are shown. This result means that the number of nucleation sites is constant even if we consider the topological deformation and denies the results of Ref. [4].

From Fig. 2(a), the single peak curves are observed for both mobility. These single peak curves are characterized by the overlap of DRX friction of some DRX cycle, as shown in Fig. 3. Since the number of DRX cycles that overlap is larger for Model C-2 than C-1, the strain from stress maximum point to steady state stress is larger for Model C-2. From these results, using the concept of DRX cycle, it is concluded that the macroscopic stress-strain relation can be characterized.

References

[1] R. Ding and Z. X. Guo, "Coupled Quantitative Simulation of Microstructural Evolution and Plastic Flow during Dynamic Recrystallization", Acta Mater., **49**, 3163 (2001).

[2] G. Kugler and R. Turk, "Modeling the Dynamic Recrystallization under Multi-Stage Hot Deformation", Acta Mater., **52**, 4659 (2004).

[3] T. Takaki, T. Hirouchi, Y. Hisakuni, A. Yamanaka and Y. Tomita, "Multi-Phase-Field Model to Simulate Microstructure Evolutions during Dynamic Recrystallization", Mater. Trans., **49**, (2008), *in press*.

[4] N. Xiao, C. Zheng, D. Li and Y. Li, "A Simulation of Dynamic Recrystallization by Coupling a Cellular Automaton Method with a Topology Deformation Technique", Comp. Mater. Sci., **41**, 366 (2008).

Investigation of ζ Hydride Precipitation in Zirconium

Ludovic Thuinet and Alexandre Legris

Laboratoire de Métallurgie Physique et Génie des Matériaux, USTL, CNRS UMR 8517, Bât. C6, F-59655 Villeneuve d'Ascq Cedex, France
(E-mails: Ludovic.Thuinet@univ-lille1.fr, Alexandre.Legris@univ-lille1.fr)

ABSTRACT

Zirconium alloys, used as cladding materials in pressurized water nuclear reactors, are corroded by the primary water. As a consequence, hydrogen is absorbed and can precipitate degrading the mechanical properties. Recent experimental investigations revealed the formation of a new hydride phase called ζ fully coherent with the matrix (hcp αZr) during the first stages of the precipitation. ζ belongs to the trigonal crystallographic system which implies a symmetry break with respect to the hexagonal symmetry of the αZr matrix. ζ hydrides are needle-shaped and, when no external stress is applied on the material, are elongated in the basal plane along the dense directions of the matrix (three different variants). Moreover, the application of an external stress promotes the growth of only one variant. Due to the coherent nature of the interfaces between ζ hydrides and the matrix, a particular effort has been made in this work in order to calculate properly the elastic energy associated to the precipitation. The aim is to numerically address the influence of symmetry break and elastic heterogeneity on precipitation morphology and variant selection under an applied stress.

Mesoscopic TDGL Model for Microstructural Evolution of $L1_0$ Type Ordering

Ryuichiro Oguma[1], Syo Matsumura[2], and Tetsuo Eguchi[1]

[1] Department of Applied Physics, Fukuoka University Fukuoka 814-0180, Japan, oguma@fukuoka-u.ac.jp;
[2] Department of Applied Quantum Physics and Nuclear Engineering, Kyushu University, Fukuoka 819-0395, Japan

ABSTRACT

A mesoscopic time-dependent Ginzburg-Landau (TDGL) model has been presented for $L1_0$ type ordering in a binary alloy, taking account of the crystal symmetry. Kinetic equations for time-evolution of the order parameters and the concentration are derived from the Ginzburg-Landau type potential consisting of the mean-field free energy density and the interfacial energy terms. Three-dimensional simulation of the kinetic equations was performed to simulate time-evolution of off-phase domain structures in real alloy systems. The microstructures obtained are compared with the experimental results of observation by transmission electron microscopy (TEM).

1. Introduction

The $L1_0$ type ordered structure is sometimes formed in *fcc*-based AB alloys such as CuAu. In the $L1_0$ structure, A atoms occupy corner-sites and one kind of face-centered sites preferentially, while B atoms are on the other two kinds of face-centered sites as shown in Fig. 1(a). The structure is characterized by alternating stacking of two different (100) planes. Therefore three orientational variants can be formed depending on which of <100> directions corresponds to *c*-axis and two translational variants are possible for each of them; six distinct crystallographic variants exist in this type of order. The $L1_0$ type ordering process from an *fcc* disordered state ($A1$) involves cubic-tetragonal transition. This structural change causes lattice mismatch between the parent cubic and the product tetragonal phases as well as between different orientation variants of the product phase. It has been observed in the cubic-tetragonal transition of some alloys that tweed structure at first appears and then it continuously transforms into twinning structure with alternate arrays of plates of two different orientational variants [1]. The present authors have developed a TDGL model on a continuous medium for ordering process of $L1_0$ type in binary alloys. The authors apply the formulation to simulate time-evolution of boundary structures with the characteristic anisotropy observed in TEM images.

2. Formulation

The fundamental *fcc* lattice is divided into four simple cubic sublattices, two of which are

preferentially occupied by A atoms in the $L1_0$ structure (see Fig. 1(b)). Four sites are grouped

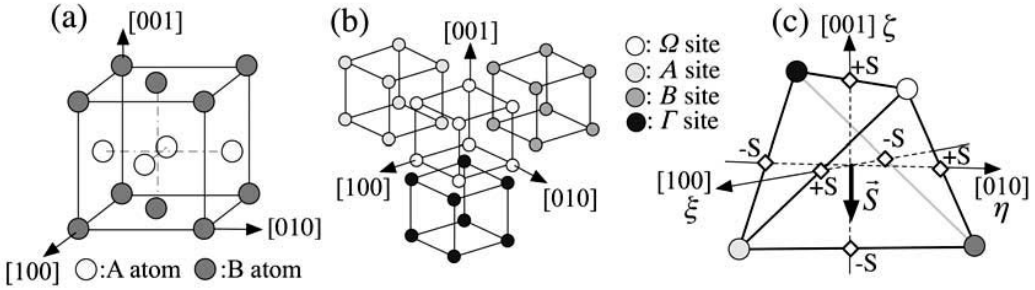

Figure 1. (a) Unite cell of $L1_0$ structure. (b) The crystal lattice of $L1_0$ structure is decomposed into four simple cubic sublattices Ω, A, B and Γ (c) Vector $\vec{s}(\xi,\eta,\zeta)$ in the Euclidian space spanned with the order parameters. Midpoints of line segments are indicated by open rhombuses.

TABLE 1. Atomic occupation probabilities for each site.

Site	A atoms	B atoms
Ω	$\frac{1}{2}(1-\varepsilon-\xi-\eta-\zeta)$	$\frac{1}{2}(1+\varepsilon+\xi+\eta+\zeta)$
A	$\frac{1}{2}(1-\varepsilon-\xi+\eta+\zeta)$	$\frac{1}{2}(1+\varepsilon+\xi-\eta-\zeta)$
B	$\frac{1}{2}(1-\varepsilon+\xi-\eta+\zeta)$	$\frac{1}{2}(1+\varepsilon-\xi+\eta-\zeta)$
Γ	$\frac{1}{2}(1-\varepsilon+\xi+\eta-\zeta)$	$\frac{1}{2}(1+\varepsilon-\xi-\eta+\zeta)$

into two of equivalent sites to treat six types of variants equivalently. Atomic occupation probabilities for each site of $A_{2(1-\varepsilon)}B_{2(1+\varepsilon)}$ alloy are defined with three order parameters ξ, η and ζ, and a composition parameter ε, as represented in Table 1. Then the values of (ξ,η,ζ) for the variants are as follows; $(\pm S,0,0)$, $(0,\pm S,0)$ and $(0,0,\pm S)$, where S is the degree of order. If the state of order of atomic arrangement is represented by a point in the three-dimensional Euclidean space spanned by the three order parameters, the six equivalent variants are defined by the six tips of a regular octahedron centered on the origin for the disordered state. The axes of ξ, η and ζ can be parallel to [100], [010] and [001], respectively and pass through midpoints of line segments between two of the corner sites of the sublattices (See Fig. 1(c)). Since the six midpoints are also related to the tips of the regular octahedron, vector $\vec{s}(\xi,\eta,\zeta)$ elongates from the origin in the direction to one of the six points as ordering proceeds.These order parameters are measurable and dark-field TEM images taken with 100, 010 and 110 Bragg reflections show spatial variations of ξ^2, η^2 and ζ^2, respectively. In TDGL formulation thermodynamic potential Φ is given in a form of

$$\Phi\{\xi,\eta,\zeta,\varepsilon;T\} = \int\left\{F(\xi,\eta,\zeta,\varepsilon;T) + G\left(\vec{\nabla}\xi,\vec{\nabla}\eta,\vec{\nabla}\zeta,\vec{\nabla}\varepsilon;T\right)\right\}d\vec{r}\,. \tag{1}$$

Here the first term F is a free energy density and the second term G means the interface energy density. We introduce the free energy density in such a Landau expansion as,

$$F(\xi,\eta,\zeta,\varepsilon;T) = A_0\left\{\frac{1}{2}b(\varepsilon-\varepsilon_0)^2 + \frac{1}{2}S_e{}^3\sigma\left(\xi^2+\eta^2+\zeta^2\right) - S_e(S_e+\sigma)\left(\xi^4+\eta^4+\zeta^4\right) + \frac{1}{6}\left(\xi^2+\eta^2+\zeta^2\right)^3\right\} \tag{2}$$

where A_0 and b are positive parameters depending on temperature T. When $S_e(\varepsilon,T)^3\sigma(\varepsilon,T)<0$ and $S_e(\varepsilon,T)(S_e(\varepsilon,T)+\sigma(\varepsilon,T))>0$, the function f has its maximal value at the origin and the minimal value at the points corresponding to the six variants, $\vec{s}(\xi,\eta,\zeta)=(\pm S_e,0,0)$, $(0,\pm S_e,0)$, $(0,0,\pm S_e)$. The interface energy density is given in a gradient square approximation [2]. Cubic symmetry should be satisfied in this energy density, because interfaces formed between two of six variants are equivalent to each other;

$$G\left(\vec{\nabla}\xi,\vec{\nabla}\eta,\vec{\nabla}\zeta,\vec{\nabla}\varepsilon;T\right)=\frac{1}{2}\mu Q^2+\frac{1}{2}\nu\sum_{i=1}^{3}P_i^{\,2}+\frac{1}{2}\gamma\sum_{i=1}^{3}V_i^{\,2}+\frac{1}{2}\omega\sum_{i=1}^{3}W_i^{\,2}+\frac{1}{2}\chi\left(\vec{\nabla}\varepsilon\right)^2, \tag{4}$$

where

$$Q\equiv\sum_{i=1}^{3}\frac{\partial\rho_i}{\partial u_i},\ P_i\equiv\frac{\partial\rho_k}{\partial u_j}-\frac{\partial\rho_j}{\partial u_k},\ V_i\equiv\frac{2}{3}\left(2\frac{\partial\rho_i}{\partial u_i}-\frac{\partial\rho_j}{\partial u_j}-\frac{\partial\rho_k}{\partial u_k}\right),\ W_i\equiv\frac{\partial\rho_k}{\partial u_j}+\frac{\partial\rho_j}{\partial u_k}\quad i,j,k=1,2,3 \text{ cyclic permutation.} \tag{5}$$

Here $(\rho_1,\rho_2,\rho_3)=(\xi,\eta,\zeta)$ and $(u_1,u_2,u_3)=(x,y,z)$. Parameters $\mu(T)$, $\nu(T)$, $\gamma(T)$, $\omega(T)$ and $\chi(T)$ are positive, and the directions of ξ, η and ζ agree with those of x, y and z, respectively. Tetragonal symmetry of the interfaces is satisfied when the vector $\vec{s}(\xi,\eta,\zeta)$ lengthens towards one of the tips of the regular octahedron as illustrated in Fig. 1(c). TDGL kinetic equations for ξ, η, ζ and ε are obtained from the thermodynamic potential Φ. Thus

$$\begin{aligned}\frac{\partial\rho_i}{\partial t}&=-L\frac{\delta\Phi}{\delta\rho_i}\\&=-L\left\{S_e^{\,3}\sigma\rho_i-S_e\left(S_e+\sigma\right)\rho_i^{\,3}+\rho_i\left(\rho_i^{\,2}+\rho_j^{\,2}+\rho_k^{\,2}\right)^2\right\}+Ll\frac{\partial^2\rho_i}{\partial u_i^{\,2}}+Lm\left(\frac{\partial^2\rho_i}{\partial u_j^{\,2}}+\frac{\partial^2\rho_i}{\partial u_k^{\,2}}\right)+Ln\left(\frac{\partial^2\rho_j}{\partial u_i\partial u_j}+\frac{\partial^2\rho_k}{\partial u_k\partial u_i}\right)\end{aligned}$$

$i,j,k=1,2,3$ cyclic permutation, (6)

$$\frac{\partial\varepsilon}{\partial t}=M\nabla^2\frac{\delta\Phi}{\delta\varepsilon}=M\left\{\nabla^2\left\{a\varepsilon+\frac{1}{2}\frac{\partial S_e^{\,3}\sigma}{\partial\varepsilon}\left(\xi^2+\eta^2+\zeta^2\right)-\frac{\partial S_e\left(S_e+\sigma\right)}{\partial\varepsilon}\left(\xi^4+\eta^4+\zeta^4\right)\right\}-\chi\nabla^4\varepsilon\right\}. \tag{7}$$

Here $L(T)$ and $M(T)$ are reaction constants and $l=\mu+\frac{4}{3}\gamma$, $m=\nu+\omega$, $n=\mu-\nu-\frac{2}{3}\gamma+\omega$. The evaluated energy densities of {110} twin boundaries are obtained from eqns (4) and (5), and ecorrespond to $G_1\sim\mu+\frac{1}{3}\gamma+\omega$ or $G_2\sim\nu+\gamma$. We thus assumed that the ratio of G_1 to G_2, l and m is small in the simulation so that the interfaces parallel to {110} are preferentially formed.

2. Simulation and Results

The simulation of $A1$-$L1_0$ transition at stoichiometric composition ε=0 was performed on a three-dimensional cubic grid of 120x120x120 mesh with periodic boundary conditions. A result of the simulation is represented in Fig. 2(a,c). Here the values of ξ^2, η^2 and ζ^2 in ten layers of computational grids were integrated along x-direction, and were plotted in two-dimensionally projected views. Three types of representations show similar tweed patterns with traces almost parallel to <110> directions at 2.2 k steps, indicating coexistence of variants whose c-axis lies on

one of the three <100> directions. The analogous tweed pattern is observed in the dark-field TEM image of a $Cu_{50}Au_{40}Pd_{10}$ alloy taken by Matsumura et al. (See Fig. 2(b)) [1]. Here most of Au and Pd atoms can be considered to be stacked in the same {100} plane in the alloy system [3]. The authors demonstrated that three *c*-axes along the <100> directions are preferred equivalently. At the 20 k steps of the simulation, variants with *c*-axis alien to [010] and [001] are found predominantly, and twin boundaries along one of the <011> directions are formed between the variants, as shown in Fig. 2(c). The comparable TEM image by Matsumura et al. is presented in Fig. 2(d) [1]. The authors showed clearly that the dark and bright bands correspond to twined $L1_0$ plates of the [010] and [001] variants with {022} habit planes.

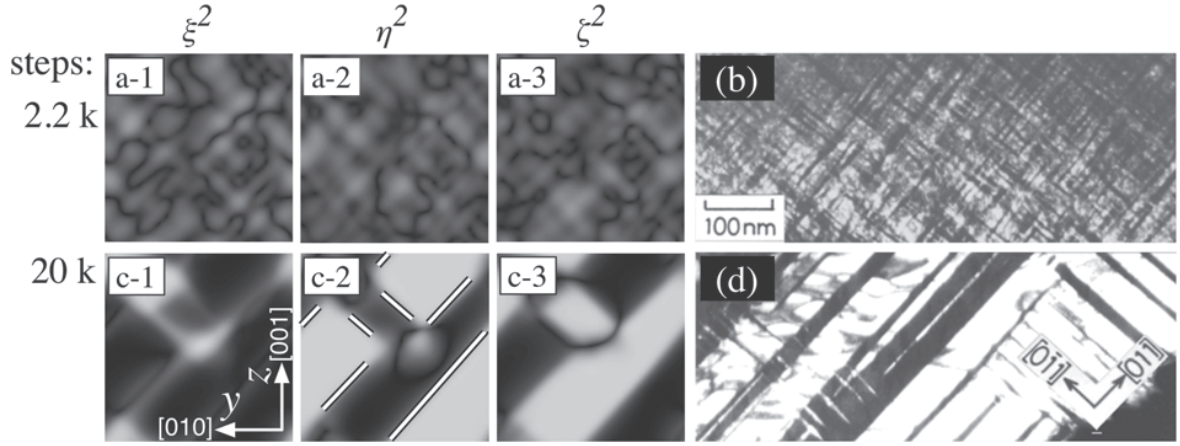

Figure 2. (a,c) Representations of ξ^2, η^2 and ζ^2 obtained by simulation. The gray level varies from dark to bright with an increase in its value. Double lines indicate twin boundaries between variants with *c*-axis alien to [010] and [001] directions in (c-2). (b,d) 010 dark-field TEM images of CuAuPd alloy annealed at 573 K for 1.2 ks (b) and 86.4 ks (d) [2]. The TEM images correspond to η^2 representations as described in section 2.

3. Conclusions

In the present study, we have formulated coupled TDGL equations for $L1_0$ type ordering, taking account of the crystal symmetry. Time evolutions of the derived TDGL equations were obtained by three-dimensional simulations, and explain well characteristic features in boundary structures of $L1_0$, which have been observed in dark-field TEM images.

References

[1] S. Matsumura, T. Furuse, Y. Sasano, and K. Oki, "Twin Structures of $L1_0$ Ordered Phase in CuAuPd Alloys" in *Solid-Solid Phase Transformations*, edited by W. C. Johnson et al. (The Minerals, Metals & Materials Society, Warrendale, 1994), pp. 485-490.
[2] J. W. Cahn and E. J. Hilliard, "Free Energy of a Nonuniform System. I. Interfacial Free energy", Journal of Chemical Physics. **28**, 258 (1959).
[3] S. Matsumura, T. Morimura and K. Oki, "An Analytical Electron Diffraction Technique for the Determination of Long-Range Order Parameters in Multi-Component Ordered Alloys", Materials Transactions, Japan Institute of Metals, **32**, 905 (1991).

Review of Nanomaterial Generation From Vapor Phase

Michael P. Anisimov

Institute of Chemical Kinetics and Combustion, Siberian Division of the Russian Academy of Sciences. 3 Institutskaja Ave., 630090 Novosibirsk, Russia
(E-mail: anisimovmp@mail.ru)

ABSTRACT

Computer modelling of nanoparticle generation has a considerable progress now. Nanoparticle generation is governing by nucleation theory. Nucleation kinetics itself is under careful investigation for many centuries. The nucleation theory which is called the Classical Nucleation Theory was completed at 1940th. The nowadays theory and experiment for vapour-gas nucleation illustrates up to 10 decimal orders deviation from theory. It induces to use the various semiempirical correlations. From physical point of view one can guess that low critical embryo size can raise the internal critical embryo pressure. That leads the carrier gas solubility growth in the critical cluster and problem turns to binary, i.e. vapor-gas system nucleation. From the other hand the data inconsistencies for different devises are a strongest reason for measuring system development. Multiple inconsistencies initiate speculation that the present nucleation vapour-gas experiments have uncontrollable parameter. Seemingly a gas-vapor nucleation consideration as binary system is the way to solve the problem of data inconsistencie. Review of the experimental techniques and principles of nanosize particle generation is presented. It is concluded that an introduction of nucleation standard(s) is an actual problem. Success in the nucleation standard development and its incorporation to the nucleation research practice is the key problem for nucleation experiments of the present time. The dipper understanding of the carrier-gas effects has chance to clarify nature of inconsistencies for the different experimental data sets. There is a hope that consistency of different origion data for all used methods will be achieved in the nearest time.

1. Introduction

Computer modeling of nanoparticle generation from vapor phase is based on Nucleation Theory (NT) using. Computer design of the nucleation rate surfaces over diagram of phase equilibria is a challenging way to raise a reliability of nanomaterial generation prediction. An idea background is formulated in article [1], where the equilibria lines ate used as a zero nucleation rates for critical embryo generation. It is supposed that the experimentally measured data set of the linearized nucleation rate surface slopes. First computer algorithm for that idea is realized in article [2]. The nanoparticle generation is under careful investigation for many centuries. The actual up to now book by Seinfeld and Pandis [3] summarises the research advantages for that problem. Nucleation description which is called the Classical Nucleation Theory was completed at 1940th [4]. The vapour-gas nucleation results illustrate up to several decimal orders deviation

from theory. The empirical nucleation rates show internal inconsistencies for the different experimental data sets [5]. One can guess that low critical embryo size can raise the internal critical embryo pressure. That leads the carrier gas solubility growth in the critical cluster and problem turns to binary vapor-gas system nucleation. That is not yet really taken in to account in the most measurements of the vapour-gas nucleation rates. The data inconsistencies from the different devises [5] are a strongest reason for all vapour-gas nucleation rate measuring system development. Multiple inconsistencies initiate speculation that the present nucleation vapour-gas experiments have uncontrollable parameter. A gas-vapor nucleation consideration as binary system is the way to solve the problem of some kind of data inconsistencies.

2. Experimental Schemas for Nanosize Particles Generation

Aitken provided in 1888 practically the first measurement on vapor-gas nucleation. He initiated nucleation by the adiabatic expansion of water vapor in air. Allen and Kassner modified an experimental procedure [6]. They suggested decoupled cycle in a Wilson's type chamber when a recompression is introduced after the adiabatic expansion of a vapor-gas mixture. Recompression stops nucleation and initiates growth of generated clusters to the optically detectable sizes in the atmosphere of low supersaturated vapor. That key idea is basis for quantitative optical measurements of nucleation rate now. Nucleation pulse experiments yield the number density of droplets, N_d. Nucleation rate, J, results as ratio $J = N_d/\Delta t_{exp}$, where Δt_{exp} is the time range of a vapor-gas expansion. Precise determination of the vapor/carrier gas ratio is important for accurate measurements of a nucleation rate. Temperatures are measured with uncertainty within several tenth of K. A shock tube and supersonic jets realized very recently the same adiabatic expansion scheme when cluster generation and growth are decoupled. These systems have the best chance for measuring the highest nucleation rates up to 10^{17} $cm^{-3}s^{-1}$ even set-ups do not have high enough data accuracy yet. Total nucleation temperature interval for adiabatic expansion techniques involves temperatures from (-240) to 100 ^oC; nucleation rate can be measured up to five order interval of nucleation rates in a single realisation of set-up. Expansion techniques cover a total nucleation rate interval from 10^3 up to 10^{17} $cm^{-3}s^{-1}$. The total nucleation pressures involve interval from near 100 kPa to 7 MPa.

A turbulent mixing of a hot vapor-gas stream with a chilled gas can be used for particle generation. Amelin has used in 1948 that system for first measurements of a single vapor nucleation rates in a turbulent regime [6]. Using turbulent flow the isothermal nucleation rates were measured for binary systems within several orders of magnitude. Problem of a turbulent mixing scheme is associated with wide spectrum of nucleation conditions which can not be attributed to a particular ensemble of particles generated within a nucleation zone. To simplify problem one can use a firm requirement that nucleation needs to be started when a system gets a temperature and vapor distribution homogeneity. Nevertheless that condition can not be controlled now and problems of system homogeneity and nucleation sequence arise in any turbulent mixing experiment. Fluctuations of vapor supersaturation and temperature can be big enough to generate some pre-particles before system gets homogeneity. These pre-particles initiate a heterogeneous nucleation and a partition problem for heterogeneous and homogeneous nucleation arises.

Langsdorf has created the first static diffusion chamber (SDC) in 1939 [6]. Static diffusion chamber represents two wet plates under different temperatures. Clusters of new phase are generated at some layer and grow then. Particles can be moved to a cooled plate direction by temperature or/and vapor concentration gradients. A particle drops down when their mass gets big enough. A special design of SDC is used for vapor-gas nucleation measurements at elevated pressures up to 40 bar. Vapor diffusion and temperature gradients provide a vapor supersaturation and nucleation occurs at the certain conditions in space within plates. Temperature and mole fraction distributions need to be calculated using a transport process model. The key problem is to reach an operational stability of the vapor-gas mixture in SDC with respect to convective flows. Total nucleation temperatures for SDC involves interval from (-30) to 100 ^{o}C; nucleation rate can be measured in four order interval in one set-up. A total nucleation rate span interval from 10^{-2} up to 10^{2} $cm^{-3}s^{-1}$. Nowdays available nucleation pressures for SDC are within interval from 30 kPa to 4 MPa.

The impressive data are collected using a recently designed Flow Diffusion Chamber (FDC). Several articles devoted to FDC first versions were published in 1978 [6]. FDC scheme involves using the hot laminar vapor-gas flow within the colder boundaries. Hot vapor-gas flow enters chilled tubing (condenser). Particles are generated in nucleation volume and grow in a supersaturated vapor media then. A geometrical separation of nucleation volume and a down stream zone for cluster growth are realised. Filtered carrier gas saturates by substance under investigation passing through a vapor saturator. It is assumed that a tubing boundary vapor pressure is under wall equilibrium conditions. Vapor concentration at the beginning of tubing is defined by vapor saturator design. Solution of a heat-mass transfer problem can be done in the approximation of a long channel. Nucleation occurs in the condenser. Aerosol concentration and particle size distribution is measured by the aerosol counter, which is placed before pressure controller to avoid the nucleation inside of controller during an exhaust pressure drop. All experimental parameters are collected by the data acquisition unit. The maximum experimental value of the nucleation rate, J_{max}, in diffusion chambers can be measured using an obvious relation $J_{theor}/N_{theor}=J_{max}/N_{exp}$, where J_{theor} is maximum theoretical nucleation rate; N_{theor} and N_{exp} are the theoretical and experimental FDC particle concentrations respectively. That relation can be used for J_{max} measurements in supersonic nozzle as well. The current FDC scheme is used for the vapor nucleation rate measurements at the total pressures from 0.03 to 0.50 MPa. The FDC data span over six orders of magnitude in nucleation rate which is measurable in a single set-up. The achieved nucleation temperature interval is from (-40) to 700 ^{o}C. Several versions of FDC have built in Finland, USA, Czech Republic, *etc*. It looks that for present time only four groups [6] measured the isothermal nucleation rates for binary vapors in gas atmosphere within several orders of magnitude. The most part of researchers measure only critical vapor supersaturations for two-component vapor systems. Vapor-gas nucleation are suggested to be considered as binary systems because of clear influence of carrier gas (CO_2, SF_6) on critical embryo phase transitions [6].

3. Short Summary

Presumably the first nucleation experiment was associated with measuring of the liquid and crystals supercooling which were done by Fahrenheit. Then the bubble nucleation of gas

saturated solutions was observed and the critical embryos of new phase were introduced in nucleation science at the second half of 19-th century. A quality of vapor-gas nucleation rate results has been increased substantially in 1980th. Currently the most discussed problem is a relation of experimental data and theoretical predictions of nucleation rate values. As a rule theoretical and experimental data on nucleation rate are not in agreement up to now. Seemingly both data sets have problems because all versions of nucleation theories and practically all experimental results can be criticized [6]. The present day theory looks quite reasonable for low enough vapor nucleation rates, when the droplet approximation is applicable. Theory gets low worth at nanosize scale when critical embryos contain around or less than 200 molecules (atoms). It looks now that given quantity of molecules is near the threshold for the droplet critical embryo approximation at least for vapors of organic compounds [6]. Advantages and current problems of the vapor-gas nucleation experiments are discussed in the frame of a present review. A vision of the future researches is presented on the base of the reviewed results on vapor-gas nucleation.

The introduction of one or several nucleation standard(s) is an actual current problem. Success in the nucleation standard development and its introduction in the nucleation research practice is the key problem of nucleation experiment of the present. The dipper understanding of the carrier-gas effects has chance to clarify the nature of the different experimental set data inconsistencies. One can conclude that a flow diffusion chamber is the powerful tool for the vapor nucleation rate measurements which can be used jointly with the expansion (piston&jet) techniques and the static cloud chamber. There is hope that data consistence of all these methods will be reached in the nearest time.

Acknowledgements

Research is under support of the Russian Foundation for Basic Research through grant numbers of 07-08-13529-ofi and 07-03-00587-a

References

[1] M.P. Anisimov, P.K. Hopke, D.H. Rasmussen, S.D. Shandakov, V.A. Pinaev, “Relation of phase state diagrams and surfaces of new phase nucleation rates“, J. Chem. Phys. **109**(4) 1435-1444 (1998).

[2] L.M. Anisimova, M.P. Anisimov, G.L. Semin, P. Turner, and P.K. Hopke, “An Algorithm for Semi-Empirical Design of Nucleation Rate Surface“, J. Colloid Interface Sci., **290**, 107-116 (2005).

[3] J.H. Seinfeld and S.N. Pandis, “Atmospheric chemistry and physics: from air pollution to climate change” (New York, Wiley and Sons, 1998).

[4] Ja.I. Frenkel, “Kinetic theory of liquids” (Nauka, Leningrad. 1975).

[5] D. Brus, A. Hyvarinen, V. Zdimal, H. Lihavainen. “Homogeneous nucleation rate measurements of 1-butanol in helium: A comparative study of a thermal and laminar flow diffusion chamber”, J. Chem. Phys., **122**, 214506 (2005).

[6] M.P. Anisimov, “Nucleation: Theory and Experiment”, *Russian Chemical Reviews*, 72(7) 591-628 (2003).

Phase-Field Modeling of Hydrogen-Dislocation Interactions and its Evolution in α-Iron

Hajime Kimizuka, Hideki Mori, and Shigenobu Ogata

Department of Mechanical Science and Bioengineering, Osaka University,
1-3 Machikaneyama-cho, Toyonaka, Osaka 560-8531, Japan
(E-mail: kimizuka@me.es.osaka-u.ac.jp)
"Fundamental Studies on Technologies for Steel Materials with Enhanced Strength and Functions"
Consortium of JRCM (The Japan Research and Development Center for Metals)

ABSTRACT

We construct a numerical model of the coupled evolution of hydrogen-concentration and defect fields in iron based on a phase-field (PF) microelasticity theory, with coupling of the long-range elastic interactions and short-range chemical interactions that control hydrogen and dislocation motion. To obtain the physical parameters included in the PF free-energy functional, the interaction energy between a hydrogen atom and dislocation core, and the hydrogen-concentration dependence of misfit energy and eigenstrains are quantitatively determined using an embedded-atom-method (EAM) and/or density-functional-theory (DFT) calculations. Based on these data, we investigate an evolution of the hydrogen-dislocation interactions, and also a hydrogen diffusion and concentration around piled-up dislocations under applied stresses at various temperatures. It is clearly observed that the hydrogen is significantly localized and concentrated around dislocation cores, so that the remarkable difference exists in hydrogen concentration between in the bulk region and in the vicinity of dislocation cores, ranging from several weight ppm to several thousands weight ppm. Also, the spatial profile of trapped hydrogen around dislocations strongly depends on the stress field produced by dislocations. With increasing temperature, the trapped hydrogen escapes from dislocations and hydrogen concentration around dislocation cores steadily decreases. From our EAM and DFT results, the misfit energy of iron is remarkably lowered by the hydrogen impurity at high concentration. This fact brings the result that the distribution of hydrogen concentration affects the dislocation configurations, and the width of dislocation core becomes broader due to the trapped hydrogen.

This study was carried out as a part of research activities of "Fundamental Studies on Technologies for Steel Materials with Enhanced Strength and Functions" by Consortium of JRCM (The Japan Research and Development Center of Metals). Financial support from NEDO (New Energy and Industrial Technology Development Organization) is acknowledged.

Micron-nanometer Lithium Manganese Oxides

Xinghua Xie

Anhui University of Science and Technology, Huainan, Anhui, China
(E-mail: xxh1963@163.com)

ABSTRACT

Lithium manganese oxides are of great interest as cathode materials for lithium-ion batteries. We describe here a new combustion method to synthesize lithium manganese oxides directly from lithium nitrate, manganese nitrate, ammonium nitrate and glycol. The resultant $LiMn_2O_4$ synthesized under the optimum synthesis conditions shows perfect spinel structure and uniform particle size distribution. The combustion products were characterized by scanning electron microscopy. And, powders X-ray diffraction and transmission electron microscopy were used to characterize the products. Lithium manganese oxides with approximately acerose crystal morphology of 100-200 nm length with 10-15 nm diameter and a variety of morphologies were found. The oxides produced by this cheap method affirmed the validity of combustion synthesis of fine powders. Lithium manganate with a fine structure different from that of the normal spinel is formed after combustion wave treatment due to the addition of ammonium nitrate. It might also provide a cheap large-scale synthesis method. Reagents combustion with the addition of ammonium nitrate is strongly nonequilibrium processes. Free metal atoms are first released with the decomposition of reagents, and then theses metal and oxygen atoms are rearranged, coagulated and finally crystallized into lithium manganate during the expansion of combustion process.

Keywords: Spinel phase $LiMn_2O_4$, combustion method, ammonium nitrate, acerose crystal